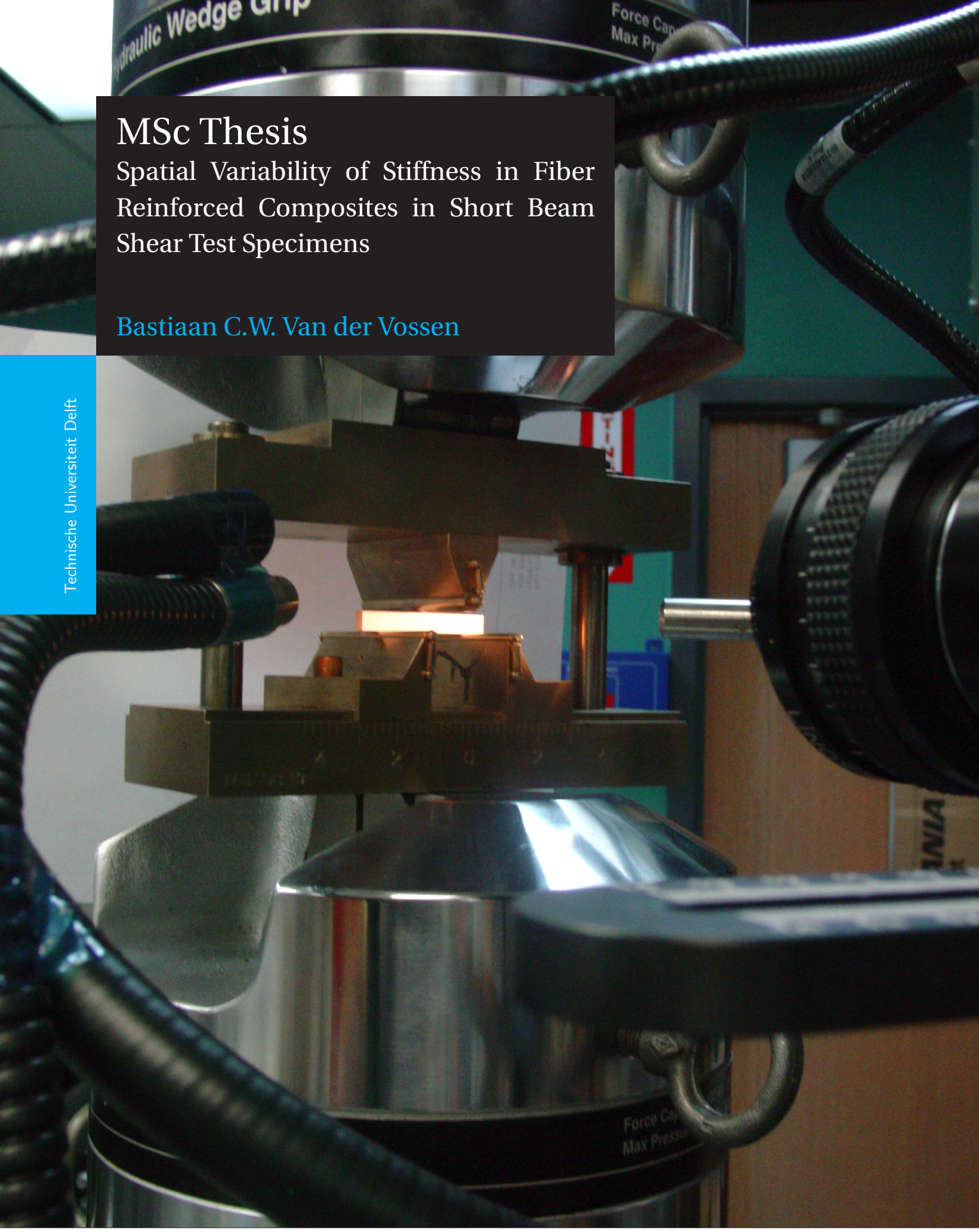


MSc Thesis

Spatial Variability of Stiffness in Fiber Reinforced Composites in Short Beam Shear Test Specimens

Bastiaan C.W. Van der Vossen

Technische Universiteit Delft

TU Delft Delft University of Technology

Challenge the future

MSc Thesis

Spatial Variability of Stiffness in Fiber Reinforced Composites in Short Beam Shear Test Specimens

by

Bastiaan C.W. Van der Vossen

in partial fulfillment of the requirements for the degree of

Master of Science
in Aerospace Engineering

at the Delft University of Technology,
to be defended publicly on April 14, 2014 at 14:00.

Student number:	1522418	
Contact:	bastiaanvandervossen@hotmail.com	
TU Delft Supervisor:	Dr. ir. R.C. Alderliesten	
UTA Supervisor:	Dr. A.V. Makeev	
Thesis committee:	Dr. ir. R.C. Alderliesten	Structural Integrity & Composites
	Dr. C. Kassapoglou	Aerospace Structures & Comp. Mechanics
	Dr. C.D. Rans	Structural Integrity & Composites

An electronic version of this thesis is available at http://repository.tudelft.nl/.

TU Delft Delft University of Technology

PREFACE

Studying at the Advanced Materials and Structures Lab at the University of Texas at Arlington (UTA) has been a very rewarding experience. My colleagues in the lab comprised a very diverse group, emanating from different countries throughout the world, providing a liberating international and open mindset. I found the atmosphere to be both stimulating and challenging, affording each student requisite freedom to engage in individualized research, while concurrently furthering the research goals of the lab. Furthermore, the research goals are ambitious and relevant for industry, with a lot of projects running at the same time. I appreciate that the lab is ambitious in their targets and that there is a lot of contact with industries. Therefore, I look forward to continuing my research in this department and contributing towards meeting said goals.

I would like to take this opportunity to extend my appreciation to my friends, family, and colleagues for assisting me through my final thesis work for the Master of Science in Aerospace Engineering degree. First of all, I would like to thank my Delft advisor, Dr.ir. R.C. Alderliesten, for his support and for allowing me to accept an international position to do my research. Next, I would like to thank Dr. Makeev, who directly supervised me, for his vision and guidance, while allowing me the freedom to take my own initiative. I am also grateful to Dr. Armanios, who provided me a warm welcome to the Department of Aerospace Engineering at UTA.

I would also like to express my gratitude to my colleagues at the Advanced Materials and Structures Lab, who have inspired me and supported me in my research. They have provided a fun and friendly working environment. I would like to thank Dr. Yihong He, Yuri Nikishkov, and Katia Bostaph for introducing me to and helping me to work with the necessary tools. Furthermore, I was fortunate to have Brian Shonkwiler and Julia Cline assist with experimental work, while providing feedback on my results. Lastly, Guilluame Seon's assistance and feedback on the quality of my research provided me with an invaluable resource.

Additionally, I want to thank my loving girlfriend, Leine Newby-Estrella, for all her support through thick and thin. A great deal of gratitude goes to Karen-Sue Newby, for proofreading my report and offering a lot of editing suggestions. Last but not least, I am very grateful for my family and friends at home. I would especially like to thank my parents, Henk and Hanneke van der Vossen, who have always been supportive of my plans and decisions, and who have made everything possible. Thank you.

Bastiaan C.W. Van der Vossen
Delft, April 2014

SUMMARY

Modern and future aerospace structures make increasing use of fiber reinforced composite materials to optimize structural performance. Failure mechanisms of out-of-plane loads in composite shells are often dominated by non-linear interlaminar shear and transverse stresses. Material properties related to these failure loads are hard to characterize, especially when they influence each other. Micro-damage models predict that non-linear shear stiffness properties change in the presence of transverse stresses. Due to their highly anisotropic nature and susceptibility to the environment and production processes, characterizing composite materials is often a very time- and cost-intensive problem.

Conventionally, the Short Beam Shear (SBS) method was only used as a quality control tool for the fiber-matrix interfacial bond. However, in combination with Digital Image Correlation (DIC) techniques, it can be used to measure multiple material characteristics of uni-directional composite coupons in a single test set-up [1]. This is a cost- and time-effective method for the characterization of the 3D material constitutive model. As the Short Beam Shear test setup is able to measure the material response in the shear non-linear region, it is in theory possible to investigate phenomena that occur in this non-linear regime.

This report shows a further development of the test method, with a Finite Element Model Updating (FEMU) approach to accurately characterize the material properties. For any given surface in the xy-plane, the program converges on axial (length-direction) tensile/compressive stiffness values, the Poisson's ratio, and the non-linear shear properties. The model is parameterized so that all specimen-specific dimensions and loading data are taken into account. The converged properties improve significantly upon the closed-form solution, when the length-to-thickness ratio is smaller than seven.

Over the front surface of the specimen, stresses are taken from the Finite Element Model and combined with strains measured from DIC. Using the converged material properties, it is assumed that the stresses in the Finite Element Analysis are representative of the actual stresses in the test. Using nodal stress calculations and corresponding strain measurements, it is possible to set stress-strain curves along the surface, from which material parameters can be calculated. Spatial variability analyses of shear stiffness parameters show increased stiffness in the non-linear regime where transverse stresses are compressive. This indicates that transverse stress components do influence the shear stress-strain response.

Finally, this report shows how a non-linear coupling term between transverse stresses and shear strains is incorporated into the compliance matrix of the material model in the Finite Element Analysis. The influences on the strain fields are plotted, showing how the solution in FEM diverges from the measured strains in DIC. This form of coupling is thus not valid in this composite material.

In conclusion, the tools produced during this thesis improve upon the accuracy of the material parameter identification in the SBS test specimens. The thesis also shows that the test can be used to characterize coupling phenomena between transverse stresses and shear strains.

CONTENTS

Preface iii

Summary v

List of Symbols ix

List of Figures xi

List of Tables xiii

1 Introduction 1

2 Background Information 3
- 2.1 Constitutive Model for UD Composite Materials . . . 3
- 2.2 Industry Standards in Characterization of Composite Materials . . . 5
- 2.3 Thesis Background, the Adapted Short Beam Shear method . . . 8
- 2.4 Material Parameter Characterization; the Inverse Problem . . . 10
- 2.5 Statistics in Material Parameter Characterization . . . 11
- 2.6 Spatial Variability of Material Properties . . . 12
- 2.7 Scope and Objectives of the Thesis . . . 13

3 FEM Updating Method 17
- 3.1 Analytical Solution for the Material Characterization . . . 17
- 3.2 The Numerical Model in Abaqus/CAE . . . 22
- 3.3 User Material Subroutine for the Numerical Model . . . 25
- 3.4 Interface and Architecture of the FEMU Model . . . 26
- 3.5 Material Parameter Iterations . . . 26
- 3.6 Material Characterization Performance . . . 29

4 Spatial Variability of Constitutive Model Parameters 35
- 4.1 Refined FEM Model and DIC Plotting Tool . . . 35
- 4.2 Spatial Variability Analysis Methodology . . . 37
- 4.3 Spatially Varying Shear Non-Linear Stress-Strain Curves . . . 38
- 4.4 Stiffness Plots with Nodal Calculations . . . 39
- 4.5 Conclusions on Spatial Variability Analysis . . . 42

5 Constitutive Model Verifications 45
- 5.1 Bilinear Axial Strain Assumption . . . 45
- 5.2 Stress-State Dependent Poisson's Ratio . . . 47
- 5.3 UMAT Adaption for Coupled Shear - Transverse Stresses . . . 49
- 5.4 Verification of UMAT with Coupling Terms . . . 50
- 5.5 Application of UMAT with Coupling Terms in SBS Specimens . . . 51

6 Conclusions and Recommendations 55
- 6.1 Conclusions . . . 55
- 6.2 Recommendations . . . 56

Bibliography 59

A Interface for the FEMU Model 63
- A.1 FEMU Program Work Directory Overview . . . 63
- A.2 Input File Template . . . 64
- A.3 Output File Example . . . 64
- A.4 FEMU Program Readme . . . 64
- A.5 FEMU Program Example Batch Script . . . 68

B Influence of Noise in DIC Measurements **69**

C Apparent Stiffness Plots with Homogeneous Model **73**
C.1 Local Stiffness Changes in FEM 73
C.2 Local Stiffness Changes in DIC 74

D Least-Squares Solution for Ramberg-Osgood Parameters **77**

E Added Coupling Terms in Shear Non-Linear Regime: Calculations **79**
E.1 2-Dimensional Coupling 79
E.2 3-Dimensional Coupling 80

F Introduction to the Included CD **83**

List of Symbols

Symbol	Definition
0	Reference
1-direction	Direction parallel to the fibers
2-direction	In-ply direction perpendicular to the fibers
3-direction	Out-of-ply direction
AMSL	Advanced Materials and Structures Lab
AR	Aspect Ratio
b	Intercept of the axial strain approximation
C	Compressive
CEGM	Constitutive Equation Gap Method
CFRP	Carbon Fiber Reinforced Plastic
.CSV	Comma Separated Values (document format)
CT	Computer Tomography
DIC	Digital Image Correlation
E	Axial Stiffness
EGM	Equilibrium Gap Method
FEA	Finite Element Analysis
FEM	Finite Element Method
FEMU	Finite Element Model Updating
G	Shear Stiffness
GFRP	Glass Fiber Reinforced Plastic
h	Specimen thickness
I	Inertia
K	Ramberg-Osgood secant-intercept modulus
	Coefficient for Coupling Terms in UMAT
L	Distance between test supports
L_L	Distance between loading nose and left support
LS	Least-Squares
L_R	Distance between loading nose and right support
M	Moment
n	Ramberg-Osgood exponent
P	Applied Load
R	Radius
R_A	Reaction force left support
R_B	Reaction force right support
R_L	Lower limit linear shear regression analysis
R_{NL}	Lower limit non-linear shear regression analysis
R_U	Upper limit linear shear regression analysis
RGM	Reciprocity Gap Method
SBS	Short Beam Shear
S	Compliance Matrix, FEM stress component
T	Tensile
TU Delft	Technical University Delft
UD	Uni-directional
UMAT	User Material Subroutine
UTA	University of Texas at Arlington
V	Shear Force
VFM	Virtual Fields Method

V_m	Height Neutral Axis
w	Specimen width
x	(distance along) length-direction
y	(distance along) thickness-direction
γ	Shear Strain
Δ	Change in
δ	Difference in
ϵ	Axial Strain
κ	Slope of the axial strain approximation
ν	Poisson's ratio
μ	Mean (statistics)
ρ	Bending Radius
σ	Axial Stress, Standard Deviation
τ	Shear Stress

List of Figures

2.1 Ramberg-Osgood Equation fitting Measurement Data . . . 4
2.2 Coupling Effects between Transverse and Shear Stresses and Strains . . . 5
2.3 Summary of Test Methods used to Formulate Composite Mechanical Properties [2] . . . 6
2.4 Cost Breakdown of Generic Material Testing Program . . . 7
2.5 Specimen Selection and Batch Traceability for B-Basis Material Allowables [3] . . . 8
2.6 Short Beam Shear Test Setup, showing the fixture, a coupon being tested and the optical system. (Source: AMSL Lab at UTA) . . . 9
2.7 Loading Configuration of the SBS method. Note the Failure in Interlaminar Shear [4] . . . 9
2.8 Heterogeneous material model in FEM (Left). Reconstruction of the contrast of shear modulus resulting from identification with Dirichlet boundary conditions in CCM (Right) . . . 13
2.9 Concept Experimental Set-up . . . 15

3.1 Different Options to Cut SBS Coupons from a Plate [5] . . . 19
3.2 Testing and Processing the SBS Specimen in Different Planes results in different Material Constitutive Properties [5] . . . 20
3.3 Coordinate Notation and Axial Strain Distribution in the SBS Specimen . . . 20
3.4 Static Analysis of the SBS Specimen . . . 21
3.5 Transverse vs Axial Strains. Defining a linear section in this model is representative for the Poisson's ratio. In this figure, $\nu = 0.3$ . . . 22
3.6 Typical FEM Model as Created by Dr. He [6], shown with changed reference coordinates . . . 22
3.7 Schematic of Refined Mesh Regions in SBS Quarter Specimen [6] . . . 24
3.8 Symmetry Analysis SBS Coupons. (a) Full Model. (b) Front Half Model. (c) Right Half Model. (d) Quarter Model . . . 24
3.9 Quarter Model of the SBS Test with Solid Support and Loading Nose . . . 24
3.10 Overview of FEMU Program: Hierarchy and Architecture, . . . 27
3.11 Overview of FEMU Program: How do Variables Update and how does that affect Material Parameters . . . 28
3.12 Converging Shear Stress-Strain Response in UD IM7/8552 using Bi-linear Shear Stress Equation 29
3.13 Converged Shear Non-Linear Properties Agree with Iosipescu Beam Specimens [6] . . . 31
3.14 Comparison Converged Material Properties from SBS to Manufacturer Hexcel Data . . . 31
3.15 Strain Comparison of DIC Measurements and FEM Output at Right Cross-Section in S2/381 UD Composite at 555 lbf . . . 32
3.16 Strain Field Comparison of IM7/8552 SBS Specimen under 1100lbs Load . . . 33
3.17 The Load-Displacement Curves match between FEM and DIC if Converged Material Properties are used . . . 33

4.1 Overview of the FEM Model with Refined Mesh (left side only). Areas A and B are used for the Mesh Convergence Analysis . . . 35
4.2 Mesh Convergence for Refined SBS Model. . . . 36
4.3 Choice of Nodes for Shear Stress-Strain Plots . . . 39
4.4 Shear Stress-Strain Curves with Coupling Phenomena. (a) shows raw data from FEM and DIC. (b) shows the same data with translated starting points . . . 40
4.5 Spatial Variability of Linear Shear Stiffness G_{13} of IM7/8552 in SBS Specimen . . . 40
4.6 Spatial Variability of Shear Stiffness Parameters of IM7/8552 in SBS Specimen. The three plots show: (a): G_{13}, (b): G_K, (c): G_n . . . 41
4.7 Spatial Variability of Axial Stiffness Modulus E_{11} of IM7/8552 in SBS Specimen. Calculations Across Frames . . . 41
4.8 Spatial Variability of Axial Stiffness Modulus E_{11} of IM7/8552 in SBS Specimen. Calculations Within Frame . . . 42

4.9 Histogram of Axial Stiffness E_{11} in figure 4.7 . . . 42
4.10 PDF and CDF of E_{11}, Excerpts from Histogram in Figure 4.9 . . . 42
4.11 PDF and CDF of Shear Stiffness G_{13} in figure 4.5 . . . 43

5.1 Axial Strains at L/4 Cross-Section with Different Trend Lines in Compression and Tension in CFRP 45
5.2 Overview, Deformed and Cross-Section View of a Bending Problem . . . 46
5.3 Comparison FEM and DIC Transverse Strains for IM7/8552 under 1100 lbs Load . . . 48
5.4 Line Slices of Axial Strains vs Transverse Strains in S2/381 4-Point Bending Specimen . . . 48
5.5 The Poisson's Ratio changes at the Neutral Axis in S2/381 4-Point Bending Specimen . . . 48
5.6 Delaminations at Compressive Edge cause Strain Anomalies . . . 49
5.7 Single Element Model Used to Verify the UMAT with Coupling Terms . . . 50
5.8 Effect of Simulated Coupling Between Transverse Compressive Stress S33 on the Shear Stress-Strain Curve. The S33/S13 Stress Ratio is 1/2 . . . 51
5.9 Simulated Strain Components at the Right Cross-Section in an SBS specimen in FEM. Blue = Uncoupled. Red = Coupled . . . 51
5.10 Strain Field in FEM with Coupling Term in UMAT . . . 52
5.11 Strain Fields in DIC. (a) Low Load (b) High Load . . . 52
5.12 AR and T/C Ratio Analysis: Strains at $L_R/2$ from FEM . . . 53

A.1 Overview of File Organization of FEMU Program . . . 63

B.1 Compression Test Specimen, showing the Speckle Pattern . . . 70
B.2 Transverse Strains in IM7/8552 Compression Specimen and its Statistical Distribution . . . 71
B.3 Axial Strains in IM7/8552 Compression Specimen and its Statistical Distribution . . . 71
B.4 Shear Strains in IM7/8552 Compression Specimen and its Statistical Distribution . . . 71

C.1 Apparent Axial Stiffness over the Front Surface of a SBS Specimen in FEM . . . 74
C.2 Apparent Shear Stiffness over the Front Surface of a SBS Specimen in FEM . . . 74
C.3 Apparent Axial Stiffness over the Front Surface of a SBS Specimen in DIC for S2/8552, Specimen 1 75
C.4 Apparent Shear Stiffness over the Front Surface of a SBS Specimen in DIC for S2/8552, Specimen 1 75
C.5 Apparent Axial Stiffness over the Front Surface of a SBS Specimen in DIC for S2/8552, Specimen 2 75
C.6 Apparent Shear Stiffness over the Front Surface of a SBS Specimen in DIC for S2/8552, Specimen 2 75

D.1 Curve-Fitting of Shear Stress-Strain Data using a Regression Analysis in Excel and 3-Parameter Nonlinear Curve-Fits with and without weights . . . 78

LIST OF TABLES

2.1 Validation Measures for Causes of Spatially Varying Mechanical Properties 15

3.1 Convergence of the Material Properties of IM7-8552 using FEMU, Bi-Linear Shear Stress Approximation. * = average between tensile and compressive values 30

4.1 Details of Maximum Stress Components on Selected Nodes 39
4.2 Results Statistical Analysis Stiffness Plots Figures 4.5 and 4.7 43

5.1 Input and Expected Parameters for the T/C Ratio Analysis 47
5.2 Results T/C and Aspect Ratio Effect Analysis 47

A.1 FEMU Input Template, Sheet 1 65
A.2 FEMU Input Template, Sheets 2-4 65
A.3 FEMU Output Sheet for IM7/8552 Specimen, Iteration 1 66

B.1 Mean Values and St. Deviation for Tensile Specimens T1 and T2 for IM7/8552. Format: μ (σ [%]) 70
B.2 Mean Values and St. Deviation for Compression Specimens C1 and C2 for IM7/8552. Format: μ (σ [%]) 72

D.1 Parameters of the Curve Fits for the Ramberg-Osgood Equation 78

F.1 Important Files in the Attached CD 83

1

INTRODUCTION

Fiber Reinforced Composite materials are fundamental to modern aerospace structures. Advances in this area of knowledge will increase future performance of these structures. The performance of these structures is driven in part by the characteristics and understanding of the materials. Failure mechanisms of out-of-plane loads in composite shells are often dominated by non-linear interlaminar shear and transverse stresses. Those properties are hard to characterize, especially when they influence each other. The understanding of the structural performance is defined by mechanical tests, but this is an intensive process [2]. Due to the high anisotropy of these composite materials and their susceptibility to time, temperature, and moisture, it takes hundreds to thousands of tests to fully characterize a material. Some of these properties are hard to characterize and might not even be measured at all[3]. Currently, industries are creating new materials faster than testing facilities are able to characterize these materials. Therefore, there is a need to define multiple material properties accurately in fewer, simpler, and cost effective test methods.

The Advanced Materials and Structures Lab (AMSL) at the University of Texas at Arlington (UTA) offers a solution: A modified version of the Short Beam Shear (SBS) test method in combination with Digital Image Processing (DIC) of a surface speckle pattern [1, 4]. The test set-up is simple, cost effective, and will characterize the constitutive model of a uni-directional coupon in 3D with just a few coupons. The method is proven to be effective, but there is more knowledge to gain from the full-field DIC strain measurements. In order to improve the accuracy of the post-processing analysis, a Finite Element Model is used to update the nonlinear shear stress-strain response. However, this is not used yet for all constitutive properties. Furthermore, the material characterization is done by using measurements at specific locations. This leads to the research questions:

1. Can one characterize all the constitutive material properties of uni-directional Fiber Reinforced Plastics more accurately using an iterative method comparing the output strains from a Finite Element Model with the strain measurements from DIC? This includes non-linear shear stiffness, axial stiffness, and Poisson's ratio.
2. If the full-field strain measurements from DIC of an SBS specimen are combined with the stresses of an FEA model, can the variation of the material properties over the surface be specified?
3. Is the constitutive model currently used at the AMSL accurate enough to simulate the strains from DIC?

This list shows that there is a need to further develop the test method with respect to post analysis. First of all, the method to converge on all significant material properties will be further developed. Because the non-linear shear response is not yet fully understood, it is important to investigate whether the chosen material model is actually correct. Furthermore, as the DIC software provides hundreds of data points over a surface, it might be possible to determine how the stiffness properties change with respect to xy-coordinates. This leads to the following hypothesis:

"The material model as used by the AMSL lab at UTA is correct and spatial variability of shear stiffness properties will not exceed noise levels."

Spatial variability of material constitutive properties in this thesis will be defined as: "The change in the stress-strain relationship over the surface measured using DIC." For linear relations, this may constitute a change in stiffness. This report will focus on varying shear non-linear parameters.

This report describes and illustrates the research choices made and arguments for each of the research questions. The research is limited to the characterization of Glass and Carbon Fiber Reinforced Plastic unidirectional coupons. The scope of this research is limited to the post-processing of the measurement data. The material convergence iterations are executed using the Finite Element Model Updating (FEMU) method, which changes the input material properties for each iteration depending on a comparison between the FEM and DIC strains. The DIC strains are extracted from digital images using the VIC3D software. The Finite Element Model is created using Abaqus/CAE and parameterized using Python. The material model is custom designed using a User Material subroutine (UMAT) in Abaqus. Finally, Matlab will be used for general calculations, including the statistical package. The research is limited in time and resources. The research itself was conducted from June 2013 to January 2014. There is enough test data in the AMSL servers to do the research, so no tests will be performed specifically for this thesis.

Chapter 2 provides background information on this thesis, including the work already performed at the AMSL lab in this field of research. It also lays out the project planning. Chapter 3 addresses research question 1 by illustrating the FEMU method and its performance. Chapter 4 delineates the research into the spatial variability of stiffness parameters over the surface. Chapter 5 details investigations into the constitutive model, as per research question 3. Chapter 6 reflects upon the significance of the research and summarizes the conclusions and recommendations.

2

BACKGROUND INFORMATION

This chapter will provide background information for the analyses performed for this thesis. It shows the important topics to be dealt with and important sources for further reading. To this purpose, section 2.1 describes some important considerations for specifying the constitutive model. Section 2.2 provides a glimpse into the current standard of characterizing new materials in the industry, which leads to the motivation for this thesis. Section 2.3 illustrates the current state of the project. Other researchers have already developed the SBS test setup as used at UTA, which is explained in this section. The options for material parameter characterization and the statistics involved are detailed in sections 2.4 and 2.5. The options for defining spatial variability of material properties has been given in section 2.6. The chapter ends with the organizational aspect of the thesis, where section 2.7 delineates the scope and objectives.

2.1. CONSTITUTIVE MODEL FOR UD COMPOSITE MATERIALS

The mechanical behavior of materials and structures requires knowledge of the relationship between stresses and strains, the constitutive model. Due to the high specific strength and specific stiffness of composite materials, their popularity and demand in aerospace structures is on the rise. This increased demand leads to a high rate of development of new materials. Among these, glass and carbon fiber/epoxy laminated composites have proven quite important in high-performance designs.

The focus in this thesis lies within characterizing material properties for Glass - and Carbon Fiber Reinforced Plastics (GFRP and CFRP). The specimens are uni-directional (UD) coupons; all plies in the coupon are stacked such that the fiber direction remains constant for each ply.

In the tested materials, the shear stiffness is not linear [7–9]. Several non-linear response equations are proposed, notably third-power stress-strain responses and the Ramberg-Osgood equation. A third-power stress-strain response becomes less accurate in high strain regions, but works well in linear systems such as the Virtual Fields Method. This third power is representative of some composite materials, but the Ramberg-Osgood offers the flexibility to specify any other exponent, see Eq. (2.1) and figure 2.1.

$$\gamma_{xy} = \frac{\tau_{xy}}{G_{xy}} + \left(\frac{\tau_{xy}}{K}\right)^{\frac{1}{n}} \tag{2.1}$$

In Equation (2.1), K and n are non-linear parameters. This non-linear regime for composites is not yet fully understood. Most literature suggests that the three-dimensional stress state will have no coupling between the axial/transverse and shear stiffness properties. However, there is reason to believe that the UD coupons have extra coupling terms in this regime [10, 11]. As the shear stress increases, micro-damage in the matrix

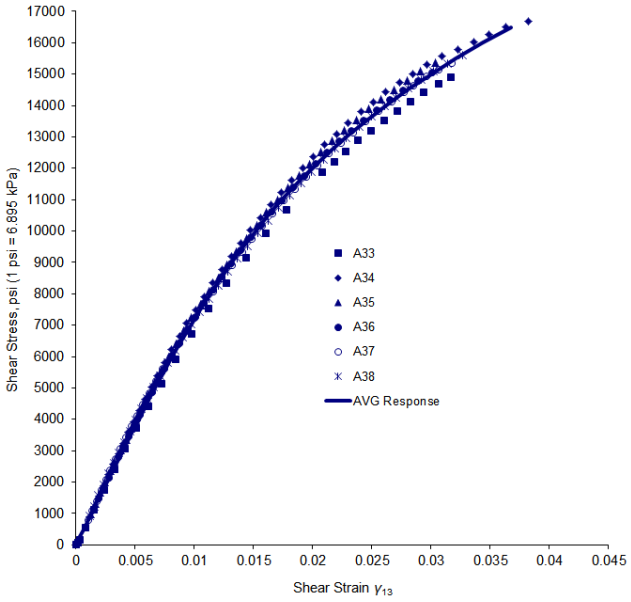


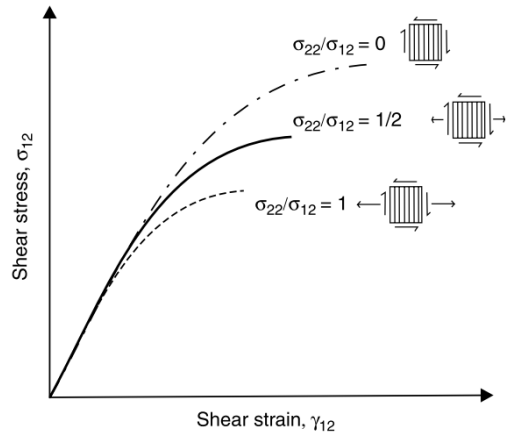
Figure 2.1: Ramberg-Osgood Equation fitting Measurement Data

causes a loss of stiffness; the stress-strain curve becomes nonlinear. Transverse stresses would interfere with the micro-damage in the matrix and thus affect the shear stress-strain curve. A tensile load would induce cracks and a compressive load may delay or induce the onset of cracks, as has been illustrated in Fig. 2.2. More experimental and analytical data is shown by Vogler and Kyriakides [12][13], who have done a systematic approach on the interaction between non-linear transverse compression and non-linear shear in AS4/PEEK.

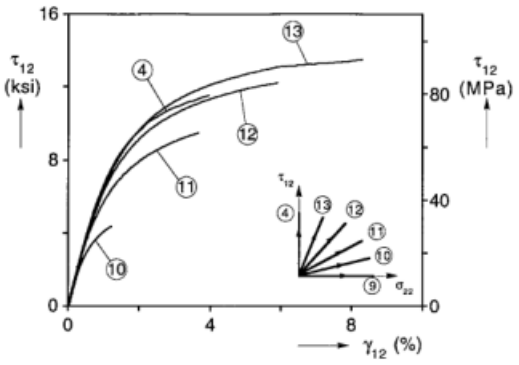
It will become increasingly important to be able to know the effect of shear non-linearity and influences from transverse stresses, because aerospace systems tend to increase structural efficiency over time and with it the stresses acting on the composite material. Camanho [11] has performed some experimental and analytical research examining load capacity of composites under transverse tensile and shear stresses. In many composite structures with shells, the failure load is often limited by the transverse and interlaminar shear stresses, which cause plies to separate and delaminate. In out-of-plane loading, these failure modes become more significant than noted in-plane loading. Camanho builds upon Hashin's theory, in which matrix failures depend on the shear load and the transverse load. These influence each other and thus the failure load. Including coupling effects renders this failure prediction more complex, but also more accurate. Whereas it is possible to define an interaction between these stress components, it is very important to note that the shear behaves non-linearly. Due to this non-linearity, the stress components are overestimated. As the matrix becomes more ductile, the load capacity decreases from what is often expected analytically. The stiffness decreases due to micro-damage in the matrix. These micro-cracks do not develop into macro-cracks due to the presence of fibers, but have a significant effect on the stiffness of the specimen.

$$\begin{Bmatrix} \epsilon_1 \\ \epsilon_2 \\ \epsilon_3 \\ \gamma_{23} \\ \gamma_{13} \\ \gamma_{12} \end{Bmatrix} = \begin{bmatrix} \frac{1}{E_{11}} & \frac{-\nu_{12}}{E_{11}} & \frac{-\nu_{13}}{E_{11}} & 0 & 0 & 0 \\ \frac{-\nu_{12}}{E_{11}} & \frac{1}{E_{22}} & \frac{-\nu_{23}}{E_{22}} & 0 & 0 & 0 \\ \frac{-\nu_{13}}{E_{11}} & \frac{-\nu_{23}}{E_{22}} & \frac{1}{E_{33}} & 0 & 0 & 0 \\ 0 & 0 & 0 & \frac{1}{G_{12}} + \left(\frac{\tau_{23}}{K_{23}}\right)^{\frac{1}{n_{23}}-1} & 0 & 0 \\ 0 & 0 & 0 & 0 & \frac{1}{G_{13}} + \left(\frac{\tau_{13}}{K_{13}}\right)^{\frac{1}{n_{13}}-1} & 0 \\ 0 & 0 & 0 & 0 & 0 & \frac{1}{G_{23}} + \left(\frac{\tau_{12}}{K_{12}}\right)^{\frac{1}{n_{12}}-1} \end{bmatrix} \begin{Bmatrix} \sigma_1 \\ \sigma_2 \\ \sigma_3 \\ \tau_{23} \\ \tau_{13} \\ \tau_{12} \end{Bmatrix} + \tag{2.2}$$

$$where \qquad E_{11} = \begin{cases} E_{11_T}, & \text{if } \sigma_1 \geq 0 \\ E_{11_C}, & \text{if } \sigma_1 < 0 \end{cases}$$



(a) Effect of Transverse Stress on Shear Stress-Strain Response [10]



(b) Effect of Transverse Compressive Stress on Shear Stress-Strain Response [13]

Figure 2.2: Coupling Effects between Transverse and Shear Stresses and Strains

In this thesis, Equation (2.2) will be used to define the constitutive model. The assumption is that the material is transversely isotropic in shear nonlinearity. In Equation (2.2), the 1 stands for the fiber direction of the uni-directional plies and the 2 stands for the transverse direction. The axial stiffness E and shear stiffness G denote the stiffness moduli of the material. ν stands for the Poisson's ratio. ϵ and γ denote the axial and shear strain respectively. σ and τ are used for axial and shear stress respectively. Certain materials show a difference in tensile and compressive axial stiffness [1]. This is not very important in GFRP, but significant in CFRP. In this thesis, this phenomenon will be referred to as bi-modularity. Other effects, including plastic loading/unloading, nonlinear matrix compression, and creep or fatigue, will not be examined in this thesis, as the analysis concerns quasi-static analyses.

2.2. INDUSTRY STANDARDS IN CHARACTERIZATION OF COMPOSITE MATERIALS

The rapid advances in material development have exceeded the ability to characterize every constitutive property for all materials due to time consuming, costly test set-ups and complex material geometries. For qualification and proper design prediction of deformations and failure mechanisms in highly anisotropic materials, these properties have to be known in all three material directions. Currently, the industry uses many different methods to find the mechanical properties, some of which are never measured due to high specimen cost. Current test methods attempt to develop a uniform stress field, so a single test measures can only measure a single stiffness modulus and one failure criterion. The Military Handbook of Composites [2] specifies a large number of test methods and procedures to characterize composite constitutive properties (figure 2.3). The costs become high due to the necessity of different test set-ups to deal with the anisotropy and high variability in material properties (stiffness, failure allowables, manufacturing quality). This variability comes from irregularities in production and handling, which could be very high. Therefore, a lot of tests are required to specify this variability. This effort makes it also very costly to investigate complicating effects (such as temperature, strain rate sensitivity or damage) in great detail. There are a number of high quality publications that discuss the way mechanical tests are performed. Among these, Adams et al. [14] and Czichos et al. [15] provide more detail on the execution of these tests. Sharpe [16] gives a more up-to-date view on the cutting edge in material characterization, including non-contact measurement methods, like the Digital Image Correlation (DIC) method. This method is also explained by Sutton [17].

The sources previously noted above specify a whole series of tests. A large variety of mechanical properties is involved in composite material characterization because it is highly anisotropic. Unfortunately, standard methods by which to characterize these materials are still in development. Additionally, certain properties are

Test Category	Source of Test Method	
	ASTM	SACMA
Lamina/Laminate Mechanical Tests		
0°/Warp Tension	D 3039	RM 4, RM 9
90°/Fill Tension	D 3039, D 5450	RM 4, RM 9
0°/Warp Compression	D 3410, D 5467	RM 1, RM 6
90°/Fill Compression	D 3410, D 5449	RM 1, RM 6
In-Plane Shear (1)	D 3518, D 5448, D 5379	RM 7
Interlaminar Shear	D 5379	---
Short Beam Strength	D 2344	RM 8
Flexure (7)	---	---
Open-Hole Compression	(draft)	RM 3
Open-Hole Tension	D 5766	RM 5
Single-Shear Bearing (2)	(draft)	---
Double-Shear Bearing (2)	(draft)	---
Compression after Impact	(draft)	RM 2
Mode I Fracture Toughness	D 5528	---
Mode II Fracture Toughness	(draft)	---
Tension/Tension Fatigue	D 3479	---
Tension/Compression Fatigue	---	---

Figure 2.3: Summary of Test Methods used to Formulate Composite Mechanical Properties [2]

hard to measure, such as non-linear shear stiffness. Furthermore, these properties are sometimes strain rate -, moisture -, and temperature-dependent. Next, the industry generally has three important requirements on the test setup.

1. Small specimens and thin laminates are preferred to reduce cost and time;
2. The test setup should measure elastic properties and failure strength. For accuracy, this means the state of stress has to be homogeneous/pure; and,
3. Tests should be performable on common universal testing machines, which rules out exotic shapes and loading configurations.

Figure 2.4 gives a cost breakdown for a material characterization program. The items on the chart are expanded in the list below. Total costs of a new composite database runs in the hundreds of thousands USD and takes years to put together. A great deal of cost and time not only goes into the testing of the material, but also into management, planning, and the cleanup. Therefore, rapid screening of new materials is very useful, as a company will only have to characterize a selection of materials. Numbers and details have been given in an interview with Steven Grohman, engineer at Triumph Aerostructures - Vought Aircraft Division (S. Grohman, personal communication, February 12, 2014)

- Management: 15%
  - Management
  - Scheduling the program
  - Providing planning estimates
  - Communicating program updates
- Planning: 20%

  - Test engineering costs
    - Order materials
    - Allocate Shop labor
    - Allocate Testing time
  - Stress engineering costs
    - Writing code
    - Analysis of the code and test methods
- Raw cost: 50%
  - Material costs
  - Shop labor
  - Engineering labor
  - Testing equipment
  - Analysis of test data
  - Time to write reports
- Cleanup: 15%
  - Customer follow-up
  - Finishing the program

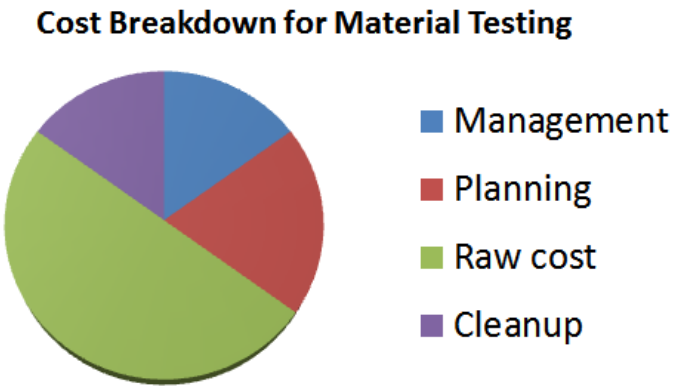


Figure 2.4: Cost Breakdown of Generic Material Testing Program

In order to characterize a material, many specimens have to be tested. Statistical variability of composite material properties has always been a tremendous issue. Reasons for this variability are numerous [18]. In practice, it is costly and time-consuming to create a material database to provide this statistical variability. Figure 2.5 shows how specimens are selected and batch traceability is maintained. This figure shows that 18 specimens are needed per test method and environment (minimum, B-basis parameters). Figure 2.3 shows some of the test methods necessary to characterize the material, but it does not represent all requirements. Some of these tests have to be repeated for laminates with selected lay-up sequences.

One example of a characterized high performance tough epoxy matrix composite material is IM7/8552 carbon fiber composite [19, 20]. It is meant for use in primary aerospace structures. The qualification material property data report is extensive and covers hundreds of both UD and laminate test specimens. Unfortunately, not all material properties are identified in this report. For example, the shear stiffness in the 2-3 plane is not tested. Furthermore, even though the shear non-linearity is touched upon, it is not quantified. Companies are thus advised to perform in-house material testing for relevant laminate stacking sequences, different environments, and any material properties not specified. Considering the tremendous amounts of effort and money that goes into such a program, it is no surprise that a composite material might not be fully understood during the design process of a structure.

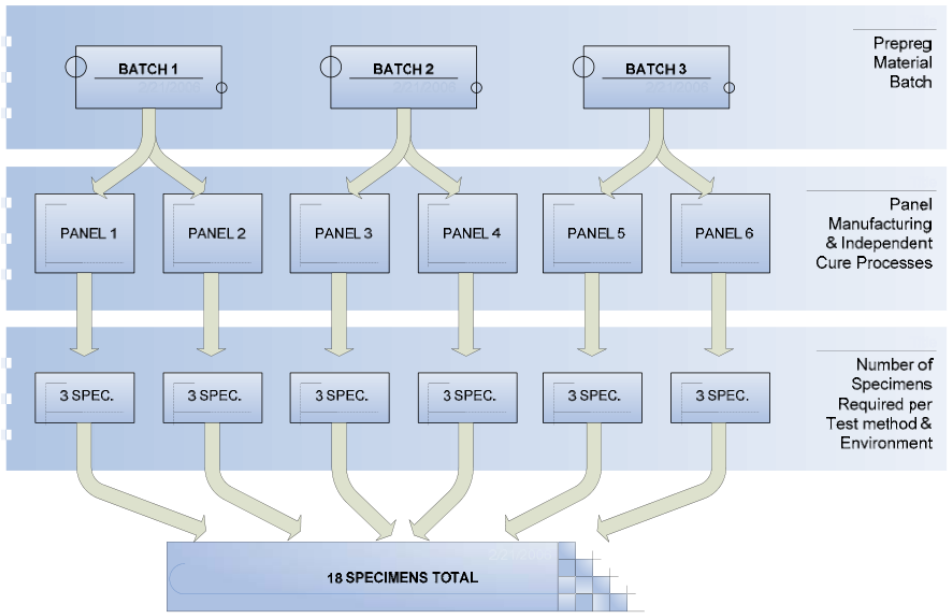


Figure 2.5: Specimen Selection and Batch Traceability for B-Basis Material Allowables [3]

A lot of the testing methods and companies still rely on strain gauges to perform the strain measurements. The promise of new optical methods has persuaded some companies to use these methods for material characterization. Optical methods like Digital Image Correlation (DIC) are very good at showing errors in alignment, given that pinching and misalignment phenomena are shown by strain anomalies. Furthermore, optical methods can expose damage development while performing deformation measurements. It is thus logical to surmise that this method will gain increasing use in industrial testing applications.

2.3. THESIS BACKGROUND, THE ADAPTED SHORT BEAM SHEAR METHOD

Measuring the shear stress-strain response is not straightforward. Multiple test methods measure the shear response curve, but obtaining a pure and uniform shear stress state is hard to achieve. The most accurate test method is to apply torsion to a circular thin-walled tube, but the test can be really expensive and sensitive to test misalignment. The Iosipescu (ASTM D 5379) or V-notched Rail (ASTM D 7078) shear tests manage to produce an area of pure shear. However, the specimens are expensive to produce, because the notches have to be produced with care. The two methods are known to be accurate and reliable. The [$\pm 45^{\circ}$] tension test (ASTM D 5379) and the two- and three-rail shear tests (ASTM D 4255) are more affordable, but fail to produce a region of pure shear [6].

The SBS test (ASTM D 2344 [21]) is a three-point bending shear test. Conventionally, the SBS test is popular, because of its simplicity and ease in which the specimens can be conducted. The method is relatively cheap, but does not provide a uniform shear stress state and failure is often affected by bending and contact stresses. There is an area of pure shear, but this specimen has to be very thick to apply a strain gauge. Instead, the test performs well as a quality control test, as it is a good indicator of the quality of the fiber-matrix interfacial bonds (the interlaminar shear strength).

At the University of Texas in Arlington, a combination of a modified Short Beam Shear (SBS) method [21] and DIC is used to characterize material constitutive properties in three directions as depicted in equation (2.2), along with interlaminar shear and tensile strength. The lab has adapted the SBS method to prevent the contact and bending stresses to influence the in-plane shear strength measurements [5]. Furthermore, the DIC method allows for an accurate measurement of the shear strains at the pure shear region, which would otherwise be too small for strain gauges. As the influences of axial, transverse, and through-the-width stresses are nearly zero at this location, the shear stress-strain response in the SBS specimen should match that of the

more reliable Iosipescu test method.

The materials that have been tested with this method are glass and carbon fiber epoxy composites. The method is well explained by Makeev [1] and the set-up is shown in figure 2.6. The requirements on the test setup, as mentioned previously, are not strictly imposed. The short beam shear (SBS) specimen has a complex stress state with high axial and shear stresses, which allows material characterization in multiple directions [1]. This method would not be very suitable with strain gauges, due to intermittent high stress gradients. The benefits of the SBS test method on industry are as follows:

- Small coupons with simple geometry can easily be manufactured in bulk. From a simple panel, dozens of specimens can be cut with different loading planes.
- Faster initial material screening, if stiffness is important; the 3D constitutive model is characterized in few coupons.
- Accurate and cost-effective material characterization of shear non-linear response will provide for better structural designs.
- The method may replace several other test methods, thereby allowing companies to invest in fewer specimens and fixtures. For instance, the SBS specimens might replace the Iosipescu shear and curved beam test methods.

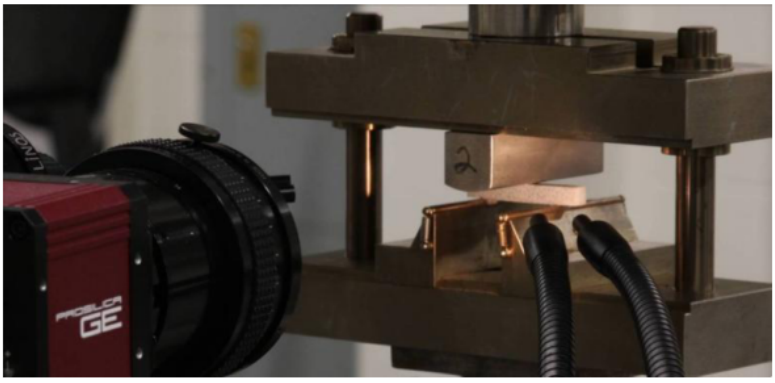


Figure 2.6: Short Beam Shear Test Setup, showing the fixture, a coupon being tested and the optical system. (Source: AMSL Lab at UTA)

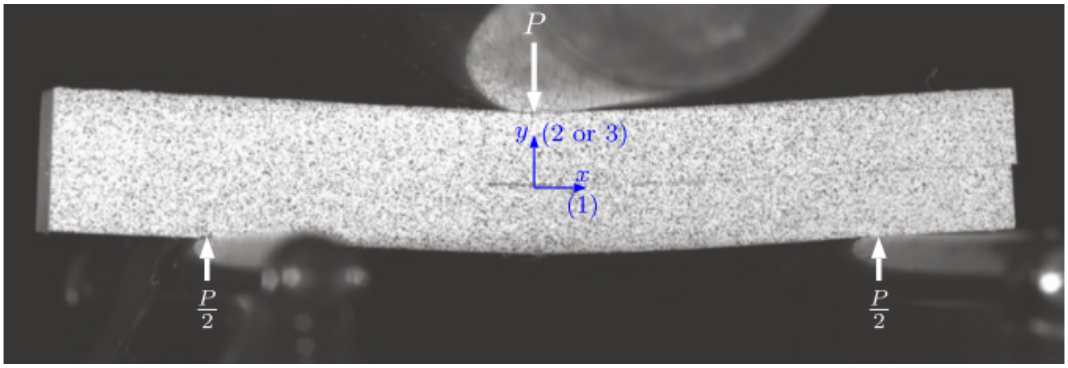


Figure 2.7: Loading Configuration of the SBS method. Note the Failure in Interlaminar Shear [4]

The adaptation of the Short Beam Shear (SBS) test setup is used to measure all constitutional properties to drastically reduce the amount of tests needed for characterization. The SBS test setup is proven to be able to measure all constitutive properties in 3D, but only by using line and point measurements, along with closed-form solution equations. The full-field strain measurements provide more information than traditional "point" strain measurement techniques, which are not used.

The PhD theses of Y. He [6] and P. Carpentier [5] will serve as the foundation of this continued research and are therefore of utmost importance. This Masters thesis will continue to employ mostly the same principles to characterize the material. The test setup and the DIC processing will be left as is. In the thesis of Carpentier, an analytical expression is used to calculate the material properties from the strain measurements. In the thesis of He, the shear stress approximation is replaced by accurate stresses from FEA. This thesis will combine the best of both of these theses. The analytical method is reviewed to make a first estimate for the FEM model, which is used to update the relevant material properties. This concept will be explored in greater detail in chapter 3. For the full methodology, see section 2.7.

The tools as developed by Dr. Yihong and associates will be further refined [4][22]. These tools include a FEM model and User Material Subroutine, which are used in a Finite Element Model Updating technique to find the shear non-linear parameters (See section 2.4). This FEMU approach has not been applied to axial and transverse strains. The thesis will build upon these tools to more accurately determine the constitutive model.

2.4. MATERIAL PARAMETER CHARACTERIZATION; THE INVERSE PROBLEM

Calculating material properties from strain measurements is often cited as an inverse problem [23–26]. In a direct problem the geometry, loading distribution, and the material model are known and the calculations solve for stresses, strains, and displacements. This is how a structural analysis or Finite Element Model works. In this case, the inverse for this problem has to be solved: starting with the strain measurements, geometry, and loading configuration to find the material parameters. For homogeneous stress states, these equations are often available. For instance, the axial stiffness of tensile specimens is found using the measured strain, specimen cross-section, and load. Heterogeneous stress states can be achieved by various load cases, notches, holes, and stress concentrations. For these stress states (where the stress state is not constant), the inverse problem is not straightforward and closed-form solutions are not always available.

The homogeneous stress states allow for an accurate characterization of one or maybe two material parameters. A heterogeneous stress state offers the analyst the option to determine multiple properties. Since optical measurements of deformation depict a 2D strain field, it is preferable that the test method finds all the constitutive properties of a material in 2D as well. Which parameters these are, is dependent upon the plane of loading. The inverse method would be able to find the relevant material parameters while taking into account more complex loading configurations and material models (including the Ramberg-Osgood). From literature, there are several methods to solve the inverse method [26].

1. Closed-form solutions
2. Virtual Fields Method (VFM)
3. Finite Element Model Updating method (FEMU)
4. Constitutive Equation Gap method (CEGM)
5. Equilibrium Gap method (EGM)
6. Reciprocity Gap method (RGM)

Closed-form solutions are the most obvious. Using an established relation between material properties and strain, the material properties are calculated. For the conventional test methods, these relationships are present. For the heterogeneous stress states, these closed-form solutions are often not available.

The Virtual Fields Method [27] uses virtual fields to extrapolate relationships between deformation and material properties. Integrating these virtual fields and the strain measurements provides a linear system which can be solved to give the material parameters. This method is highly appropriate and does not require a Finite Element Model, leading to reduced cost. Unfortunately, the virtual fields are assumed. Optimal virtual fields are hard to achieve and require a lot of validation [28]. Next, it is a linear method, so the shear model has to be

linearized, which will degrade the quality of the results. Furthermore, the response is integrated from the entire front surface, which includes the insecurities under the stress concentrations and local damage effects. As the axial response is integrated, no difference can be discerned between tensile /compressive moduli. Lastly, the performance of the method is very dependent upon the resolution and quality of the DIC speckle pattern. This has the following two drawbacks. First, the DIC method integrates multiple speckles to define the strain field. Therefore, there is no data at the edges, which renders the result more unstable. Secondly, the noise in the data is very significant in low strain measurements. In the current SBS setup, the transverse strains are very small with respect to the shear strains. Therefore, the determination of the Poisson's ratio would be very inaccurate.

The FEMU method is applied by a lot of researchers and is shown to have great performance, albeit with high computational cost [24, 25, 29, 30]. The FE model is run with an initial guess for the material parameters and the output strain is compared to the DIC strain. Using a sensitivity matrix, the FE model is rerun with a new set of properties which are closer to the solution. The model keeps iterating until convergence is reached. This convergence is often a least-squares fit between the strain fields.

The CEGM, EGM, and RGM are variations on the VFM method. The Constitutive Equation Gap method was used previously to verify Finite Element simulations. In the past several years, applications to material parameters identification have been discovered. The method relies on defining statically admissible stress fields and is therefore similar to the VFM [31]. Therefore, it is also subject to the same drawbacks. The Equilibrium Gap Method is similar and can be seen as an equivalent of the VFM with piecewise particular fields [26]. The Reciprocity Gap method is another variation, employing kinematic fields on the boundaries. So far, no reference is known where this method has been applied to test data.

There are various combinations of the aforementioned solutions to find material properties. One can combine various ways to process strain measurements with inverse parameter characterization methods. For instance, closed-form solutions can aid the FEMU method. For the Short Beam Shear method, there are no closed-form equations to determine the entire stress/strain field available. There is a trade-off between the FEMU- and VFM-like methods. Due to the aforementioned reasons, the FEMU method has higher accuracy and flexibility, albeit at a greater computational cost. The FEMU method has already been applied for the non-linear shear response [4]. Therefore, it is logical to continue this work.

Optical strain measurements are very important for the inverse problem. The full strain field often incorporates hundreds of data points, which represent a lot more data than strain gauges can provide. The strain measurements for the inverse method have to be of good quality to accurately characterize the material. There are multiple options available, including Moiré interferometry, Digital Image Correlation with speckle or grid patterns, photo-elasticity, or X-Ray stress analysis. Digital Image Correlation is a popular choice with good performance. VIC3D software processes speckle pattern images to create fields (matrices) with the values for the different strain components. However, this output is dependent upon the filter size to render the data more smooth. Unfortunately, this data is inherently noisy, necessitating smoothing. There are different methods to post-process the DIC data, which may have to be combined.

- Varying the filter size for increased/decreased smoothing.
- Match Finite Element nodes using bi-linear interpolation [25]
- Parameterizing the DIC strain output using Artificial Neural Networks [32] or other least-squares solutions, like Multi-Layer Perception Networks [33].

2.5. STATISTICS IN MATERIAL PARAMETER CHARACTERIZATION

Statistics represent a large topic in industry. For design purposes, the material allowables and constitutive model have to be well-known. However, the measurement results will always show variation. This variation is due to variations in material quality, measurement accuracy/noise, and production inconsistencies. Section 2.2 previously discussed that the generation of material parameters takes many specimens to gain confidence in the specified parameters. It has already been mentioned that the proposed SBS method reduces

the number of different mechanical tests required to characterize the material. However, can the number of coupons necessary per test method be reduced?

A DIC strain field has hundreds of data points, instead of just a single one that a strain gauge would give. The strain field generated by the DIC method is inherently noisy. By applying multiple point measurements in a noisy field, one may find the material properties are different depending on where you go. Gurvich shows an example in which the noise in the DIC method is characterized [34]. This noise is very much dependent upon the picture resolution, the speckle pattern the deformation field and the processing [17]. One may characterize this noise and gain confidence in the test performance. This may be used to aid the statistical database of tested specimens, but may not be used to directly make conclusions about material properties. If a statistical distribution is created, the analyst is most likely specifying noise instead of stiffness variability. Most material parameter identification methods (FEMU, VFM) won't deal with this at all, because all measurement points are integrated to come to a solution [7, 25].

Therefore, it is imperative for this thesis to look into the matter of DIC noise. Spatial variability of stiffness, statistics and noise will be very hard to distinguish just from a surface field. It might be more significant if DIC noise is used as a threshold value for which a homogeneous material model can have varying stiffness. Appendix B elaborates on this idea.

2.6. SPATIAL VARIABILITY OF MATERIAL PROPERTIES

In the introduction, the spatial variability of material constitutive properties is defined as "The change in the stress-strain relationship over the surface measured using DIC". There are many causes for variability in material properties [18]. These vary from material batch to batch and even within panels. In one example the mixture rule was used to define stiffness variability [35]. Furthermore, ply waviness, inclusions and voids, broken fibers and curing phenomena increase the variability. One method to characterize this variability is by defining a heterogeneous material model. As the material model can be defined locally, this method is suitable for damage identification [36–38].

Another definition of spatial variability could be "The change in axial and shear stiffness over the surface measured using DIC". A homogeneous model can be applied to define a stiffness map [39]. The material model with non-linear shear strain response and bi-modular axial stiffness will give a varying "apparent stiffness" over a surface. Tensile/compressive regions will clearly show a changing stiffness and regions of higher shear strains will give a lower shear stiffness value. Note that the actual material model does not change over a surface. It does show the more compliant and critical regions through the thickness. This definition and method is practical; for structural analysis it is important to know how the stiffness might vary with loading and location. However, this thesis aims to characterize the material model (parameters). Therefore, a stiffness map is not very significant. More on this topic can be read in Appendix C.

There are 8 conceptual methods found for generating a spatially varying material model. These range from VFM-like methods to single point calculations.

1. The FEMU model can be used, applying material sections that are allowed to change [38], or applying a spatial field as a function of the coordinates in UMAT/node creation. The big challenge would be the convergence criterion to define this spatial field. This method will have the greatest flexibility with respect to modeling.

2. The Virtual Fields Method has been applied for damage characterization [37, 39]. The authors distinguish between discrete and continuous variability. Both have their pros and cons with respect to accuracy and sensitivity. A continuous spatial field will have low spatial resolution, but can find areas of lower stiffness. The discretely changed area has higher sensitivity, but the results change on how the surface is partitioned. The drawbacks mentioned in section 2.4 on the VFM method still apply.

3. A point-by-point or least-squares solution can be applied. This will involve some form of stress approximation or closed-form solution and will likely be hard to distinguish from noise.

4. VFM-like methods have a lot of potential. The following four concepts are under development by Florentin and Lubineau, which partition the measurement surface and create virtual-fields like equations. The Constitutive Equation Gap Method [31], the Global Equilibrium Method [40], the Equilibrium Gap Method, and the Constitutive Compatibility Method [41] are used to identify the areas of increased stiffness, as is validated using FEM output strains. The performance is good and does not require an FEM model. However, currently it has only been applied to simple material models and loading configurations. See Figure 2.8.

5. The last method is the simplest: Cutting multiple coupons from a larger panel [42–44]. The resolution is very low, and varies within a panel, but not within a coupon.

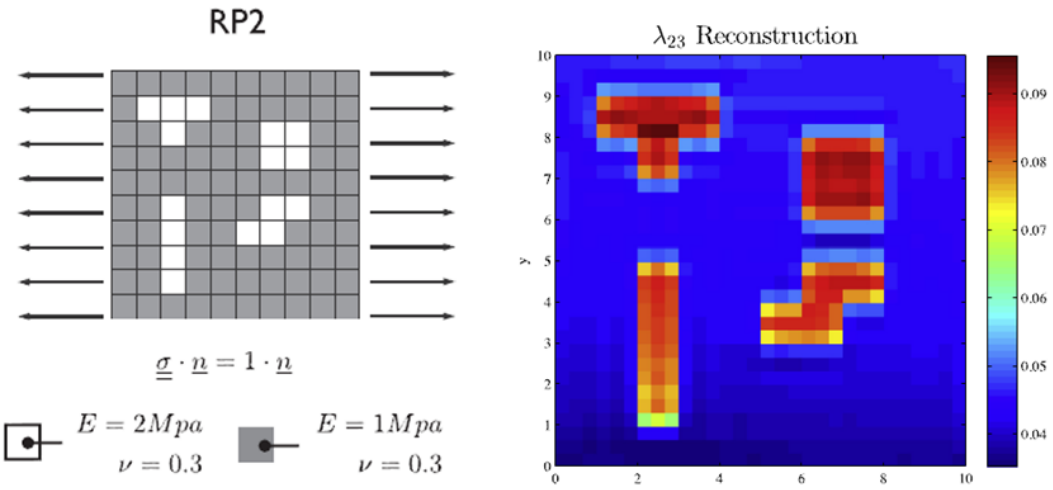


Figure 2.8: Heterogeneous material model in FEM (Left). Reconstruction of the contrast of shear modulus resulting from identification with Dirichlet boundary conditions in CCM (Right)

Another consideration is how the spatial variability is defined. Is it a point value, a discrete region, or a continuous spatial field? The pros and cons have already been mentioned in this section. Continuous responses have the lowest resolution, but will show where the more compliant and stiff regions are. Point calculations may be the simplest to apply depending on the situation, but are most noise sensitive.

2.7. SCOPE AND OBJECTIVES OF THE THESIS

This MSC thesis will build on the SBS method as designed by Makeev et al. [1] by focusing on applying spatial variability in the short beam shear test specimen. There are other test set-ups known that can identify all 2D material parameters in a surface, but the SBS is the first attempt to measure all 3D constitutive properties in one test setup, without making any ad hoc assumptions on the constitutive model and the stress field. This will be the first attempt to update all 2D material properties using the FEMU program and to define spatial variability of the shear stress-strain curves to validate the material model. The research objective is given as:

"To accurately determine the constitutive model of composite uni-directional static short beam shear test specimens, by (a) characterizing the constitutive model from DIC surface strain measurements by applying the FEMU approach and (b) using the stress field from FEM and strain measurements from DIC to define spatial variability of shear non-linear parameters over a surface and (c) determining whether the SBS set-up can be used to model coupling phenomena between shear and transverse stresses in the non-linear regime"

Using the research objective, different research questions are stated. Ultimately, a hypothesis has to be tested. The SBS coupons are very small; the thickness of the coupons is a quarter inch. This reduces the chance that manufacturing effects are present and thus maybe one material model will define the stiffness variations

over the surface sufficiently. There is a chance however, that the matrix deforms plastically under the loading nose. Such non-linear matrix compression is something that is not modeled in the FEA. Furthermore, it is interesting to investigate whether known manufacturing defects show a changing strain field. Therefore, the null hypothesis will be: "The material model as used by the AMSL lab at UTA is correct and spatial variability of shear stiffness properties will not exceed noise levels." This will be rejected if the research shows that locally the stiffness values differ too much from the converged material model, including noise from the DIC method. The research questions are as follows:

1. Using the Finite Element Model Updating approach, how do the constitutive properties of the SBS specimens converge?
2. If the full-field strain measurements from DIC of an SBS specimen are compared with the output strains of an FEA model, can the variation of the shear non-linear material properties over the surface be specified?
3. Can the SBS test method be used to investigate extra coupling terms in the shear non-linear regime?

The scope of this thesis must be limited to a 9 month duration. Work will be centered on UD GFR epoxy and CFR epoxy materials. Because this thesis combines multiple aspects (test methods, full-field strain measurements, finite element analyses), only known technologies will be used. The test method is not necessarily non-destructive, but failure criteria will not be taken into consideration. The AMSL has access to all previous raw test data including tensile, compressive, Iosipescu, 4-point bending, curved beam and SBS test data for glass and fiber epoxy unidirectional coupons. Processing options using the commercial DIC software "VIC3D" is available. Outside of the scope is the set-up of the SBS fixtures/specimens and the DIC camera system. Also, no investigations will be performed on the influence of DIC filtering. The existing guidelines and suggestions are used to create the strain fields. The X-ray Computer Tomography is not of importance to this thesis and is thus also out of scope. What is included in the scope is the formulation of the material model, the interpretation of the strain field, the Finite Element Models and modeling approach and lastly the post-processing of the results.

Because of the frequent use in the aerospace industry, it is interesting to focus on glass fiber and carbon fiber reinforced epoxy unidirectional coupons. The AMSL has amassed a database of measurements on S2-glass/E773-epoxy, S2-glass/8552-epoxy and IM7-carbon/8552-epoxy tape coupons for all material directions. From this data, several test runs will be chosen in either the 1-2 or 1-3 material directions. From these, it can be argued, that the results are valid for glass and carbon fiber reinforced epoxy tape material, which are common for aerospace. The chosen assumptions (linear axial strain, non-linear shear strain, etc) indicate that the method might be valid for fiber reinforced UD thermosets with high enough fiber volume fraction.

During the thesis, a lot of emphasis will be placed on verification and validation. When applying point calculations over a surface, there are many factors that can cause the stiffness parameters to change spatially. The plausible causes have to be taken into consideration as specified in Table 2.1. The parameters may appear different because the accuracy of the test specimen is not perfect. Compressive tests on near-perfect specimens give a simple stress field to quantify the DIC-method induced noise (see appendix B). Another possibility is the inclusion of manufacturing defects. CT-scans (x-ray) give 3D images, showing structural flaws, such as voids and ply waviness. Scans have shown that most SBS specimens are smooth and the defects are negligible. Certain specimens have purposely added production defects, but these are avoided in this thesis. If the material model is wrong, the spatial variability and coupling analysis might pick up on this.

The AMSL lab uses the FEMU approach, using an Abaqus model in Python and DIC strain measurements with VIC3D software. This method is preferable over the VFM method, due to its flexibility, accuracy and robustness. The model is aided by closed-form solutions in order to achieve fast convergence. The inverse parameter identification method is already partially implemented at UTA [1], but has to be parametrized in Python and expanded to incorporate all constitutive properties, nonlinearities, and potential transverse/shear coupling.

Figure 2.9 gives the concept of the experimental set-up. The speckle pattern images are used to generate the strain data for both the material parameter characterization and the strain fields to quantify the spatial vari-

Causes Spatial Variability	Action
Production errors	Perform X-ray scans
Natural spread in material properties	Perform a batch run with multiple specimens
Geometric imperfections	Are not determined
Wrong material properties	Apply FEMU Method for a batch of SBS Specimens
Wrong material model	Coupling Analysis in non-linear regime, relate FEMU results to other mechanical tests
FEA model mesh is bad	Mesh Convergence study
Wrong contact stresses	FEA contact verification
DIC Measurement Accuracy	Compressive tests to quantify DIC noise

Table 2.1: Validation Measures for Causes of Spatially Varying Mechanical Properties

ability of stiffness. Using the strain measurements, the geometry and the loading data, the material properties are estimated and then used as a starting point for the material iterations in Abaqus/CAE. The converged material model is then used in a more refined model to generate a fine and accurate stress field. Both the DIC strain fields and the FEM stress fields are input for the spatial variability analysis.

The methodology for the spatial analysis is described in section 4.2. It is primarily based on axial and shear stress (from FEM) and strain (DIC) data across the different frames (load levels). These are combined to form stress-strain curves, from which material parameters can be extracted. Using carefully selected points offers the option to track the different stress components, but also a surface of nodes can be processed to generate a field of spatially varying stiffness properties. This latter gives more statistical insight in noise and accuracy of the method.

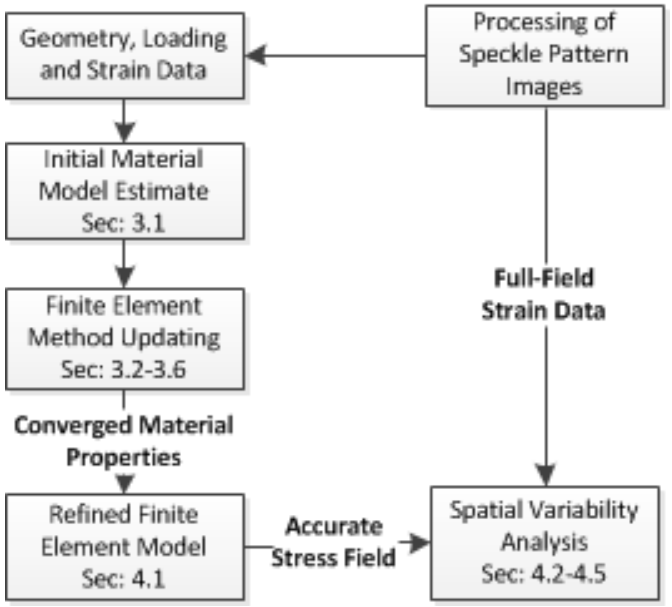


Figure 2.9: Concept Experimental Set-up

The first models are created in Abaqus/CAE, which is a commercial tool which is already widely used in industry and education. For the modeling, the Python language is used. This object-oriented language has a good interface with Abaqus and is very easy to debug. The AMSL lab at UTA has a lot of experience modeling with Python and Abaqus/CAE. The material model is defined as a User Material subroutine in Abaqus/CAE and is programmed in Fortran. This material model will include all the constitutive parameters as defined in section 2.1 and will also be used for the investigations in the material model (see chapter 5). The VIC3D software is used to extract strain measurements from speckle pattern pictures.

For the final post processing, which is very mathematical, Matlab is chosen. This program is very suited for large and complicated calculations and operations. It is widely used commercially and at TU Delft. Because

multiple models have to be created, there will be some time constraint on how many test specimens can be analyzed.

3

FEM UPDATING METHOD

This chapter will discuss the Finite Element Model Updating (FEMU) method, starting from the SBS test method and an analytical first estimation of the material (section 3.1), through the description of the Finite Element Model (section 3.2) and the User Material subrouting (section 3.3), to explaining the architecture of the FEMU model (section 3.4) and how it works (section 3.5). Finally, the performance is given in section 3.6.

3.1. ANALYTICAL SOLUTION FOR THE MATERIAL CHARACTERIZATION

This thesis builds upon the previous works by Dr. He and Dr. Carpentier [5, 6]. As such, the SBS test setup, including the mechanical fixtures and specimen dimensions, the speckle pattern processing, and the analytical analysis are mostly unchanged. For understanding of the FEMU method, this procedure will be discussed. Note that the SBS method is different from the ASTM standard D2344 [21].

The Short Beam Shear specimens are small and have very simple geometries. This makes them some of the most affordable specimens to create. The specimen and test setup can be seen in Figure 2.6. The cross section is rectangular and constant, with a length to width ratio of 5-7. Quarter inch thick specimens are standard and the supports are 1.2in apart. These values must be scaled together, so that the specimens fail in shear and not in tension or compression. The supports have a .125in radius and the loading nose radius is increased to 2in or 4in to apply a smoother loading and prevent the specimens failing in compression. This radius is different for GFRP and CFRP and can be reduced if the specimens are really small. The nose has no effect on the identification of material properties, but it does change the strain field locally.

The specimens are cut and loaded in the material principal planes (see figure 3.1). The plane notations are as follows: The first number is the horizontal axis and the second number is the vertical axis. Direction 1 stands for the fiber direction, 2 is the in-plane transverse direction, and 3 is the laminate-thickness direction. In this figure, specimen A can be loaded in the 1-2 plane and loaded in the 1-3 plane by simply turning the specimen over. Specimen B can be loaded in the 2-1 and 2-3 plane. Specimen C can be loaded in the 3-2 and 3-1 planes. The last specimen is considerably more expensive to produce, as it requires a very thick panel with many plies. These specimens will thus generally have smaller dimensions.

The three-point bending configuration induces a high shear force and bending moment. This induces high gradients of shear strain and axial strains, but the transverse strains are generally lower due to the insignificant transverse stresses. The axial strains allow for a quantification of the axial stiffness parameters. Because the shear strains are highest at the neutral axis, there is a region of pure shear strain, which allows for accurate quantification of the non-linear shear parameters. Because the transverse stresses are close to 0 (if the aspect ratio is large enough), one may assume that the transverse strains are induced by the Poisson's ratio [5]. Thus, for a plane loaded in the x-y plane, it will be able to find 6 different material properties.

1	Compressive axial stiffness	$E_{xx,T}$
2	Tensile axial stiffness	$E_{xx,C}$
3	Poisson's ratio	ν_{xy}
4	Shear stiffness	G_{xy}
5	Secant-intercept modulus	K_{xy}
6	Exponent	n_{xy}

Note that if SBS coupons are tested in the 1-2, 1-3, 2-3 and 3-2 planes, the entire stress-strain constitutive model would be characterized. Unfortunately, the SBS coupons that are not 1-2 or 1-3, will fail under the bending stresses at low strain levels. Therefore, these specimens fail before the shear non-linear response can be characterized and thus the secant intercept modulus and the exponent cannot be determined. 3D material characterization by 2D measurements is only valid if these parameters are uncoupled. At the locations of strain measurements in SBS specimens, the stress components in width and transverse direction are negligible, so this assumption is valid. Figure 3.2 shows which material properties can be calculated from which planes. On the positive side, the SBS test method is destructive and can therefore also measure failure loads. The specimens loaded in 1-2 and 1-3 planes fail in pure shear and thus give the shear strength (see figure 2.7). Other specimens fail in tension at the bottom of the specimen underneath the loading nose, thus giving the tensile strength in xx; A coupon in 2-3 plane can specify the transverse tensile strength and in 3-2 can specify the inter-laminar tensile strength.

The coupons are set in a custom test fixture. This text fixture is shown in figure 2.6. It allows for a variable support distance and has an alignment tool so that the nose is almost exactly in between the supports. The test is performed in a servo hydraulic load frame, at a displacement rate of 0.05in/min nose vertical displacement. To perform the optical strain measurements, the lab has several stereo imaging camera systems of 5MP and 16MP resolution. A speckle pattern of black on white is applied to the surface of interest, of which the speckle size is dominated by the resolution of the camera. Two bright lights illuminate the surface to create the desired contrast between the speckles and between the specimen and its background. The images which are taken are analyzed using the VIC3D software. The subset and filter size are chosen according to the size of the speckles and resolution of the camera. The DIC method calculates the deformation field by tracking the speckles. This deformation field is processed to generate full-field strain measurements, which are exported as a matrix of evenly spaced strain values. The total number of data points in a strain field is several thousands. These are exported in a comprehensive .CSV file or .MAT file for exportation into Excel or Matlab.

With the strain fields known, it is now possible to make a first estimation of the material properties. The significant measurements are taken from a cross-section halfway between the loading nose and the supports, which gives a strain distribution as expected from shear loading, without the effects of stress concentrations. Figure 3.4 shows that the shear strains become parabolic and the axial strain data linear at this cross-section, which agrees with beam theory. The calculations on the axial stiffness depend greatly on the neutral axis. If the compressive stiffness is lower than the tensile stiffness, the neutral axis shifts away from the middle line. This shift is usually very small and therefore, this value is suspect to noise in the DIC measurements and any alignment issues. A slight error in the coordinate system in VIC3D gives a neutral axis which deviates greatly from what is expected. A rotation would make the shift in neutral axis significantly bigger at one side and significantly smaller at the other. Therefore, this effect has to be corrected before the initial analysis [5](See appendix C.2).

As mentioned before, the strain data is taken at the cross-section halfway between the loading nose and the support. One frame gives sufficient information to characterize the axial stiffness and the Poisson's ratio. The frame needs to have sufficient load to decrease the DIC noise, but has to be well below the failure load. From this vertical section, the axial, transverse, and shear strains are taken, averaged over a 2mm horizontal gauge length. The notation of the coordinate system and the linear representation of the axial strains at this coordinate system are represented in figure 3.3.

The analytical solution for the first estimate is different from what is explained in Reference [4]. The difference is that the two data sets, left and right, are used together to solve for the material properties. Figure 3.4 shows a static analysis of the SBS specimen, including a shear force (V) - and bending moment (M) diagram. The cross-sectional data is taken from $L_L/2$ and $L_R/2$. Taking the bending moment at the right support gives

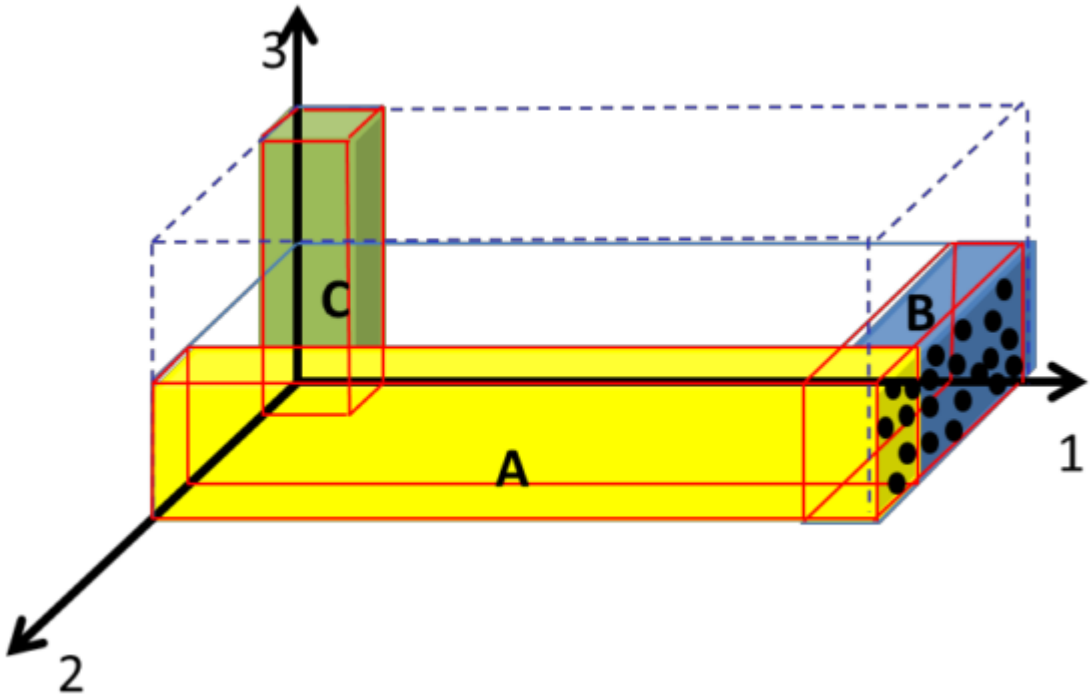


Figure 3.1: Different Options to Cut SBS Coupons from a Plate [5]

equation (3.1), from which the reaction force at A can be calculated (3.2). Similarly, the reaction force at B is found (3.3). The maximum bending moment is found using equation (3.4). Observing the bending moment diagram, it shows that the bending moment at the relevant cross-sections is equal, regardless of whether the loading nose is right in the middle or not (3.5) [45].

$$LR_L - PL_R = 0 \tag{3.1}$$

$$R_A = \frac{PL_R}{L} \tag{3.2}$$

$$R_B = \frac{PL_L}{L} \tag{3.3}$$

$$M_{max} = R_L L_L = \frac{L_R L_L}{L} P \tag{3.4}$$

$$M_L = M_R = R_L \frac{L_L}{2} = R_R \frac{L_R}{2} = \frac{L_R L_L}{2L} P = \frac{L_R L_L}{2(L_L + L_R)} P \tag{3.5}$$

Parallel to this static analysis, the DIC strain measurements are processed as follows. Equation (3.6) shows the linear approximation of the axial strains. Note that the neutral axis is given by $y = -b/\kappa$.

$$\epsilon_{xx} = -\kappa y - b, \qquad -\frac{h}{2} \leq y \leq \frac{h}{2} \tag{3.6}$$

where x is the distance from the support and P is the applied load. For the initial estimation of the tensile and compressive stiffness, equation (3.7) is used.

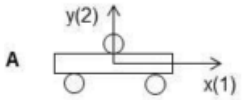
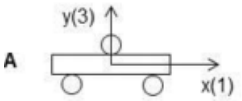
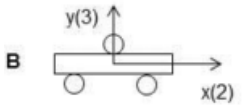
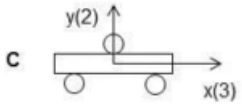
Material Plane	Measured Properties
A 	Axial Tensile Modulus, E_{11T} Axial Compressive Modulus, E_{11C} Poisson's Ratio, ν_{12} Shear Modulus, G_{12} Secant Intercept Modulus, K_{12} Exponent, n_{12}
A 	Axial Tensile Modulus, E_{11T} Axial Compressive Modulus, E_{11C} Poisson's Ratio, ν_{13} Shear Modulus, G_{13} Secant Intercept Modulus, K_{13} Exponent, n_{13}
B 	Axial Tensile Modulus, E_{22T} Axial Compressive Modulus, E_{22C} Poisson's Ratio, ν_{23} Shear Modulus, G_{23}
C 	Interlaminar Tensile Modulus, E_{33T} Interlaminar Compressive Modulus, E_{33C} Poisson's Ratio, ν_{23} Shear Modulus, G_{23}

Figure 3.2: Testing and Processing the SBS Specimen in Different Planes results in different Material Constitutive Properties [5]

.

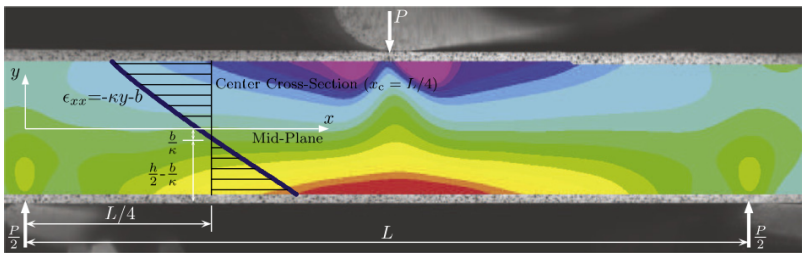


Figure 3.3: Coordinate Notation and Axial Strain Distribution in the SBS Specimen

$$E_{T,C} = \frac{M}{\kappa I(1 \mp a^2)}, \qquad a = \frac{2b}{h\kappa}, \qquad I = \frac{wh^3}{12} \tag{3.7}$$

where $wh^3/12$ is the moment of inertia, κ and b are the slope and intercept of the axial strains, w is the specimen width and h is the specimen thickness. Note that as E_t is equal to E_c, the intercept b would be negligible and the solution converges to $M/(\kappa I)$.

The shear strain values are taken at the same cross-section (at x = L/4), at y=0. In this region, the axial strains are approximately zero, and the shear stress is maximum and pure. Therefore, beam theory is used to approximate the shear stress as in equation (3.8). However, in order to get a more accurate initial estimate, equation (3.9)[5] is used to get a more accurate first estimate of the shear non-linear properties. The equation shows that the longer the aspect ratio, the more accurate the closed-form solution becomes. The strain values are taken in this region, using a horizontal 2mm gauge length. This gauge length is taken to prevent local noise in the DIC measurements to invalidate the measurements.

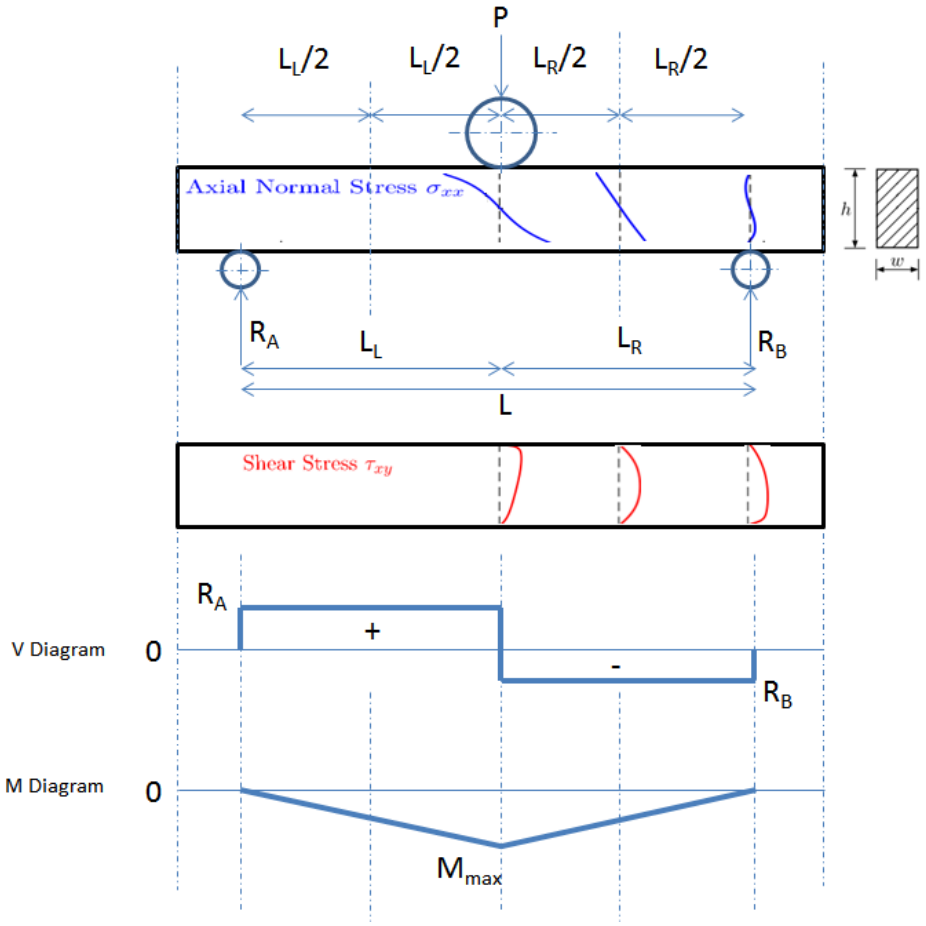


Figure 3.4: Static Analysis of the SBS Specimen

$$\tau = \frac{3V}{2wh} \qquad where \quad V = \begin{cases} \frac{L_R}{L}P, & \text{if } left \\ \frac{L_L}{L}P, & \text{if } right \end{cases} \tag{3.8}$$

$$\tau = \begin{cases} \frac{3V}{2wh}, & \text{if } \frac{3P}{4wh} \leq 6800 \\ \left((.03(\frac{L}{h}) + .6)\left(\frac{3V}{2wh} - 6800\right)\right) + 6800, & \text{if } \frac{3P}{4wh} < 6800 \end{cases} \qquad where \quad V = \begin{cases} \frac{L_R}{L}P, & \text{if } left \\ \frac{L_L}{L}P, & \text{if } right \end{cases} \tag{3.9}$$

Using the strain measurements at this location for each load frame, a stress-strain response is generated, which is used to estimate the shear stiffness parameters G, K and n. The corresponding equations have already been introduced in section 2.1.

Lastly, the Poisson's ratio is evaluated. The transverse stresses are small, but definitely zero at the outside edge. Therefore, the Poisson's ratio would be most accurately characterized at the outside edge, using $\nu = \epsilon_{yy}/\epsilon_{xx}$. Yet, the VIC3D software creates a lot of noise at these edges and therefore this method is not particularly useful. In the thesis of Dr. Carpentier, the Poisson's ratio is determined by minimizing the error of $\epsilon_{yy}/\epsilon_{xx}$. More consistent results are found by plotting ϵ_{yy} over ϵ_{xx}, specifying a linear section and taking the slope of the section. This allows the user to disregard edge effects from the DIC software. This is explained in figure 3.5.

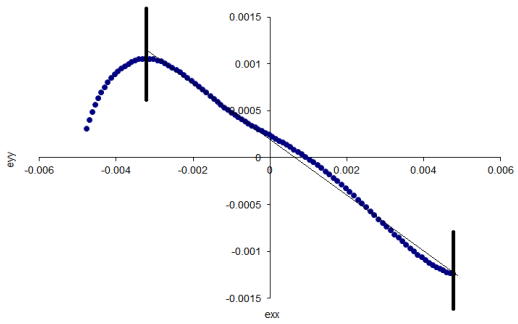


Figure 3.5: Transverse vs Axial Strains. Defining a linear section in this model is representative for the Poisson's ratio. In this figure, $\nu = 0.3$

3.2. THE NUMERICAL MODEL IN ABAQUS/CAE

This section describes the FEM model of the SBS test static set-up. As the composite material reacts non-linearly, equation (3.8) overestimates the shear stress (see figure 3.13). Since the accuracy of the initial stress estimation of the closed-form solution is not satisfactory, a Finite Element Model is created to characterize those stresses more accurately. The initial model from Dr. He [4, 6] was created using Abaqus, modeled in the input .INP file. This model was adopted with few major changes:

1. The model was recreated and parametrized using Python scripting. This allows this model to be versatile and usable for any size and material.
2. The original model as created by Dr. He was a half model. It was used to extract the shear stress at a specimen node. The current model takes stresses from both left and right for material characterization.
3. The original model had 10 discretization in the width direction. It was found that the material characterization does not change by reducing this number of discretizations to 5. This increased the efficiency of the program.
4. The reference coordinates are switched. z is now the width direction and y the thickness direction.

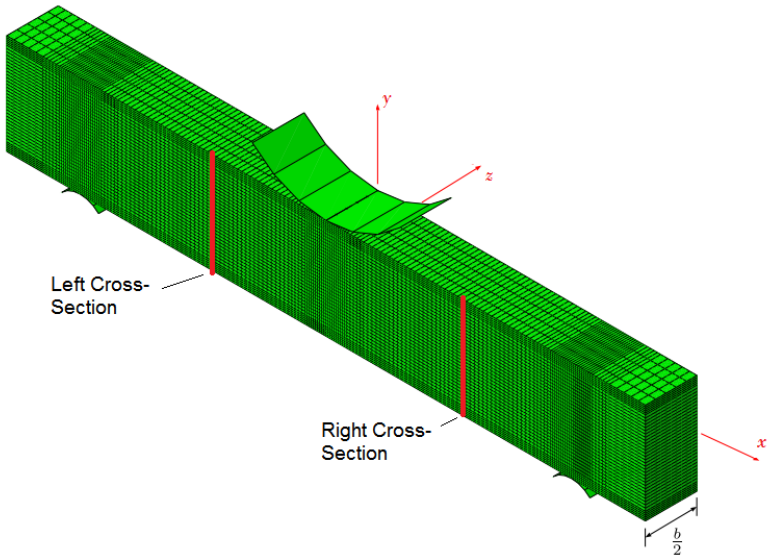


Figure 3.6: Typical FEM Model as Created by Dr. He [6], shown with changed reference coordinates

Figures 3.6 and 3.7 show the FEM model as created by Dr. He. The loading nose and supports are modeled by analytical rigid surfaces and the SBS coupon is a solid extrude with homogeneous sections. Its material

is modeled using a custom User Material (UMAT) subroutine in Fortran. As the material is anisotropic, the orientation has to be defined. This orientation corresponds with the loading plane and is thus parameterized.

To begin, a symmetry analysis was performed. Applying an extra symmetry plane would decrease running time, but it also decreases the information one can receive from the model. The model needs to give information on the stresses on the front surface, at the cross-section halfway between the loading nose and the support. This analysis is shown in figure 3.8. The full model (a) shows phenomena over the entire specimen, which is useful for intuitive verification purposes. Model (b) focuses on the front half of the specimen. Because the strain measurements are only taken on the front surface, this model does not change the results. These strain measurements are taken left and right, effectively generating two data sets. If the nose is well centered between the supports, it is possible and efficient to split the model in the length direction. Model (c) focuses on one data set (left or right) and as long as loading is symmetric, the results are unaffected. Model (d) has two symmetry planes and still converges on the same properties as the full model. It is thus the most efficient model to use for the FEMU program. However, the half model is used for the following reasons.

- The loading nose is never perfectly centered. This influences the material properties, as shown in section 3.1.
- Both data sets describe the same specimen and also the same material. With respect to geometry and loading, the data sets are identical.
- The strain data is never perfectly rotated. As mentioned, the neutral axis has a large influence on the axial moduli. This neutral axis rarely matches well between left and right. Using both data sets, an average neutral axis gives more sensible results

The meshing is shown in higher detail in figure 3.7. The mesh is refined along the top/bottom surfaces regions and under loading nose and supports. This allows the surface stresses and stress concentrations to be more accurately modeled. Effectively, there are different partitions along the length (x) and thickness (y). Zone T2 is coarser than T1 and zone L3 is coarser than L1 or L5 to save computational speed. Zones L2 and L4 are intermediate zones. R1 and R2 are the loading nose and support radius. h and L/2 are the thickness and distance nose - support. The discretization zones are scaled with respect to the length $L/2$ and h and seeded by number of elements. L1 is 12% and L2, L4 and L5 are 6% of $L/2$. T1 is 5% of h.

Equation (3.7) shows that emphasis on the neutral axis of the SBS specimens is large. Not only is it important to correct the coordinate system in VIC3D to measure the right neutral axis, one must also realize a small shift in the neutral axis leads to a large difference in the tensile/compressive moduli. One would expect that the discretization of the mesh needs to be very fine to capture this shift accurately. The number of discretizations along T2 (see figure 3.7) was increased from 18 to 28. This typically led to a change in tensile and compressive modulus of 0.4%. For efficiency reasons, the number of discretizations was returned to 18.

The final structured mesh consists of C3D8I elements, which have a good performance in bending dominated problems, removing shear locking and reducing volumetric locking. These linear elements show the same performance as quadratic C3D20R elements, with much shorter run times. Zones T1 and T2 are divided into 2 and 18 elements respectively. Zones L1, L2, L3, L4, and L5 are divided by 10, 3, 27, 3 and 5 element respectively. The width is 5 elements thick.

Figure 3.9 shows the quarter model with solid supports. The idea of solid supports is a more accurate representation of reality. If these bodies are deformable with generic isotropic steel material (E = 30E6 psi, ν = 0.29), the stress concentrations will be different. This change was <1% for all relevant stress values in the center region, but this difference was up to 5% right underneath the loading nose. As the effect of the stress concentration dies out before it reaches the area of interest, material characterization does not get any more accurate using solid supports. It is, however, interesting when considering the full strain field, for later research purposes.

The SBS specimen is only constrained by the symmetry plane. The supports are encastré and the loading nose is only free to move in y-direction. Underneath the loading nose, the freedom of the nodes to move

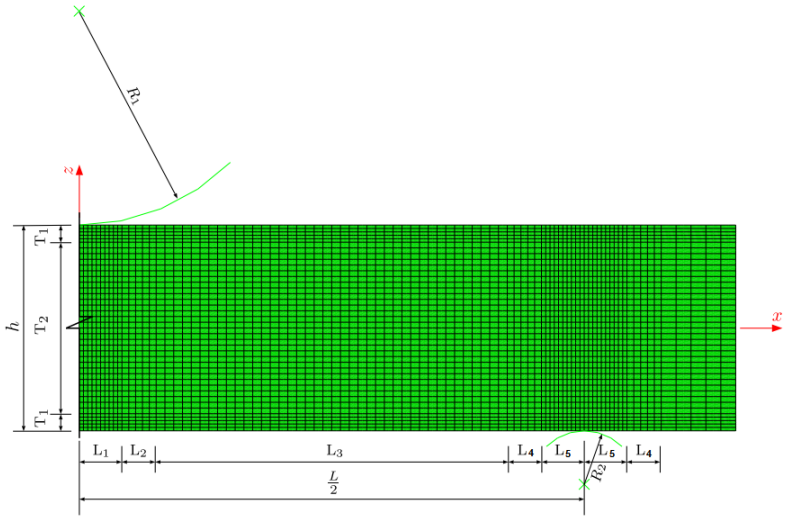


Figure 3.7: Schematic of Refined Mesh Regions in SBS Quarter Specimen [6]

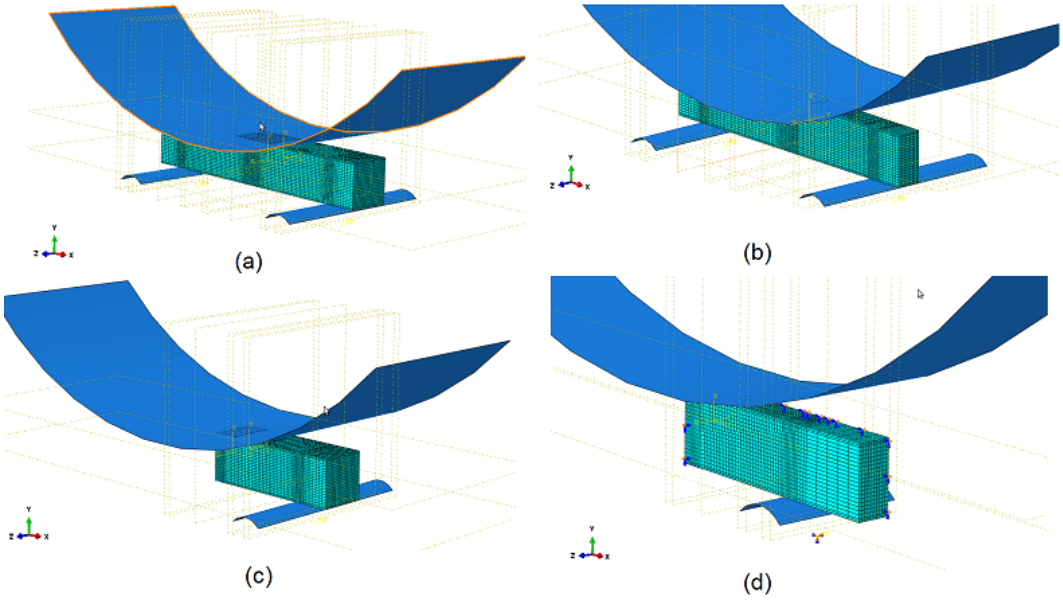


Figure 3.8: Symmetry Analysis SBS Coupons. (a) Full Model. (b) Front Half Model. (c) Right Half Model. (d) Quarter Model

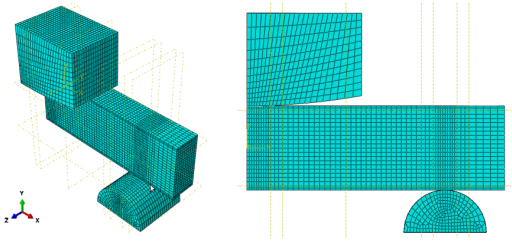


Figure 3.9: Quarter Model of the SBS Test with Solid Support and Loading Nose

in the x-direction is suppressed. The analytical surfaces make contact to the SBS specimen with a surface-to-surface contact definition. The contact properties are given penalty tangential behavior of 0,2 (friction) with maximum elastic slip of 0.005 and standard geometric properties. In order to improve contact stability, the contacts apply automatic surface smoothening and stability controls. Care is taken that the energy

dissipation due to these stabilization controls is insignificant.

The step is static, general with nonlinear geometry on. The step increments are linked to the loading data. A regular SBS test takes about 50 pictures. For each picture, the load is recorded. The maximum load is the applied load and the load per each frame will have a fraction of that load. These fractions are put in a timetable. The output is requested for each point in this timetable, which forces the step increments to match the timetable. This allows each frame in the output to match a picture from DIC. Because the problem is so non-linear, the step needs at least two increments per frame, which means the maximum increment size is about 1.0% to 1.2 %.

3.3. USER MATERIAL SUBROUTINE FOR THE NUMERICAL MODEL

As mentioned before, the UMAT from Dr. He [22] is taken adopted for this research. This UMAT was created in 2008 to incorporate non-linear shear. The cited source shows the UMAT in 2D, but is essentially the same in 3D. The programming is done in Fortran and is thus fully customizable. As the computing is done on Linux, the environment file is set to compile this Fortran code before the model is run and the UMAT object is placed in a scratch folder, conveniently selected to be in the work directory. This allows the user to take UMAT-created output files.

The UMAT has already been debugged and validated [4]. The UMAT will first define all variables and set all integer and double precisions. Next, it checks whether the user applies 3D elements and the correct amount of input parameters. Then it assigns the material input parameters to material specific properties. After that, it calculates the new shear stress in 12, 13 and 23, using the Newtonian method. Equation (2.1) is differentiated to produce (3.10). This derivative is also used for the Jacobian matrix. The new shear stresses are found using (3.11). Equations (2.2) and (3.10) are plugged into (3.11) to produce (3.12). The assumption of transverse isotropy is observed in GFRP and CFRP US specimens. It is not necessarily true for the 23 direction, but these properties are never measured for the SBS method. The non-linear response is added in all three directions, because under the nose the stress concentrations would drive the shear response into the non-linear regime. Therefore, the input parameters only ask for one set of nonlinear shear parameters K and n.

$$\frac{\delta\gamma}{\delta\tau} = \frac{1}{G} + \frac{\tau^{\left(\frac{1}{n}-1\right)}}{nK^{\left(\frac{1}{n}\right)}} \tag{3.10}$$

$$\Delta\tau = \frac{\delta\tau}{\delta\gamma} \cdot (\gamma_{new} - \gamma_{old}) \tag{3.11}$$

$$\Delta\tau = \frac{\gamma_{new} - \left(\frac{\tau}{G} + \left(\frac{\tau}{K}\right)^{\frac{1}{n}}\right)}{\frac{1}{G} + \frac{\tau^{\left(\frac{1}{n}-1\right)}}{nK^{\left(\frac{1}{n}\right)}}} = \frac{G\gamma_{new} - \tau - G\left(\frac{\tau}{K}\right)^{\frac{1}{n}}}{1 + \frac{G\tau^{\left(\frac{1}{n}-1\right)}}{nK^{\left(\frac{1}{n}\right)}}} \tag{3.12}$$

where γ and τ are the shear strains and stresses. G, K and n are the shear stiffness parameters as described in section 2.1.

In the last sections, the Jacobian matrix and the stresses are given. The Jacobian is simply the inverse of the compliance matrix as defined in (2.2). The shear stiffness is replaced by the derivative $\frac{\delta\tau}{\delta\gamma}$. The axial stresses are calculated by adding the product of the Jacobian and the incremental strain to the existing stress.

If the compressive and tensile stiffnesses are equal,the neutral line corresponds with the center line. This is properly simulated with the Short Beam Shear specimen. However, the FEM model will inherently create faulty strains if these two moduli are different. As observed, the neutral axis shifts down. The UMAT can choose its axial stiffness depending on the stress (or strain) state. In the section where the input parameters are assigned to material properties, the IF-statement below is included. This relatively simple statement shows the shift in neutral axis as expected.

```
IF (STRAN(1) > 0) THEN
    E11 = PROPS(1)
ELSE
    E11 = PROPS(2)
END IF
```

3.4. INTERFACE AND ARCHITECTURE OF THE FEMU MODEL

The purpose of this research was to create a tool for the AMSL lab, such that the material iterations can be applied to all of the SBS specimens. Per request, the analyst should not have to open the script and the tool should be operable for batches of experiments. So far, the half model is shown to be fully parameterized for any load test, which makes it suitable for batch processing. The actual process for performing the material iterations is as follows:

1. Specify the test data in an input file for each specimen
2. Open Abaqus/CAE and set the work directory
3. Spcify the input file and run main Python script
4. Find output files in Output/Specimen_name

To maintain a clean interface even during batch processing, the work directory will only include the .env environment file for Abaqus and any files created by running Abaqus. The environment file is necessary to tell Abaqus how to compile Fortran code. Step 1 has to be repeated for every specimen and the file is stored in subdirectory /input. The hierarchy and architecture of the FEMU model is a black box in this procedure, but operates as in figure 3.10. After the user performs his DIC strain analysis, it will have the information on geometry, loading, strain measurements and desired model properties. These input properties have to be entered in the input excel file in the work directory, which is shown in Appendix A. Sheet 2 of this file will specify for each picture frame the load and the shear strain value at the pure shear area. Sheet three contains the axial and transverse strains at the cross-section at L/4, halfway between the impactor and support. The model will recreate the initial stress and material estimate and then start the convergence loop. This while loop calculates the material properties first, then runs the model and performs the output analysis. After running the model, the FEMU program will create a folder (named after the specimen) in subdirectory /Output and store each output file in this new folder. This way, the interface does not get cluttered and each item will be easy to locate. The reader is referred to Appendix A, for more details on the interface and architecture of the FEMU model.

During execution, the FEMU program creates several temporary subdirectories for scratch data and the GUI. These are added to the directory for debugging options. They are deleted after the material properties are converged. Other files, like the .log, .msg, etc. are kept at the analyst's discretion.

There have been two main efforts to increase time efficiency in this model. First of all, the half model has reduced elements in the width to considerably speed up runtime without losing significant accuracy. Secondly, as the loop is programmed to run the half model after recalculating the material properties, it would run Abaqus after convergence. This gives the new strain field for the converged material properties, but by definition of converged, these strains will not differ significantly from the previous iteration. Therefore, a break statement will break the loop and the final output file will contain the FEM output strains of the previous iteration. Lastly, a bi-linear shear stress estimate provides a more accurate initial estimate, thus less iterations are required to converge.

3.5. MATERIAL PARAMETER ITERATIONS

The FEMU program is shown in more detail in figure 3.11. It focuses more on which feedback is received from the FEM program and how the variables are affected. First of all, the convergence criteria is given by (3.13).

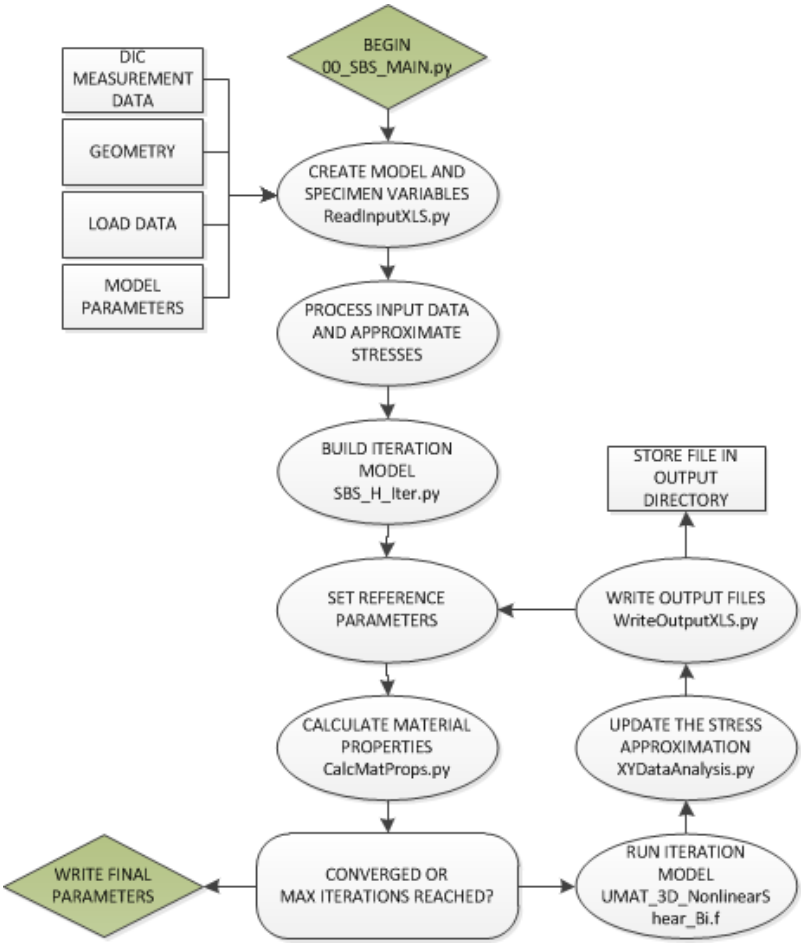


Figure 3.10: Overview of FEMU Program: Hierarchy and Architecture,

All material parameters are involved in reaching convergence, but the nonlinear shear parameters K and n are usually slowest to converge.

$$((G_{xy}/G_O)-1)^2+((G_K/G_{K_O})-1)^2+((G_n/G_{n_O})-1)^2+ \\ ((E_{xx_T}/E_{T_O})-1)^2+((E_{xx_C}/E_{C_O})-1)^2+((\nu_{xy}/\nu_O)-1)^2>Accuracy^2 \quad (3.13)$$

where G, G_K, G_n, E and ν are the material parameters, subscripts xy and O denote the measurement surface plane and reference value. These reference values are created arbitrarily at the start and later represent the previous loop. From the DIC measurements, the user is shown to need geometry and loading, $\gamma, \epsilon_{xx}, \epsilon_{yy}$ and Y-coordinates at the cross-section. With the first few parameters, the shear stress-strain response is simulated. With ϵ_{xx} and ϵ_{yy}, the Poisson's ratio is determined. Using geometry and loading, ϵ_{xx} and the Y-positions, the axial moduli are calculated. These calculations follow the equations in section 3.1 and are performed in a separate script, "'CalcProperties.py"'. It calculates G, G_K, G_n, E_{xx_T}, E_{xx_C} and the shear stress-strain response.

After the half model has run, the model runs another script called "XYDataAnalysis". It calculates: τ_{xy}, $\delta\sigma_{xx}/\delta y$, Neutral Axis in the FEA and $\delta\epsilon_{yy}/\delta\epsilon_{xx}$. It also updates the model neutral Axis and Poisson's ratio ν_{xy}. It does so by creating a path at the surface of the cross section of interest. Then, it extracts all relevant logarithmic strains and stress components, along with the undeformed Y-coordinates. Note that the FEM strains for axial and transverse strains are skewed near the edges. These edges cannot be measured by the DIC method and are thus left out of the linear regression analysis. Next, it extracts the shear strain values at

the node with pure shear for each frame.

- Using a linear regression of the axial strains at the cross-section, a FEM neutral axis is found. The neutral axis used for calculations "b" is scaled using the ratio $\frac{b}{b_{FEM}}$. If the FEM neutral axis is higher than measured, the ratio E_{xx_T}/E_{xx_C} is lowered until the neutral axis matches. For verification: A model run with $E_{xx_T} = E_{xx_C}$ and a long aspect ratio will not change its ratio (see section 5.1).
- The slope $\frac{d\sigma_{xx}}{d_y}$ is used to replace the initial stress estimate (Moment/Inertia). This may change the values for the stiffness moduli E_{xx_T} and E_{xx_C}.
- The slope $\frac{d\epsilon_{yy}}{d\epsilon_{xx}}$ is compared to the measured slope of the DIC measurements. Since these strains are dominantly caused by the Poisson's ratio, this ratio is changed to match the FEM and DIC slopes better.
- The node at which the shear stress τ_{xy} is taken (exactly at y = 0), may not be purely in shear. It is, however, close to pure shear and it is the same location that the measurements are taken from the DIC pictures. The FEM stresses are used to replace the assumption in (3.8). Using a regression analysis, G, K and n are found to match this measured curve.

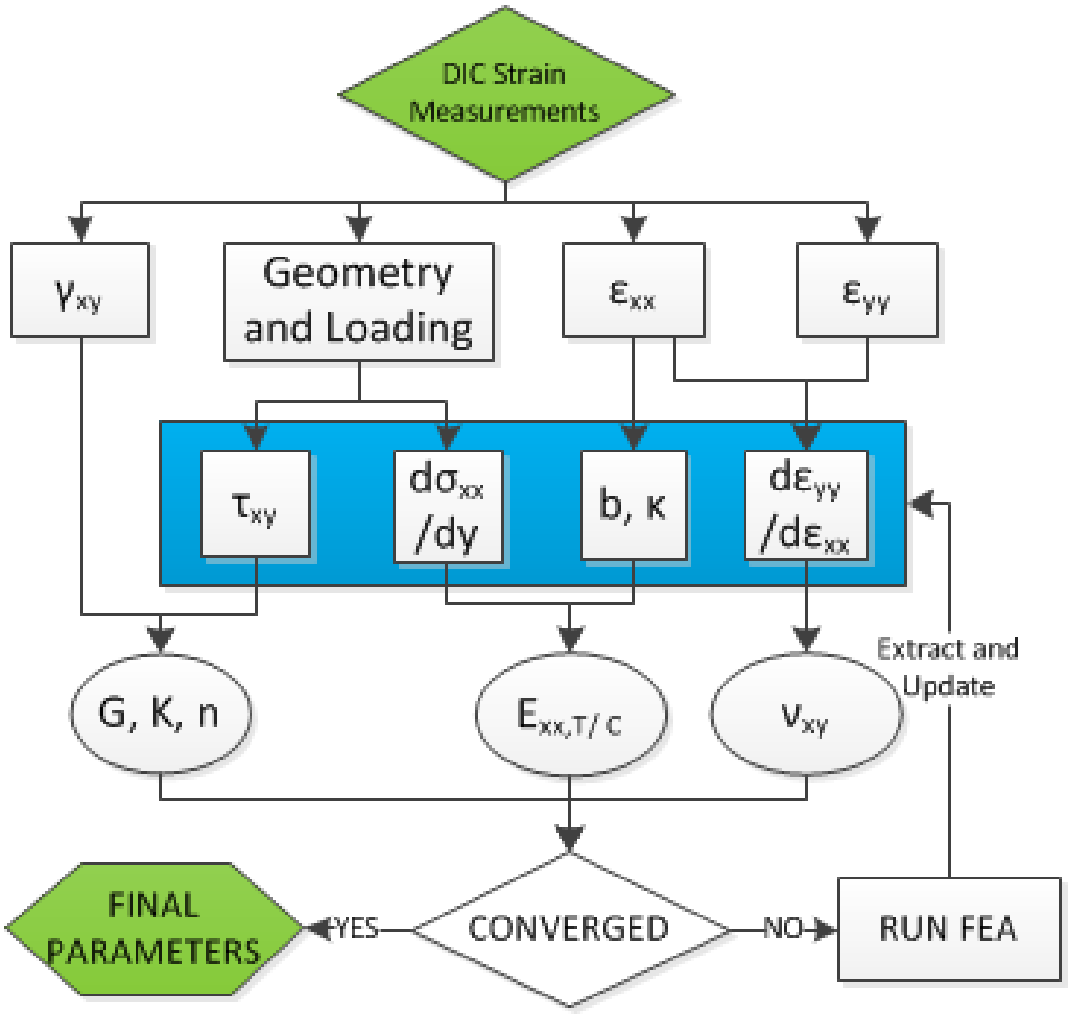


Figure 3.11: Overview of FEMU Program: How do Variables Update and how does that affect Material Parameters

Important to note is that the method described here converges two data sets at the same time. All variables are double and each set follows the exact same calculations. The material properties input in ABAQUS are chosen to be the average of the two data sets. This approach works very poorly for the axial moduli. Consider the

case where the left cross-section has a lower neutral axis than right. If the material properties are averaged, the FEM model creates a neutral axis which is likely just above the average, but below the higher neutral axis. When this happens, the lower neutral axis is diminished and the higher neutral axis is increased. This diverging tendency still results in converging average values for the axial moduli, but is intuitively wrong. The ratio of tension/compression would have to decrease in this case, but that would not necessarily happen.

The strains from the FEA model need to agree with the strains from DIC. It can be assumed that both data sets have a wrong neutral axis, but these neutral axes have to be used as reference in the analysis. Since the left and right data sets are both equally important, it has been chosen to take an average of the neutral axis before the FEMU model starts. The original neutral axes are abandoned, but now it is possible for the FEMU program to converge in a proper way.

3.6. MATERIAL CHARACTERIZATION PERFORMANCE

This section shows the performance of the FEMU program. As the model is programmed to converge the strain results at specific locations, here is where the comparison is made. The accuracy is set to 1%, as in (3.13). This criterion is met after 6 iterations when the linear shear stress approximation is used (eq. (3.8)). The model converges within 4 iteration when using the bi-linear shear stress estimation (eq. (3.9)). An advantage of this method is that the initial material or stress estimates have no influence at the final material parameters. However, the more accurate the analytical estimate is, the fewer iterations are needed to converge to material properties. This way, one may also make statements on the degree of accuracy of the initial estimate.

For this section, a batch of four coupons of IM7/8552 carbon epoxy tested in the 1-3 plane is taken as example of the performance of the FEMU method. This batch was chosen, as the analytical solution gives material parameters that differ from those specified by the manufacturer. The deviation in axial moduli is caused by the finite aspect ratio, which skews the strains near the edges of the speicmen. These four specimens equate to $4x2 = 8$ data sets. The material parameter convergence using eq. (3.9) is shown in table 3.1 and figure 3.12.

The shear nonlinear stress-strain response converges as expected [4, 6]. For this example, the convergence of this response is shown in figure 3.12. The bi-linear geometric stress approximation is already very accurate and the response hardly changes within few iterations. Had a linear geometric shear stress estimate been used, the results would have been very similar to that already found in [4, 6] and figure 3.13. This trend is shown to be much more like the results shown in Iosipescu test specimens. Figure 3.13 (a) shows the comparison between the SBS analytical expression, assuming linear geometric shear stresses, and Iosipescu nonlinear shear parameters, according to test results made by He et al. [6]. Using the batch of IM7/8552 specimens, this figure is recreated in 3.13 (b). The "initial" stress estimate is calculated using equation (3.8). The fourth iteration (and the bi-linear stress approximation), agree with the Iosipescu test specimens. Note that the spread in the non-linear shear response is still very small, even after the iterative program is applied.

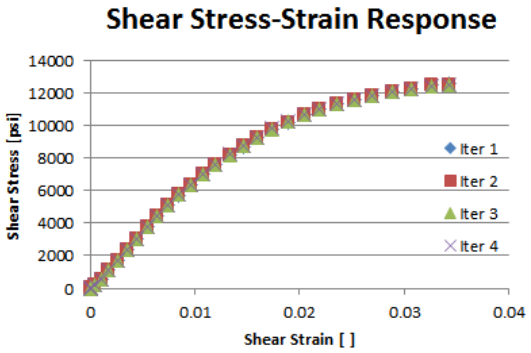


Figure 3.12: Converging Shear Stress-Strain Response in UD IM7/8552 using Bi-linear Shear Stress Equation

Figure 3.14 and table 3.1 show that the material properties found in this iterative model is close to the values as specified by Hexcel [20]. Even though the group in this batch have a relatively small spread, they fall just

Table 3.1: Convergence of the Material Properties of IM7-8552 using FEMU, Bi-Linear Shear Stress Approximation.
* = average between tensile and compressive values

Iteration	E11T	E11C	NU13	G13	GK	Gn
A1: 1	2.64E+07	2.11E+07	0.347	7.74E+05	2.94E+04	0.199
2	2.42E+07	2.10E+07	0.412	7.34E+05	2.71E+04	0.182
3	2.39E+07	2.11E+07	0.421	7.35E+05	2.65E+04	0.177
4	2.37E+07	2.12E+07	0.423	7.35E+05	2.62E+04	0.175
5	2.36E+07	2.13E+07	0.423	7.36E+05	2.61E+04	0.174
A4: 1	2.62E+07	2.18E+07	0.334	7.74E+05	2.80E+04	0.191
2	2.40E+07	2.15E+07	0.408	7.34E+05	2.56E+04	0.173
3	2.36E+07	2.16E+07	0.421	7.35E+05	2.49E+04	0.167
4	2.35E+07	2.17E+07	0.424	7.36E+05	2.47E+04	0.165
A5: 1	2.64E+07	2.26E+07	0.290	7.99E+05	3.00E+04	0.205
2	2.41E+07	2.21E+07	0.375	7.56E+05	2.79E+04	0.190
3	2.37E+07	2.22E+07	0.385	7.58E+05	2.73E+04	0.185
4	2.36E+07	2.23E+07	0.387	7.58E+05	2.71E+04	0.184
A6: 1	2.64E+07	2.09E+07	0.309	7.85E+05	3.22E+04	0.220
2	2.42E+07	2.09E+07	0.415	7.41E+05	3.11E+04	0.212
3	2.38E+07	2.11E+07	0.446	7.41E+05	3.08E+04	0.209
4	2.36E+07	2.12E+07	0.462	7.42E+05	3.07E+04	0.208
AVG Iter 4	2.36E+07	2.16E+07	0.424	7.43E+05	2.71E+04	0.183
Hexcel	2.26E+07	2.07E+07	0.333*	2.26E+07		
COV [%]	1.7	6.4		3.7		

within the error margins. The axial tensile and compressive moduli are slightly higher than the average in Hexcel. It is unsure whether that is due to a fault in the FEMU program or variability in the manufacturers process (slightly higher fiber volume fraction). The linear value of the shear stiffness is higher than that as specified by Hexcel. It is to be expected that the shear stiffness values differ. Instead of one linear value, the linear response is expressed with one linear and two non-linear values. The further the tests reach into the non-linear response, the less accurate a linear shear stiffness estimate becomes. Lastly, the Poisson's ratio in the FEMU program is off. The initial estimate is fairly accurate, but the FEMU increases this parameter. In this case, the analyst should use the initial estimate, rather than the FEMU converged estimate.

Figure 3.15 visualizes how the FEMU model converges upon the DIC strain measurements to find material parameters. In this example, strains at only the right cross-section of a S2/381 glass epoxy specimen are taken for the material iterations. Graph (a) shows the axial strains throughout the thickness. The result matches fairly well at iteration 1 already. The slope of the FEM curve is slightly too steep, which results in a decrease of the axial moduli. The intercept value in FEM is significantly overestimated. The FEMU model corrects to this error by decreasing the tensile/compressive moduli ratio. The latter effect is shown in the graph (b), which is zoomed in from graph (a). The final iterations match the neutral axis much more accurately. Graph (c) shows the transverse stresses. The top and bottom parts of this graph for DIC measurements are not taken into consideration. The FEM model will only show a relatively straight line for the transverse strains, which is not observed in DIC. Rather, the slope in FEM is matched to the slope in DIC for the linear regime in the measurements. Finally, graph (d) shows the shear strains in DIC and in FEM. The solution converges to match the graph much better, but slightly overestimates the peak. This is because the shear response is not optimized to match this single frame, but rather all frames. This frame may be slightly over-estimated, but other frames match better.

Figure 3.16 shows how the strain fields from FEM and DIC match. The DIC frames is on top, followed by the FEM frame. The color scheme is matched exactly.

The last evidence that the material parameters used in the analysis are correct, is by comparing the load-

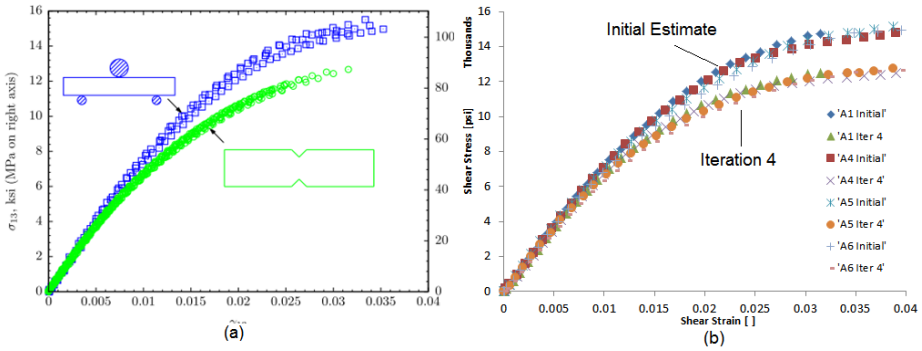


Figure 3.13: Converged Shear Non-Linear Properties Agree with Iosipescu Beam Specimens [6]

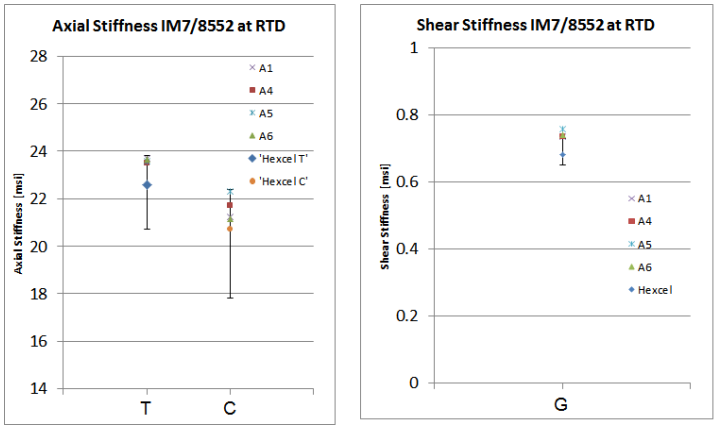


Figure 3.14: Comparison Converged Material Properties from SBS to Manufacturer Hexcel Data

displacement curve from FEM to the one measured. The maximum displacement of the model is underneath the loading nose, but the displacement of the model does not coincide with that from the loading machine. The error is larger than the loading frame compliance and the indentation of the specimen. Deformation measurements of DIC are used to conclude if the model or the test data as written by the testing machine is wrong. For an IM7/8552 CFRP specimen with a square cross-section of $.25x.25[in]$ and $L = 1.725[in]$, the load-displacement curve in FEM and DIC is given by figure 3.17. Using the converged material properties, an excellent fit is found between the simulated and measured structural response.

The method relies on regression analyses to process FEM and DIC data and shifting boundaries on measurement data for the regression analysis has consequences on the material properties found. One may reduce this dependency by setting firm guidelines for setting the regression boundaries or by changing the concept of the FEMU iterations. Least-squares strain data fitting between FEM and DIC (see section 2.4) may be less sensitive for interpretation of these boundaries. It is very much advised to run more test runs on more materials with this program to characterize its performance and reliability. Furthermore, the program has operational drawbacks. The preparation of the input data sheets takes time and the program itself is computationally expensive. Therefore, it is not suitable for rapid material screening purposes, where time is very important as well.

In conclusion, the FEMU model uses an iterative method to substitute the stresses from the closed-form solution with those found in the FEA. The closed-form solution overestimates the slope of the axial stresses and the neutral axis, because of the finite aspect ratio. This results in a decrease of the tensile/compressive axial stiffness moduli and their ratio. The first estimate for the Poisson's ratio and shear stiffness parameters is very good. The FEMU model then corrects the shear non-linear stiffness values to match the DIC measurements even better. If an accuracy of 1% is required, the model needs at most 4 iterations to converge.

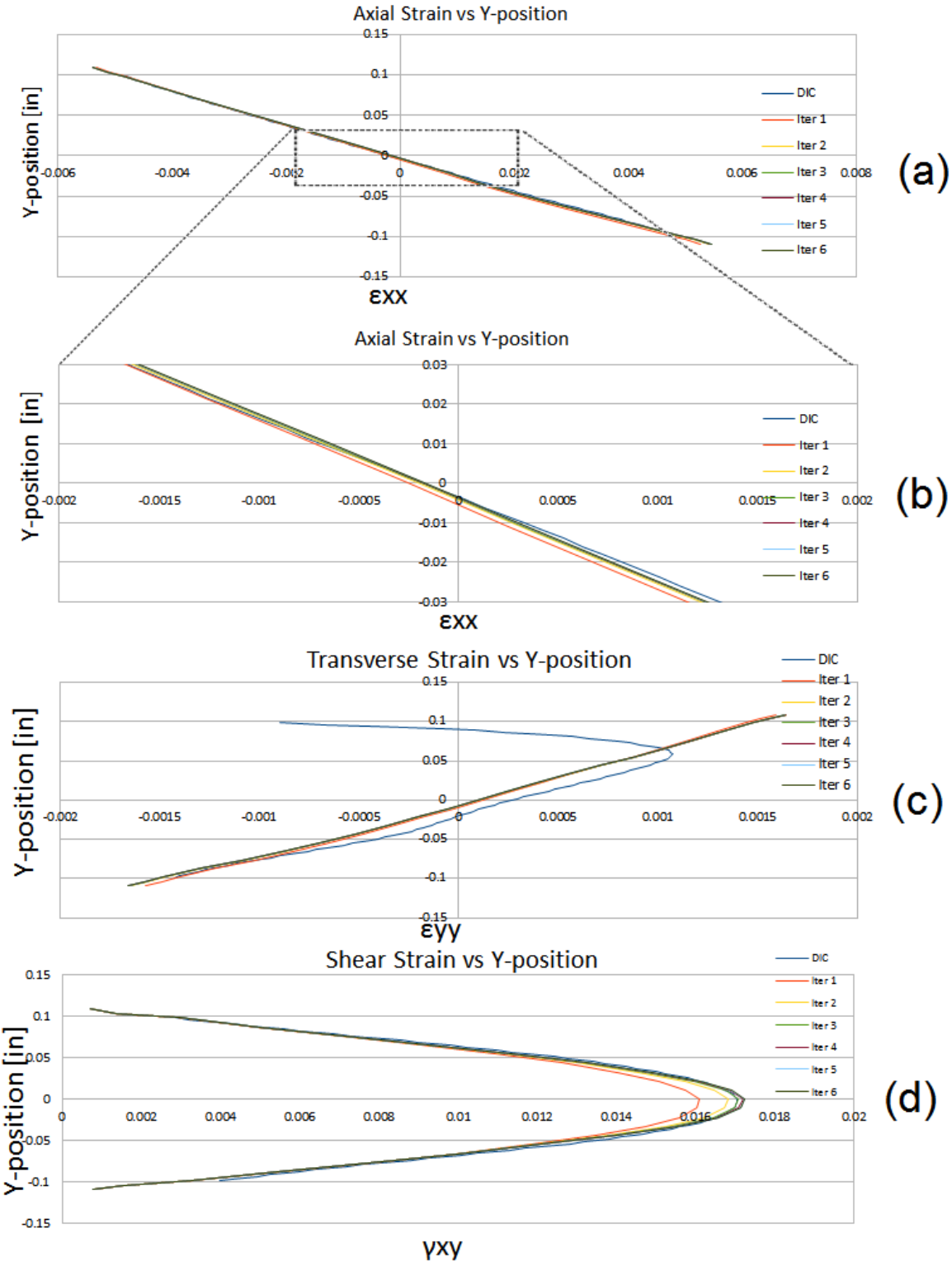


Figure 3.15: Strain Comparison of DIC Measurements and FEM Output at Right Cross-Section in S2/381 UD Composite at 555 lbf

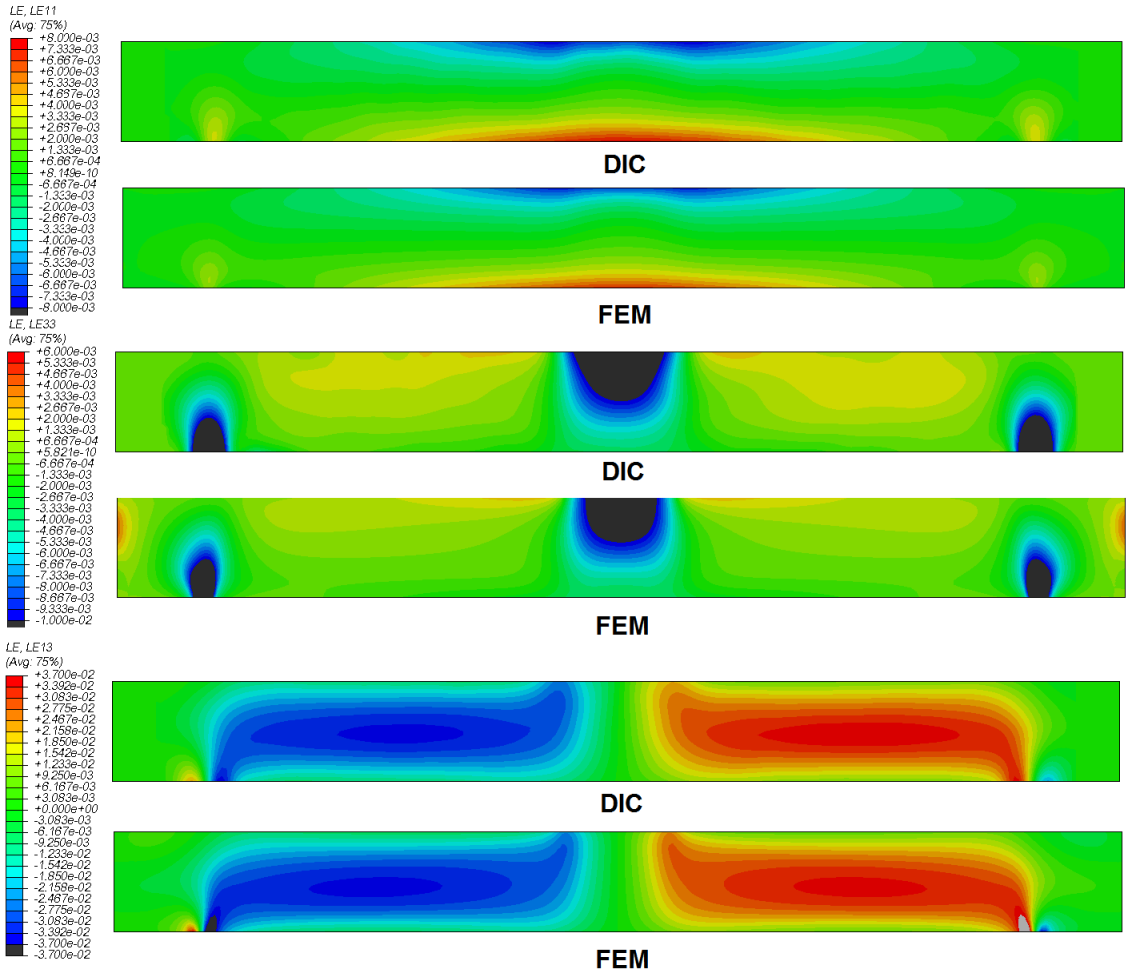


Figure 3.16: Strain Field Comparison of IM7/8552 SBS Specimen under 1100lbs Load

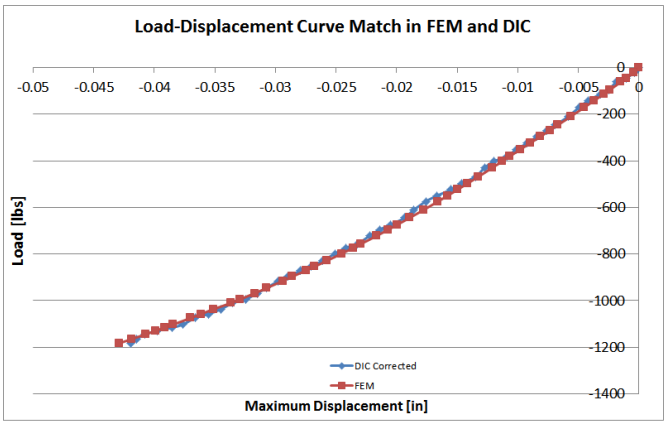


Figure 3.17: The Load-Displacement Curves match between FEM and DIC if Converged Material Properties are used

4

SPATIAL VARIABILITY OF CONSTITUTIVE MODEL PARAMETERS

This chapter shows the tools (section 4.1), the methodology (section 4.2), the results (sections 4.3 and 4.4) and conclusions (section 4.5) of the spatial variability analysis of constitutive model parameters in the SBS model. It also deals with the issue of coupling effects between transverse and shear stresses in the non-linear regime.

4.1. REFINED FEM MODEL AND DIC PLOTTING TOOL

The purpose of the SBS model in this chapter is different than that in chapter 3. The front half of the SBS model is modeled to get an accurate stress and strain field from the FEM model at the front surface. This is used for comparison with the strain fields from DIC and for nodal calculations. It is important to model the contact as accurate as possible, to get reasonably accurate stresses as the field of interest reaches towards these contact areas. The half model will use properties which have been established with the FEMU model. The strain fields from DIC and FEM (figure 3.16) match better than when using standard material parameters.

The lay-out of the model is reasonably unchanged. The mesh is still divided in the same sections, the same symmetry conditions apply. However, the supports are modelled as solids, rather than analytical rigids. As shown in section 3.2, the supports and loading nose have a finite stiffness and there is a small change in the strain fields under the loading nose and supports. The supports are given generic steel properties: E = 30E6; ν = 0.29. The loads and boundary conditions are now applied to the top/bottom of the solids. The load is now a pressure on the loading nose, with magnitude $P_{max}/(2 * AREA)$. Figure 4.1 shows the refined mesh field on the half model, showing only the left half. It shows that the solids have a themselves have a structured and refined mesh towards the contact zone.

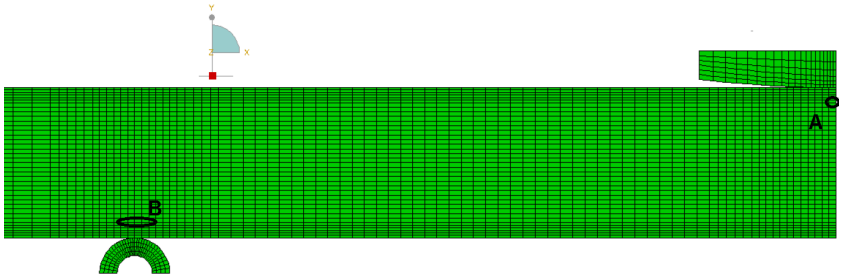


Figure 4.1: Overview of the FEM Model with Refined Mesh (left side only). Areas A and B are used for the Mesh Convergence Analysis

(a) SBS Model Discretizations See Figure 3.7

Edge	# Discr.
L1	24
L2	5
L3	40
L4	5
L5	12
T1	6
T2	26

(b) Stress Components at Selected Nodes for Different Elements in the Width

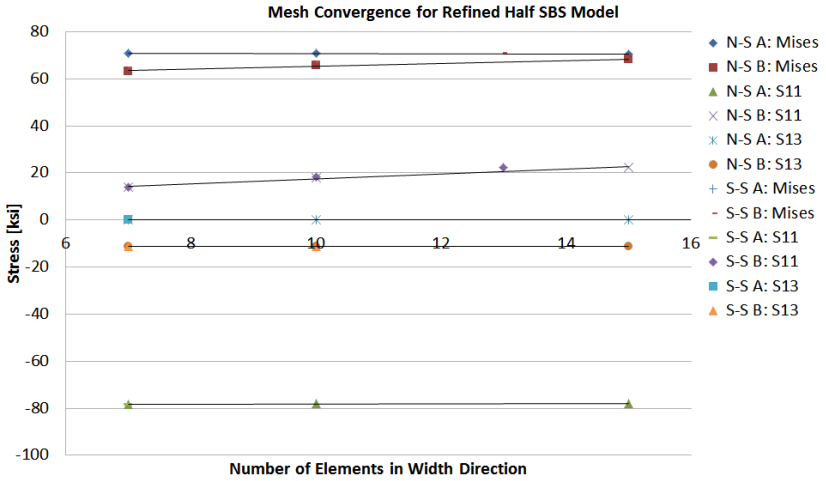


Figure 4.2: Mesh Convergence for Refined SBS Model.

The mesh as described in table 4.2a is finer than that of the FEMU model, in order to create more nodal points and increase the stress field accuracy. The discretizations along T1, L1, L5 and the width are most critical to mesh convergence. In this model, it is most important to converge upon the axial and shear stresses, which are related to the material parameters sought after in the SBS test setup. The stress field does not change significantly when increasing the number of discretizations along T1, L1 and L5, but the number of discretizations in the width direction does affect the surface stresses. This is visualized in figure 4.2b. Underneath the loading nose (A) and the support (B) are plotted: the maximum mises stresses, the maximum axial stress component S11 and shear stress component S13 are plotted. A and B are at distance T1 from the support, because there are no strain measurements at the edges to validate the stresses and strains there. The mesh underneath the impactor is converged. The number of discretizations in width direction does not influence the mentioned stress components. The mesh underneath the support is not converged. A lot of extra discretizations are needed in the width direction, in order to get the axial stress component S11 properly. However, this slows down the model significantly without adding any data points for analysis. As the analysis in this chapter focuses on the shear non-linear response curves, it is decided that the number of discretizations in width direction is left at 7. Due to such uncertainties, no data points very close to the contact area are taken in the analysis.

An important function in this model is the ability to plot the DIC data onto the front surface nodes in the finished ODB file. The goal is to have one step with the strain fields from DIC and one step with all the stresses and strain fields from the FEM analysis. The strains fields have matching loads and the strains fields match well. These frames are matched, to make it possible to generate stress-strain response curves at specific nodes. This is achieved in the following way.

A subdirectory containing the DIC strain data (standard export in .CSV) is specified and a new step is generated in the ODB file. The FEM model has a node set with all the nodes on the front surface, to plot the DIC strain field on. For every frame in DIC it performs the following tasks in order:

1. Read the DIC strain measurement extract (.CSV)
2. Correct the DIC nodal coordinates so that the center of the surface (X,Y) is (0,0)
3. Read the coordinates of the node set at the front surface of the FEM model
4. Use the scipy package (specifically the griddata function) to interpolate the values of the DIC nodal points to the FEM nodal points.

5. Create a frame in the ODB file
6. FieldOutput object files are generated for axial strain measurements and shear strain measurements
7. The FieldOutput objects are filled with the labels from the FEM Node set and the data from the fitted strain measurements

For verification purposes, the corrected DIC nodal coordinates (X,Y,Z) are saved in "DIC_Nodes.f". The strain data corresponding to these coordinates is saved in "DIC_Data.f". The FEM surface nodal coordinates are written in "FEM_Nodes.f". Lastly, the fitted data is written in "Fit_data.f". The ODB now has the full-field stress (from FEA) and strain (from DIC) data fields necessary for the coming analysis.

4.2. SPATIAL VARIABILITY ANALYSIS METHODOLOGY

Using python scripting, a program is made that runs through all the facets of the spatial variability analysis. It starts off similar to the FEMU model, but follows up by a very different analysis.

1. Read the geometry and loading from the input file as shown in Appendix A.
2. Build the SBS model with refined mesh
3. Apply the material parameters from the FEMU model and run the model
4. Plot the DIC frames in the ODB file
5. Start the spatial variability analysis

The spatial variability analysis attempts to map the constitutive model parameters on different locations of the measurement surface. The focus lies on the shear non-linear parameters; the linear stiffness parameters are considered fairly constant over the surface, but they do show significant spread in the nodal calculations. One cause of this is the great uncertainty in the lower load levels, where the noise is statistically much more prevalent than in higher load levels, creating much confusion in these linear part of the analyses. Furthermore, the background information in chapter 2 suggests that transverse stress components alter the shear stress-strain response, primarily in the non-linear regime. If this is true, the shear non-linear parameters are expected to change over the surface. Tensile transverse stresses would result in a lower shear nonlinear stiffness, whereas compressive transverse stresses may increase or decrease the nonlinear stiffness. The SBS model shows regions of compressive transverse stresses, which are interesting to explore.

Since the DIC strains and FEM nodes are overlayed, it is possible to generate stress-strain response curves at specific nodes. The model works as follows. A choice of nodes is made to apply the analysis. From this node list, the xyData List from Field function [46] extracts the raw data (DIC strains and FEM stresses). This raw data is processed to generate the G, K and n parameters. There are a few methods to approach this result:

A carefully selected set of nodes at interesting locations is chosen. For this method, interesting nodes must have very different stress components and lay apart spatially. The stress and strain data is extracted and plotted in Excel. Section 4.3 shows the result of this approach. It will give a very clear view of how the stress-strain curve changes at different locations and which phenomena have to be taken into consideration. It is manageable to show which other stress components may be influencing the stress-strain curves. By making careful observations of the maximum stress components, one may deduce which of these components may or may not affect the shear stress response curve. This method can thus be applied to look for trends.

In the second method, a field of nodes is chosen. This field is processed as a batch; they all follow the same calculations. This is shown in section 4.4. This method is less flexible. As is shown later, the stress-strain curves appear to be translated, due to low load-level inaccuracies. This also reflects into the quantitative solutions: These are to be taken qualitative, not quantitative. Due to this translating effects, it is very hard to set lower and upper limits on the linear part of the shear stress-strain curves.

$$G_{xy} = slope(\tau_{xy}; \gamma_{xy}), \qquad where \qquad \{\gamma_{xy} \| R_L < \gamma_{xy} < R_U\} \tag{4.1}$$

$$G_n = \frac{1}{slope(ln(\gamma_{xy} - \tau_{xy}/G_{xy}); ln(\tau_{xy}))}, \qquad where \qquad \{\gamma_{xy} \| \gamma_{xy} \geq R_{NL}\} \tag{4.2}$$

$$G_K = e^{G_n \cdot intercept(ln(\gamma_{xy} - \tau_{xy}/G_{xy}); ln(\tau_{xy}))}, \qquad where \qquad \{\gamma_{xy} \| \gamma_{xy} \geq R_{NL}\} \tag{4.3}$$

In equations (4.1) - (4.3), the shear linear and non-linear parameters are a function of the stress and strain arrays. R_L, R_U and R_{NL} denote the linear lower and upper range limits and the nonlinear lower limit for the strain values. Appropriate settings of these limits allow for accurate R-O parameters. To remove the dependency on the linear term, the input value for G_{xy} is used in equation (4.2). If the model notices that the shear response curve is translated, it will increase the lower limit for the linear analysis. The upper limit is left unchanged, in order not to overlap with the non-linear response. As a result, the strain regression limits and the linear stiffness value are less than optimal. Furthermore, it is important to remove nodes with low stress and strain levels. In these nodes, no regression analysis is meaningful and therefore, they are shown in the plots with a blank color.

Instead of comparing the stresses and strains across frames, the stresses and strains within a frame may be used to define the axial stiffness parameters. In this method, the list of nodes is used to generate a path along a defined surface. The various stress components are extracted along the path and used to calculate the material parameters (see equation (4.4)). This latter method does not give nice results. It is sensitive to noise; where the stress levels are low, the values for the axial moduli vary easily. This is in the areas around the neutral axis and away from the specimen center. Apart from this, the stress components in 22 and 33 direction underneath the contact surface are uncertain, because the material is only characterized in 2D. The results for this method is shown in section 4.4.

$$E_{11} = \frac{\sigma_{11} - \nu_{12}\sigma_{22} - \nu_{13}\sigma_{22}}{\epsilon_{11}} \tag{4.4}$$

4.3. SPATIALLY VARYING SHEAR NON-LINEAR STRESS-STRAIN CURVES

In this section and section 4.4, a SBS specimen of carbon epoxy IM7/8552 is analyzed. This specimen is loaded in the 1-3 direction, thus the x = 1 and y = 3. Therefore, the axial stiffness moduli E_{11_T} and E_{11_C}, and shear stiffness parameters G_{13}, G_K and G_n are important. In the following analysis, the FEMU model has converged on these parameters:

- E_{11_T}, E_{11_T} = 22.9E6, 20.6E6
- ν_{13} = 0.331
- $G_(13)$, G_K, G_n = 0.72E6, 37E3, 0.246

The selection of nodes is illustrated in figure 4.3. The locations of extracted shear stress-strain curves have been chosen as follows: Locations 1 and 2 have pure shear and thus serve as a reference stress-strain response. Locations 5, 6, 7, 8, 3 and 4 are subject to increasingly large compressive transverse stresses, due to the impactor and supports locations. Table 4.1 shows the maximum stress components at these selected nodes. Nodes 3 and 4 have a compressive stress component equal to the shear stress components. This ratio is lower in nodes 5-8. The main difference between nodes 5-6 and 7-8 is the axial stress component S_{11}, which is much larger for nodes 7-8. It also differs in sign with respect to nodes 3-4.

Extracted stress (FEM) and strain (DIC) curves are shown in figure 4.4. Note that these lines are all positive, as a negative shear-stress response is physically the same as a positive shear-stress response. This raw data quickly shows one of the difficulties with the spatial variability analysis; the FEM model does not agree with the DIC measurements at low loads; the stress-strain curve appears to be translated because the stress does

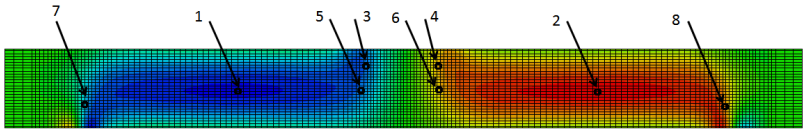


Figure 4.3: Choice of Nodes for Shear Stress-Strain Plots

Table 4.1: Details of Maximum Stress Components on Selected Nodes

Node	S11	S33	S13
1	-3730	100	12877
2	-3730	100	12877
3	-65000	-10000	10053
4	-65000	-13000	11210
5	3800	-6544	11000
6	3800	-6544	11000
7	28000	-9500	12663
8	28000	-9500	12663

not increase at the same time as expected. They do exhibit the same linear slope. Using this linear slope as a reference, the stress-strain curves are translated left or right to match up with the pure shear node curves. Curve 7 is removed, as the left support location did not match well enough with the actual test performed, due to wrong input.

When all the stress-strain curves are lined up, the trends become clearer. The reference "pure shear" nodes 1-2 reach furthest in the non-linear regime, but also have the lowest nonlinear stiffness: the stress-strain curves lie below that from the other 6 selected nodes. Nodes 5-8 show a slightly higher curve. Nodes 3 has the next higher slope and node 4 the highest. Critically speaking, simply translating the curves left gives a less than perfect image of reality. The shear stresses are probably higher and a vertical translation may be more applicable, but it is uncertain to say how much. For this trend analysis, a simple horizontal translation is a conservative approach to this method; a vertical translation would show an even bigger deviation of the stress-strain curves when compared to the "pure shear" nodes 1-2.

The trends as shown in figure 4.4 correlates with the ratio S33/S13. It is important to distinguish between the effects of transverse or axial stresses. Nodes 5-6 and 8 have very different values for the axial stress components, yet the stress-strain response is very similar for these nodes. These axial stresses are positive and a higher curve is observed, but nodes 3-4 are subject to compressive axial stresses and their curve lies even higher. Therefore, there does not seem to a correlation between the ratio of axial S11 and shear stress S13 components and the shear stress-strain curve. This is in line with the results of the literature study, which does not mention any coupling between these stress components.

4.4. STIFFNESS PLOTS WITH NODAL CALCULATIONS

This chapter gives the results of the spatial analysis of constitutive parameters, applying nodal calculations on a surface (large batch) of nodes. This surface consists of thousands of data points, which gives a fine spatial field. The methodology is already explained in section 4.2. Two specimens of IM7/8552 with different aspect ratio's are examined.

The limits for the linear shear calculations are preferably between 0.1% and 0.7%. If the stress/strain curve appears translated, the lower limit is shifted, up to a maximum of 0.4%. The non-linear lower limit is set to 2%. Only nodes that have ten data points over 2% strain are taken into consideration for the non-linear parameter calculations. The results are shown in figures 4.5 and 4.6

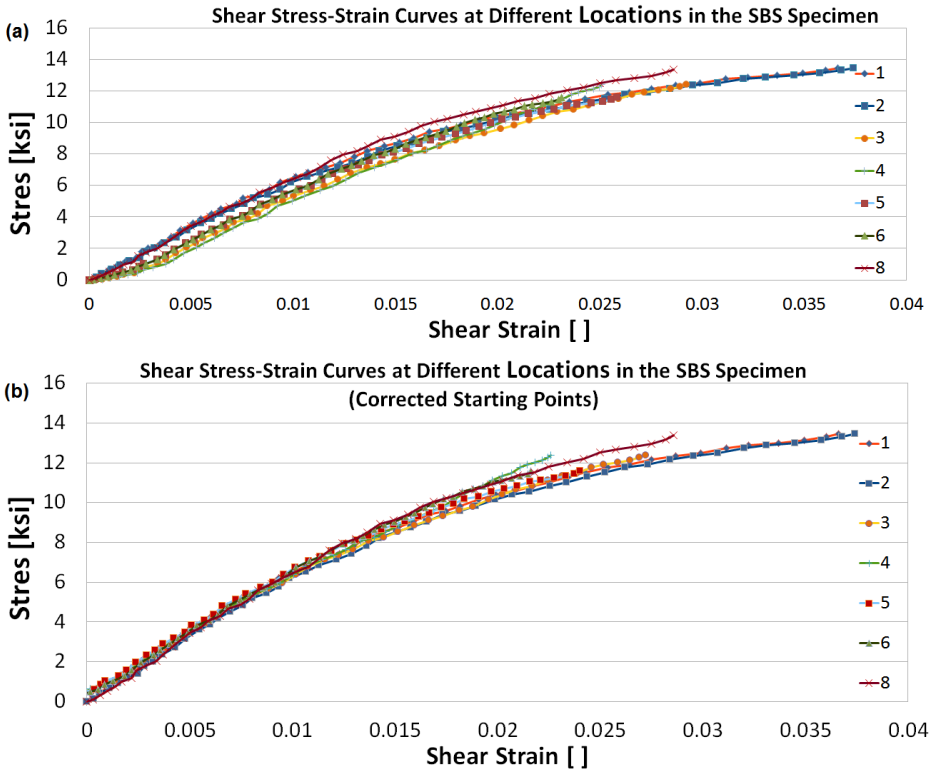


Figure 4.4: Shear Stress-Strain Curves with Coupling Phenomena. (a) shows raw data from FEM and DIC. (b) shows the same data with translated starting points

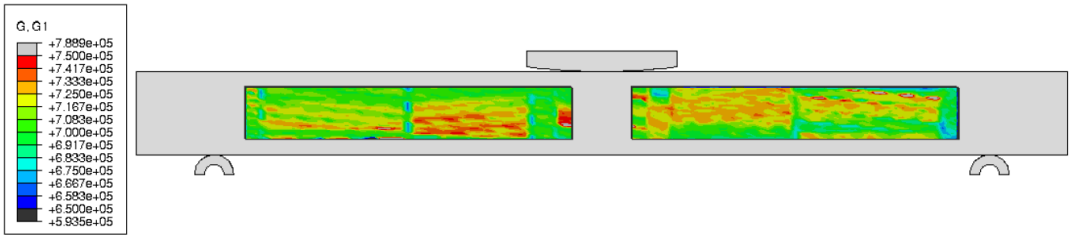


Figure 4.5: Spatial Variability of Linear Shear Stiffness G_{13} of IM7/8552 in SBS Specimen

The method for the shear stiffness parameters can also be applied to axial stiffness. The axial stress-strain response is strictly linear, which simplifies the calculations. There is no shifting of upper or lower limits, so the axial stiffness modulus at any point is simply the slope between axial stresses and strains. This assumption violates equation 4.4, which shows that transverse stresses have to be taken into account. The result clearly shows a different stiffness in the tensile and compressive regions. Only underneath the contact areas, this method is less accurate. There is still a lot of area that gives reasonable results. This is visualized in figure 4.7.

Lastly, it is possible to calculate the axial stiffness moduli using point calculations within a frame. This is explained in section 4.2 and visualized in figure 4.8. The model creates a path from a defined node set (the front surface) and extracts the various stress and strain components along this path. Equation (4.4) is used to calculate the stiffness modulus. This method gives reasonable results when the aspect ratio is very large, but it is inherently less accurate than the method that calculates the axial stiffness across frames. Across frames, many more data points are used to generate the stiffness values. This is visible by a larger spread in the stiffness values compared to figure 4.7.

The methods above have various degrees of succes. First of all, the SBS with the long aspect ratio gives more even stiffness plots than the SBS specimen with shorter aspect ratio. The values found in the spatial field

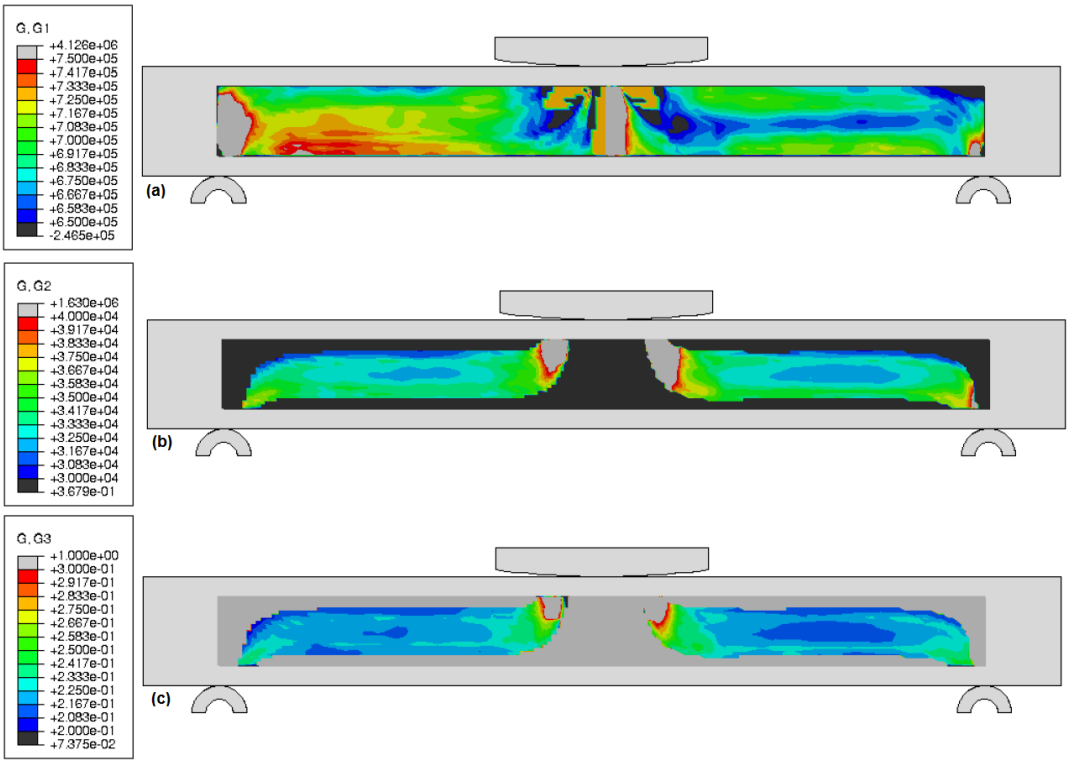


Figure 4.6: Spatial Variability of Shear Stiffness Parameters of IM7/8552 in SBS Specimen.
The three plots show: (a): G_{13}, (b): G_K, (c): G_n

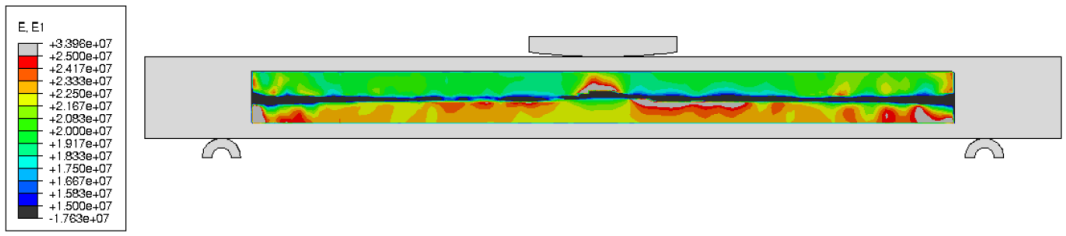


Figure 4.7: Spatial Variability of Axial Stiffness Modulus E_{11} of IM7/8552 in SBS Specimen. Calculations Across Frames

are close to those from the input parameters. However, the specimen fails in a low load in tension and the non-linear analysis was not very useful. The specimen with a low aspect ratio could hold much more load, but was unable to provide smooth linear stiffness plots as shown in this section.

The spatial fields of linear parameters show values comparable to that of the input. Figures 4.9 and 4.10 show a statistical distribution of the calculated axial stiffness parameter in figure 4.7. The axial stiffness values near the neutral axis are cut off, because the strains are too small to make a good estimate of the material property. The histogram is split into two regions, as there is a distinct region for tensile stiffness and compressive stiffness and each has it's own mean and standard deviation. The results are summarized in table 4.2. Input parameters of the FEM model lie well within the error margins of this distribution, but the real compressive axial stiffness might be lower than the input parameter. The spread in the stiffness values is low; the standard deviation is less than 4%.

The results for the non-linear parameters are interesting. The K and n values found in the spatial analysis, at the pure shear nodes, are minimum values. The closer the node is towards the contact areas, the higher the K and n values become. The higher K value delays the onset of non-linearity, whereas the higher n value makes the shear stress-strain curve more curved. Combined, it leads to a delayed shear non-linearity phenomenon. This phenomenon gets stronger towards the contacts, where the transverse stress components are strongest.

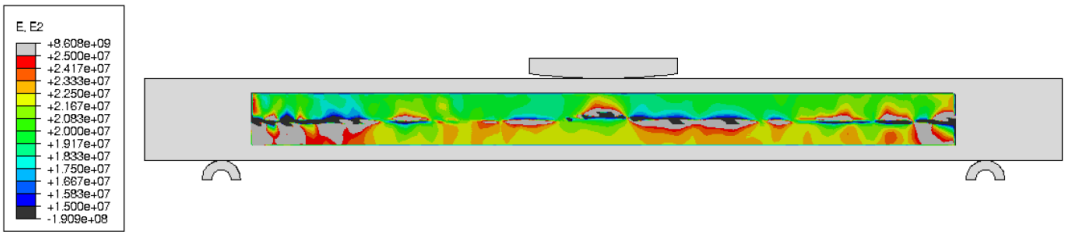


Figure 4.8: Spatial Variability of Axial Stiffness Modulus E_{11} of IM7/8552 in SBS Specimen. Calculations Within Frame

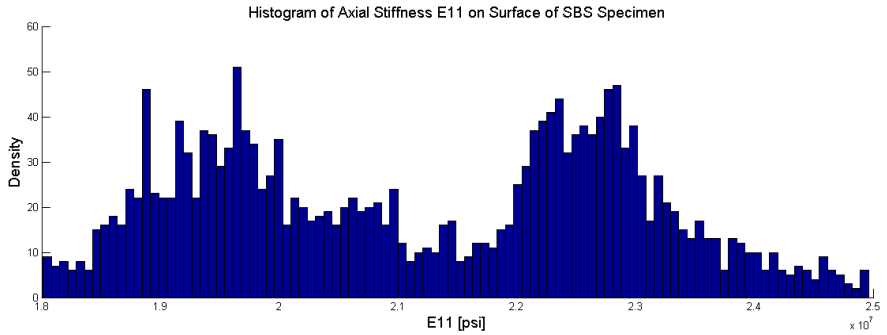


Figure 4.9: Histogram of Axial Stiffness E_{11} in figure 4.7

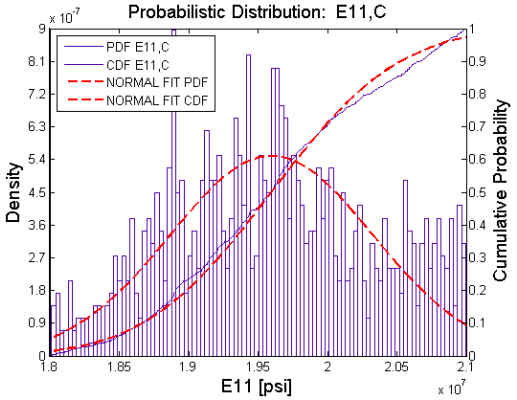
This is a strong indication that there are coupling phenomena in this composite specimen between the shear stress-strain response and transverse stresses.

4.5. CONCLUSIONS ON SPATIAL VARIABILITY ANALYSIS

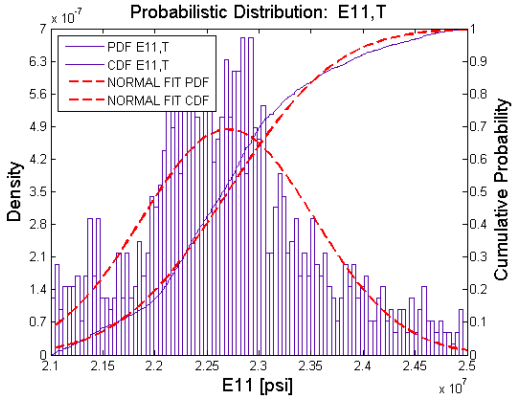
This chapter summarizes the conclusions and recommendations based on the contents of this chapter. Several tools have been developed: The FEM model has a refined mesh and can be used to plot the strain fields from DIC. All analyses extract the FEM stresses and DIC strains to create shear and axial stress-strain curves.

The first analysis is done on carefully selected nodes. The shear stress-strain curve was extracted for these nodes. This method allowed tracking the other stress components. A correlation was found between increasing transverse stresses and increasing shear non-linear stiffness parameters.

The second analysis was a batch analysis to generate spatial fields of stiffness moduli. Because of an inac-



(a) PDF and CDF for Compressive Stiffness



(b) PDF and CDF for Tensile Stiffness

Figure 4.10: PDF and CDF of E_{11}, Excerpts from Histogram in Figure 4.9

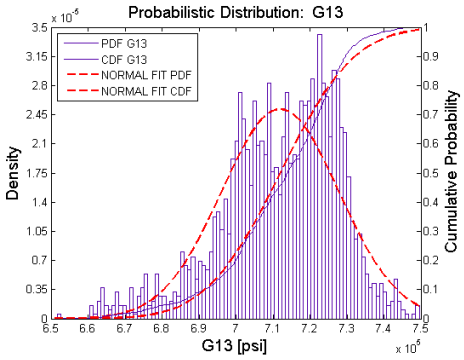


Figure 4.11: PDF and CDF of Shear Stiffness G_{13} in figure 4.5

Table 4.2: Results Statistical Analysis Stiffness Plots Figures 4.5 and 4.7

	Mean	St. Dev. [%]
E_{11}^{C}	1.96E+07	3.70
E_{11}^{T}	2.27E+07	3.60
G_{13}	7.12E+05	2.20

curacy at low loads, the linear strain fields are subject to heavy scatter. This scatter is much more prevalent in the specimen with low aspect ratio than in the high aspect ratio. However, the high aspect specimen does not carry enough load to characterize shear non-linear parameters accurately. This method is also used to characterize axial stiffness. Across frames, the axial stress-strain response curve is generated to extract the stiffness modulus. This method clearly shows how the axial stiffness differs in the tensile from the compressive area.

The third analysis is used to find the axial stiffness parameter using the stress and strain components within a frame. This method deals with the stress components in other directions, but is less accurate than the second analysis, because it makes use of far fewer data points.

The accuracy of this method is excellent in the example provided, but is generally lower and depends heavily on the analysis parameters. Method 3 has the lowest accuracy and should be discarded. The axial stiffness plots show high deviations underneath the contact areas and near the neutral axis. At these locations, the method is not representative. However, the stiffness parameters are scattered around the correct value. Close to the contact areas, the shear stiffness parameters are not accurate. The stress-strain curves appear to be translated, so any conclusions drawn are qualitative, not quantitative. The non-linear shear parameters show increasing values towards the contact areas, where compressive transverse stresses are present. This is evidence to support the hypothesis that IM7/8552 shows coupling phenomena between transverse stress and the shear stress-strain response. Assuming this is true, the stress calculations are wrong, because no coupling terms are taken into account in the UMAT. This matter is discussed in more detail in chapter 5.

In order to increase the accuracy of the method, some recommendations can be made. First of all, the mismatch between the FEM model and DIC at low load levels (which causes the translating stress-strain curves), should be addressed. It might be because the initial load values lag behind the actual load that corresponds to the frames. Also, the contact definition should receive more research; Is the contact actually giving the correct stresses? If the stress-strain curves all start from the same point, a smarter algorithm should be used to define the shear stiffness parameters, without relying on a regression algorithm. A least-squares solution may be more suitable, even though such a method does not always give a unique solution (see appendix D). Lastly, the calculations on axial stiffness properties can be made more accurate by including the effects of other stress components present underneath the contact areas and to exclude data points near the neutral axis.

5

CONSTITUTIVE MODEL VERIFICATIONS

This chapter will discuss the verification of the constitutive model as used in the FEM Updating method as explained in chapter 3. It will discuss several investigations into this model, including a bi-linear approximation for the axial strain measurements (sec 5.1), stress-state dependent Poisson's ratio (sec 5.2) and axial-shear coupling analysis in the non-linear regime. The latter is split in a section describing the methodology and the governing equations (sec 5.5), a section describing the verifications of a new User Material Subroutine (sec 5.4) and the application of the coupling equations into the SBS model (sec 5.5).

5.1. BILINEAR AXIAL STRAIN ASSUMPTION

Currently, the axial moduli E_{xx_T} and E_{xx_C} are estimated using a linear regression analysis of the axial strain measurements along the L/4 cross-section. The method detects a shift in neutral axis and calculates the tensile and compressive moduli accordingly. In closer inspection, there is a clear change in slope of the axial strain near the neutral axis, see figure 5.1. This is confirmed by FEM.

It is unclear how accurate the measurement of the shift of the neutral axis is. The stiffness calculations are very sensitive to this single value. Indeed, the neutral axis is often mismeasured and mismatched left and right, requiring a manual rotation of the measurements to get better results. If this new method could decrease the sensitivity to the single value, the accuracy and reliability of the method would likely increase. Note how figure 5.1 has a high intercept value. The analyst needs to decide whether and how much to rotate the DIC measurements to gain good answers.

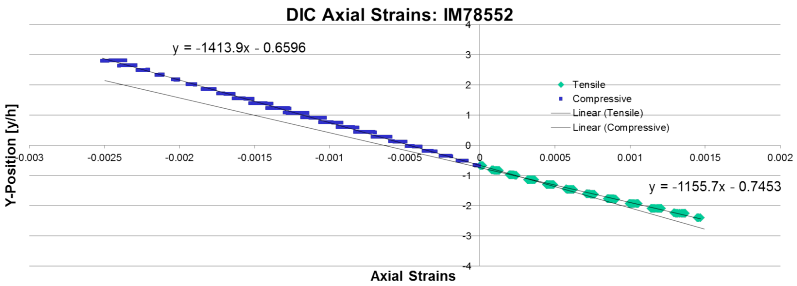


Figure 5.1: Axial Strains at L/4 Cross-Section with Different Trend Lines in Compression and Tension in CFRP

$$\sigma_{xx} = \begin{cases} E_{xx_T}\epsilon_{xx}, & \text{if } \epsilon_{xx} \geq 0 \\ E_{xx_C}\epsilon_{xx}, & \text{if } \epsilon_{xx} < 0 \end{cases} \tag{5.1}$$

Equation (5.1) shows that the stress is dependent upon the stiffness and axial strains. Wen-juan and Zhi-ming [47] give a good analytical solution for the effect of the axial moduli on the neutral axis and vice versa. Figure 5.2 shows a general bending problem. Here, Vm is the height of the neutral axis with respect to the tensile edge and ρ is the bending radius. The strains are assumed to be of the form: $\epsilon_x = y/\rho$. Equations (5.2) and (5.3) show the equilibrium equations for bending moment and axial load. The former is equal to 0 in a pure bending problem. Solving equation (5.2) gives the formula for the neutral axis (5.4). Solving (5.3) for $1/\rho$ and combining with equations (5.4) and (5.1) gives equations (5.5) and (5.6), which note the positive and negative stresses. For example, if $E_C = 0.9E_T$, the neutral axis would shift $0.013h$. The equations are equivalent to those section 3.1. Combining (5.1), (5.5) and (5.6) returns the linear strain approximation.

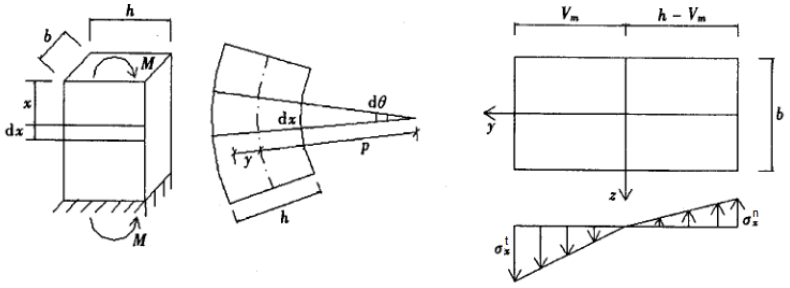


Figure 5.2: Overview, Deformed and Cross-Section View of a Bending Problem

$$N = \int_{V_m-h}^{0} E_T \frac{y}{\rho} b\delta y + \int_{0}^{V_m} E_C \frac{y}{\rho} b\delta y = 0 \tag{5.2}$$

$$M = \int_{V_m-h}^{0} E_T \frac{y}{\rho} by\delta y + \int_{0}^{V_m} E_C \frac{y}{\rho} by\delta y = M \tag{5.3}$$

$$V_m = \frac{h\sqrt{E_C}}{\sqrt{E_C}+\sqrt{E_T}} \tag{5.4}$$

$$\sigma_T = \frac{3M}{bh^3} \frac{(\sqrt{E_C}+\sqrt{E_T})^2}{E_C} y \tag{5.5}$$

$$\sigma_C = \frac{3M}{bh^3} \frac{(\sqrt{E_C}+\sqrt{E_T})^2}{E_T} y \tag{5.6}$$

The calculations are based on an isotropic material with thin and planar cross-sections. This is unfortunately not true in the SBS situation, where the stresses at the edges are skewed. For this method, the equations above are used to attempt converging on a bi-linear strain assumption. Two slopes κ are quantified for the tensile and compressive region (see figure 5.1). Combining equations (5.5) and (5.6) with (5.1) gives the initial stress estimate. As stiffness $E = \frac{\sigma}{\kappa}$, the FEMU model calculates a tensile and compressive stiffness modulus separately. It converges by replacing the estimates in (5.5) and (5.6) with stresses extracted from FEM. The results from the FEMU model above were disappointing. The model converged to a tensile/ compressive stiffness ratio of 1:1, which is not correct for the CFRP material IM7/8552.

To gain more understanding, the effect of the aspect ratio of the test specimen in combination with the tensile/compressive ratio (T/C Ratio) is investigated. In Abaqus, the quarter model is run using different aspect and T/C ratios. The width w and thickness h are 0.25in, making the inertia 3.25521E-4 [in^4]. Generic material properties for IM7/8552 are used, except the axial stiffness is varied. The specimen is loaded until the bending moment at the cross-section L/4 is 150 [lbs · in]. Table 5.1 shows the input and expected parameters for this analysis. It shows the tensile and compressive stiffness moduli used for the analysis, resulting in 3 T/C ratios: 1, 1.125 and 1.25. It also shows the expected neutral axis and slope as expected under pure bending (equation (5.4) and $\frac{M}{E_{avg}I}$)

Table 5.1: Input and Expected Parameters for the T/C Ratio Analysis

T/C Ratio	E_T	E_C	$b_{Expected}$	$\kappa_{Expected}$
1	2.25E+07	2.25E+07	0.00E+00	48.82813
1.125	2.39E+07	2.12E+07	-3.68E-03	48.82813
1.25	2.50E+07	2.00E+07	-6.97E-03	48.82813

The results are summarized in table 5.2 and figure 5.12. One can observe that the neutral axis and the tip of the shear strain curve shift when the T/C ratio is increased. For a long aspect ratio (L = 2.4 [in]), the simulated strain curves approach the closed-form solutions as defined in section 3.1. The equations of a beam under pure bending also become more valid. As the aspect ratio is decreased, the neutral axis is over-estimated. Here, the planar sections are warped due to the effect of the stress concentrations under the loading nose and the supports. Significant transverse stresses are induced that shift the neutral axis. One may also note that the maximum shear strains increase by increasing the aspect ratio. This was noted earlier by Dr. Carpentier [5], who noted that the shear stress estimation becomes more accurate for longer aspect ratios.

Table 5.2: Results T/C and Aspect Ratio Effect Analysis

L [in]	1.2			1.8			2.4		
T/C	1	1.125	1.25	1	1.125	1.25	1	1.125	1.25
Lin. κ	-47.7	-47.7	-47.3	-49.0	-49.0	-48.6	-49.4	-49.4	-49.0
Intercept	-4.1E-3	-7.6E-3	-1.1E-2	-5.8E-4	-4.2E-3	-7.4E-3	2.8E-5	-3.6E-3	-6.9E-3
κ_C	-41.6	-42.0	-42.2	-45.8	-45.9	-45.7	-46.9	-46.9	-46.6
κ_T	-47.3	-46.8	-46.1	-50.0	-49.8	-49.3	-51.0	-50.9	-50.4
ΔSlope	13.7%	11.4%	9.4%	9.2%	8.5%	7.9%	8.8%	8.5%	8.2%

In this chapter, it was noted that the axial strains appear to be bi-linear, changing slope at the neutral axis. It is, however, not possible to determine the tensile and compressive stiffness of the material using this phenomenon. As table 5.2 shows, this change in slopes is dependent upon the aspect ratio and for high aspect ratios, the slopes appear to change little when varying the T/C ratio. In conclusion, the analyst is still advised to use the linear strain estimate for determining these parameters.

5.2. STRESS-STATE DEPENDENT POISSON'S RATIO

While attempting to match the strains measurements with the calculated strains in FEA, the method falls short when it comes to the transverse strains. The DIC measurements often show a curved line of the transverse strains at across the thickness at L/4. The FEM Analysis predicts a fairly straight line. A comparison is shown in figure 5.3. The transverse strains are more bi-linear/curved and are translated. Furthermore, there seems to be an anomaly at the compressive edge that cannot be reproduced in the simulation. This section will therefore explore if the Poisson's ratio might be stress-state dependent.

The transverse strains are not supposed to give a linear curve. Using equations (5.7) and (5.1), it is expected that the transverse strains change slope at the neutral axis, if the tensile axial modulus is higher than the compressive axial modulus. This is visible in the FEM strains as well. The second contribution to the transverse strains comes from the transverse stresses. They are conveniently assumed to be 0, as they are usually negligible. As the aspect ratio becomes shorter, the transverse stresses become more significant and they influence the transverse strain plot (see figures 5.3 and 5.12). Even though the phenomena are the same, the strains do not match well.

$$\epsilon_{yy} = \begin{bmatrix} \frac{-\nu_{xy}}{E_{xx}} & \frac{1}{E_{yy}} \end{bmatrix} \begin{bmatrix} \sigma_{xx} \\ \sigma_{yy} \end{bmatrix} = \frac{-\nu_{xy}}{E_{xx}} \cdot \sigma_{xx} + \frac{1}{E_{yy}} \cdot \sigma_{yy} \tag{5.7}$$

4-point bending test data will be used to investigate whether the Poisson's ratio is stress-state dependent. In

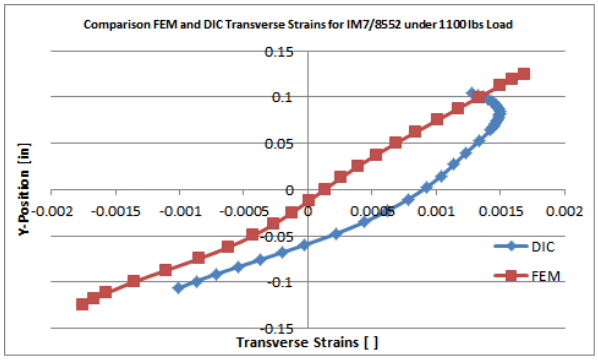


Figure 5.3: Comparison FEM and DIC Transverse Strains for IM7/8552 under 1100 lbs Load

other words, does the Poisson's ratio change depending on the level and sign of stress. The 4 Point Bending test creates a section of pure bending between the two loading noses. Therefore, it is more plausible to assume pure bending in these sections. Figure 5.4 shows a plot of axial stresses vs transverse stresses, which is representative for the Poisson's ratio. This figure is representative for the tested IM7/8552 carbon epoxy and S2/381 glass epoxy 4 Point Bending specimens. The curve appears to translate. No physical reason is found for this translation, but it is also observed in the SBS specimens. In these tests, the Poisson's ratio appears to be constant at first glance, but actually changes it's slope slightly at the neutral axis. This is shown in figure 5.5.

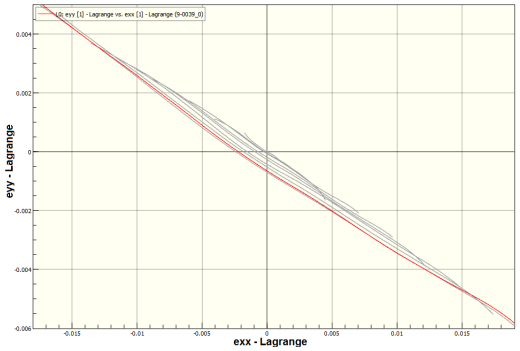


Figure 5.4: Line Slices of Axial Strains vs Transverse Strains in S2/381 4-Point Bending Specimen

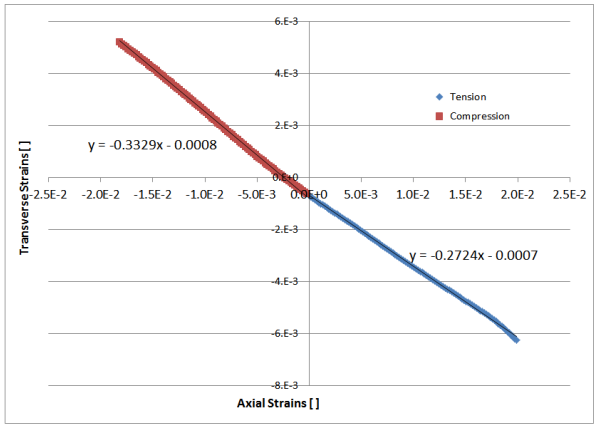


Figure 5.5: The Poisson's Ratio changes at the Neutral Axis in S2/381 4-Point Bending Specimen

Many specimens in the 4 Point Bending tests show damage occurring at the compressive edge. This is often visible as a delamination and results in a transverse strain concentration. This is shown in figure 5.6. One theory is that this damage is occurring at the SBS specimens as well, but the delamination does not visibly

open.

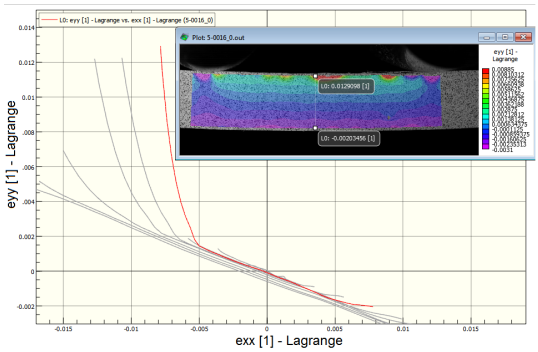


Figure 5.6: Delaminations at Compressive Edge cause Strain Anomalies

IM7/8552 itself has already been proven to have a stress-state dependent Poisson's ratio [20]. In this report, the Poisson's ratio ν_{12}^{T} is 0.316 and ν_{12}^{C} is 0.356. Using a linear approximation, a Poisson's ratio of 0.33 would be expected. The slope of the transverse strains in figure 5.3 appears to be the average of the two different slopes found in DIC.

This chapter showed how and why the measured transverse strains do not match the FEM strains. The Poisson's ratio is shown to be stress-state dependent, but one has to taken into account: the unseen damage at the compressive edge, the slope is expected to change when the axial stiffness modulus is stiffer in tension than in compression and transverse stresses become significant at low SBS aspect ratios. In conclusion: It is possible to define two separate stress-state dependent Poisson's ratios, but the analysis has to compensate for the effects mentioned above.

5.3. UMAT ADAPTION FOR COUPLED SHEAR - TRANSVERSE STRESSES

Chapter 4 shows that there are coupling effects present between transverse compressive stresses and the shear stress-strain curve. The spatial variability analysis did not show how they relate to each other. The following sections investigate one possible form of coupling, where there is a coupling term in the compliance matrix of the material model. The hypothesis is as follows:

"The coupling between transverse compressive stresses and shear strains can be simulated by adding coupling terms in the compliance matrix of the material model in FEA"

For this method, the coupling terms are implemented in the User Material Subroutine in Abaqus, the UMAT. The base for this UMAT is already explained in section 3.3. It is adapted to simulate the aforementioned coupling. This research question is answered using three steps:

1. The User Material Subroutine is adapted to add coupling terms in the compliance matrix. Appendix E shows the calculations related to implementing this coupling term. The coupling term is added as a Poisson's ratio (equation (5.8), where K is a an input parameter of the UMAT). In this Appendix, only the calculations to implement the coupling at location 35 are shown (coupling axial stresses S33 and shear S13). Because the IM7/8552 specimens used as reference are tested in the 13-plane, it is only possible to investigate the effects of strain components in 11, 33 and 13. Furthermore, equation (E.9) would quickly grow very large and complex if more coupling terms are added. One may also investigate a coupling term in the 15 location (between axial stresses S11 and shear strains LE13), but it has been established in section 4.3, that it is highly unlikely that this coupling exists. The coupling term ν_{35} is non-linear and assumed to have a quadratic expression (see equation (5.8)). This prevents any coupling effects in the linear regime.

2. The new UMAT is verified to be working correctly. A 1-element model is set up and subjected to a combination of shear and transverse compression. It shows that the shear stress-strain curves changes when transverse stresses or strains are applied.

3. The new UMAT is applied to the SBS model. This validates or invalidates whether the coupling phenomena are well simulated with this approach. The only way to validate the model is by comparing the strain fields. If a coupling term can find a better match between the DIC and FEM strain outputs, it is plausible that this method works. If the mismatch between the strain fields increases, this method would not be applicable.

$$\nu_{35} = K \cdot \gamma_{13}^2 \tag{5.8}$$

On a critical note on this method, there is little physical background to support this method. The cause of this coupling phenomena is found in micro-mechanics: the formation of tiny cracks in the matrix. This is not simulated in this method and worse, the Poisson's ratio will easily exceed 0.5 at high shear strain values.

5.4. VERIFICATION OF UMAT WITH COUPLING TERMS

This section verifies that the UMAT as described in section 5.3 and appendix E works properly. A single element model is set up and loaded in the 1-3 plane. An overview of the model is given in figure 5.7. The model is encastred on one side and at the other side a shearing and a compressive displacement is applied.

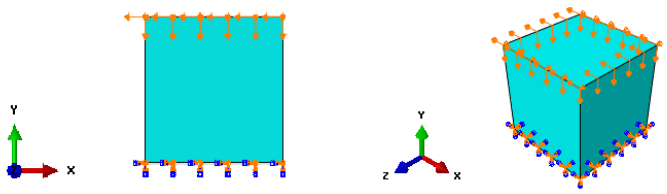


Figure 5.7: Single Element Model Used to Verify the UMAT with Coupling Terms

The single element model illustrates the coupling phenomena in this model. Because the coupling term is a function of the shear strains, a simple compressive strain will not induce any shear strains. Then, the ν_{35} is zero and the model behaves exactly like the reference UMAT. However, if a large shear strain is applied, other effects become visible: The transverse strains in 3-direction increase significantly and the strains in the 1- and 2- direction increase slightly. This effect is quadratic; negligible at low shear strain values and more significant at high strain levels. Combined shear and compressive loading clearly shows the effect of the coupling. Figure 5.8 shows the shear stress-strain curve for two different loading cases and for various values of K.

In figure 5.8, the shear stress-strain response is altered due to the presence of compressive transverse stresses, as expected. The most important parameters are G_{13} (0.75E6), G_K (25,000), G_n (0.2), K and E_{33} (2.0E6). The basic Ramberg-Osgood equation is given as a reference, which matches well with the new UMAT if K=0. The numeric values as plotted from UMAT correspond with the analytical solution, and therefore it is verified that the UMAT reacts as intended.

The model already shows fundamental flaws with previously observed results. High values of K are representative for strong coupling effects. As is shown when K = -2000, the Poisson's ratio is reaches a value so high, that the solution is unstable. Apart from this effect, the sign of the shear strains determines in which direction the transverse stresses move the shear response curve. The line for "K = 1000, S13 < 0" is a perfect match with "K = -1000, S13 > 0" and vice versa. This is unfortunately not in agreement with the results found in section 4.3, where compressive stresses move the shear stress-strain curve up, independent of the shear strain sign.

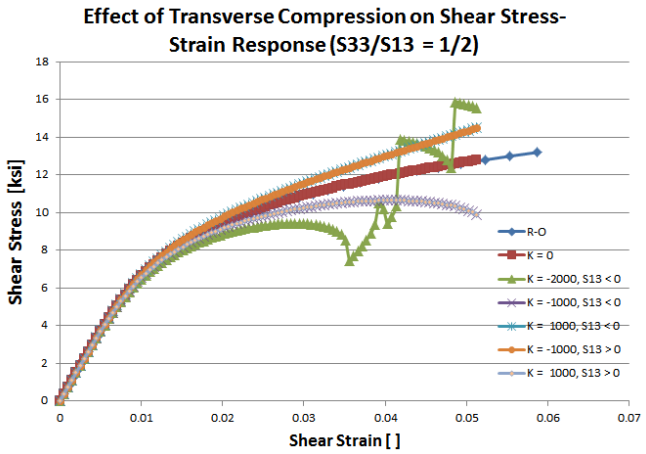


Figure 5.8: Effect of Simulated Coupling Between Transverse Compressive Stress S33 on the Shear Stress-Strain Curve. The S33/S13 Stress Ratio is 1/2

5.5. APPLICATION OF UMAT WITH COUPLING TERMS IN SBS SPECIMENS

After the UMAT with non-linear coupling between transverse stresses and shear strains is verified to work as expected, it is applied to the SBS specimen. By now, it is deemed improbable that the coupling equations as shown in Appendix E are valid, because of the sensitivity to the shear strain convention and the lack of a physical basis. The only way to surely say a method is invalid, is the show that the output strain field from FEM does not create a better match with the measured strain field in DIC. Therefore, the new UMAT is applied to the SBS and any changes are noted. The purpose of this analysis is to find trends and make a qualitative judgment on the validity of the method.

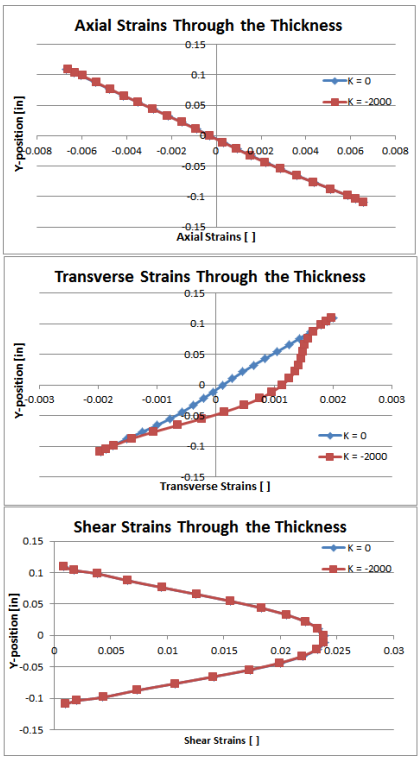


Figure 5.9: Simulated Strain Components at the Right Cross-Section in an SBS specimen in FEM. Blue = Uncoupled. Red = Coupled

Figure 5.9 shows the strain components through the thickness at the right cross-section of a SBS specimen.

The transverse stresses are very low, thus the influence of this component on the axial and shear strains is very small and hard to differentiate. The effect of the shear stresses on the transverse strains is very significant. The transverse strain line becomes much more curved. Even though curves like this are sometimes found in the SBS strain measurements, they are also found this way in the 4-point bending tests, where the shear stresses are very small (see section 5.2). Furthermore, the curvature is mirrored on the left side; the transverse line curves upward, because the shear stresses are negative. This mismatch is not observed in DIC.

Figure 5.10 shows the FEM output transverse strain field (LE33) with coupling phenomena. Because the shear stresses are mostly positive right and negative left, there is a strong asymmetry in the effect on the transverse strain field. This causes the strain field to look twisted. In the DIC measurements (figure 5.11), this phenomenon is not observed. The strain field does not appear to twist as the specimen goes from a low load to a high load.

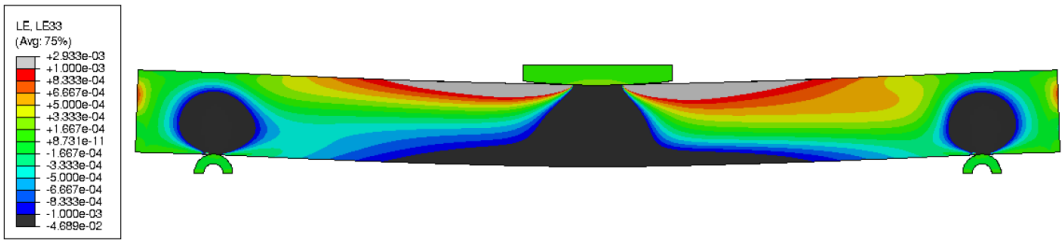


Figure 5.10: Strain Field in FEM with Coupling Term in UMAT

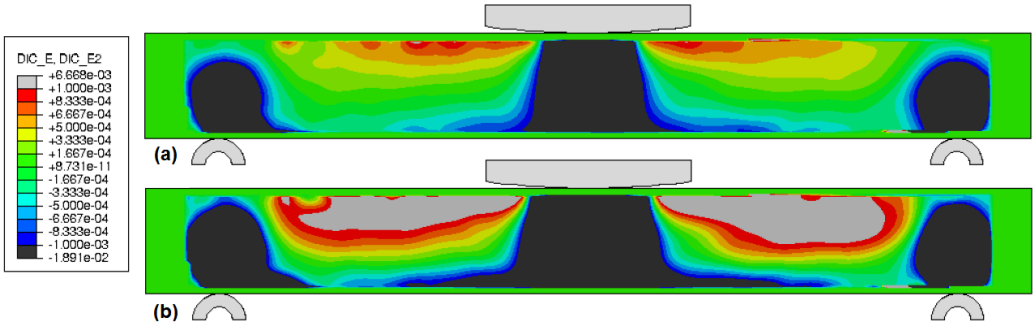


Figure 5.11: Strain Fields in DIC. (a) Low Load (b) High Load

In conclusion, the coupling between transverse stresses and the shear stress-strain response cannot be simulated with the coupling term as described in section 5.3. Whereas it does allow the transverse stresses to influence the shear strains, the dependency on the sign of the shear strains invalidates the argument. Also, the inverse relationship (the effect of shear strains on transverse strains), is unconfirmed by examining the SBS strain field. The "twisting effect" on the transverse strain field is not observed in the DIC measurements. Lastly, the appearance of transverse strains due to shear stresses is not supported by literature. Test data from Vogler [12] does not show that shear stresses actually induce transverse strains. It does, however, influence the transverse stress-strain response. This effect is not even taken into consideration in the current material model.

One may wonder whether the coupling term in the compliance matrix may be adapted, so that it always points in one direction. This solution would not fix the issues that this method is facing; the lack of a physical basis, the potentially very large Poisson's ratio and that shear stresses induce transverse strains. The coupling term would also change over the surface. A better idea may be to expand the Ramberg-Osgood equation for the shear stress-strain response by adding extra coupling terms to this equation based on S22 and S33. It is plausible that the SBS specimen can be used to quantify the coupling phenomena between shear and transverse stresses, but an appropriate law to simulate this response has to be established first.

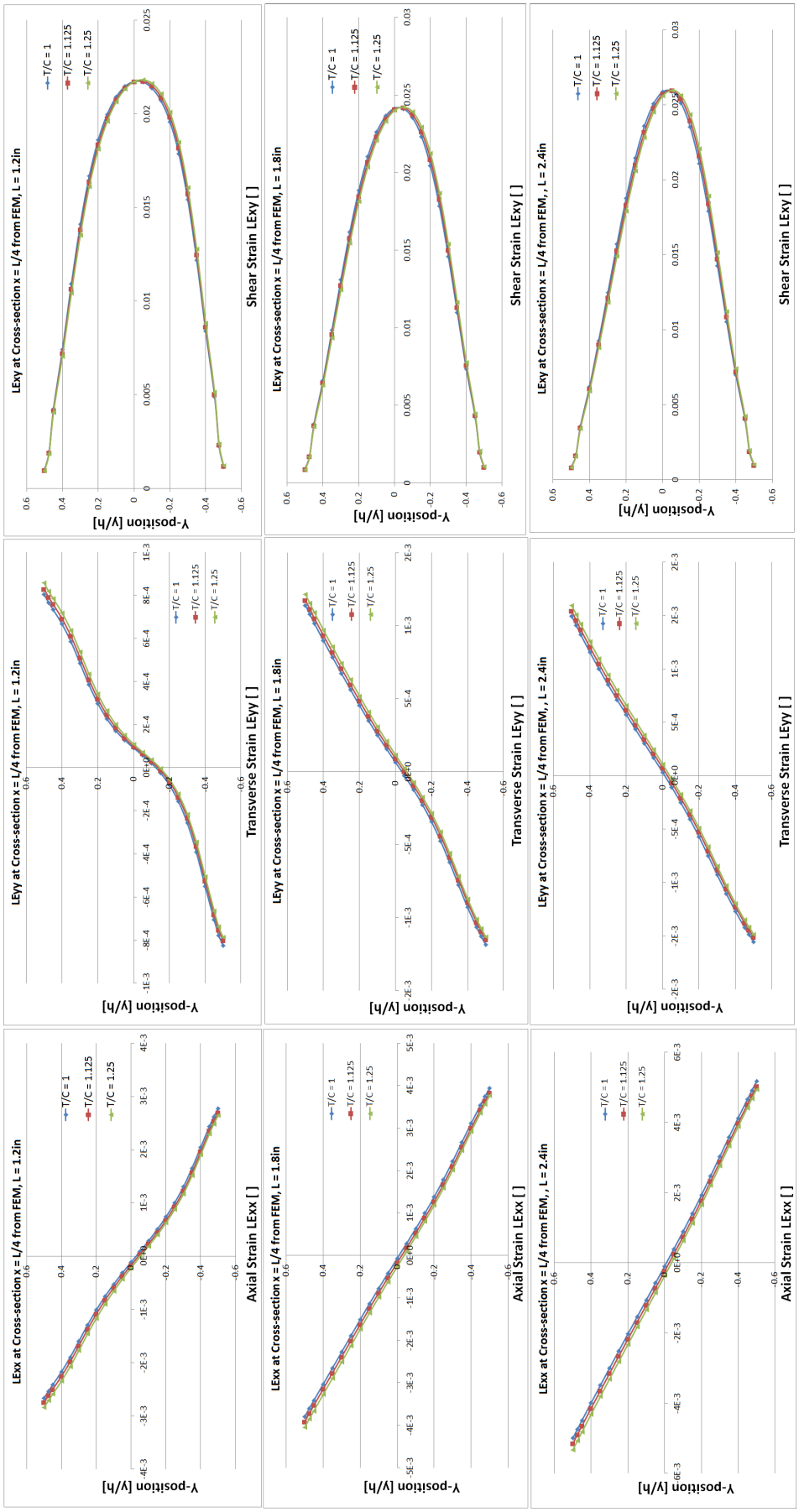


Figure 5.12: AR and T/C Ratio Analysis: Strains at $L_R/2$ from FEM

6

CONCLUSIONS AND RECOMMENDATIONS

6.1. CONCLUSIONS

The first research question asks whether all the material constitutive properties of uni-directional Fiber Reinforced Plastics can be more accurately characterized using an iterative method. Because the aspect ratio is finite, the actual shear stresses, the axial stiffness properties and the neutral axis are overestimated. A FEMU program was developed as illustrated in chapter 3 as a post-processing tool to enhance the accuracy of the identified parameters. As mentioned in section 5.1, the program should be applied when the aspect ratio becomes too small (lower than seven). Unfortunately, the program has some operational problems. The preparation of the input data sheets takes time and the program itself is computationally expensive. Therefore, it is not suitable for rapid material screening purposes, where time is very important as well. In conclusion, the FEMU program is most significant when accurate material characterization is desired for SBS specimens with low aspect ratios.

The second research question asks if the variation of material properties over the measured surface of an SBS specimen can be specified. Chapter 4 shows how strain measurements from DIC are combined with stresses from FEM to provide nodal stress-strain curves. Thousands of data points on a surface indeed provide a surface of changing material properties.

The third and last research question asks whether the constitutive model currently used at the AMSL is accurate enough to simulate the strains from DIC accurately. Section 5.2 shows that the Poisson's is stress-state dependent, which is possible to characterize in the SBS specimen. Furthermore, the research shows that there are coupling phenomena between transverse stresses and shear strains. A correlation was found between transverse compressive stresses and shear non-linear stiffness parameters (see chapter 4). The original hypothesis goes as follows:

"The material model as used by the AMSL lab at UTA is correct and spatial variability of shear stiffness properties will not exceed noise levels."

The first part of the hypothesis ("the material model is correct") is disproved in research question 3. The second part ("shear stiffness properties will not exceed noise levels") is partly disproved in chapter 4. The noise contribution in DIC is typically in between 3-10% (see appendix B). Variability plots of linear shear and axial stiffness show a relatively small spread of the material parameters, potentially less than 4%. On the other hand, the non-linear shear parameters change significantly over the surface. Near the contact areas, the increase in these stiffness parameters cannot be explained by noise alone. This evidence supports the notion that IM7/8552 shows coupling phenomena between transverse stress and the shear stress-strain response.

As the SBS specimen shows coupling phenomena between transverse stresses and shear strains, this effect has to be incorporated in the UMAT. The SBS test setup can be used to characterize coupling phenomena in the non-linear regime, because the surface nodes comprise many different combinations of stress components. Because the ratio compressive stresses - shear stresses varies per node, a lot of different loading scenario's are available in one test piece. These scenarios and their shear response curves may be used as pieces of a puzzle to characterize the coupling phenomena.

This thesis tested and disproved that the coupling between transverse compressive stresses and shear strains can be simulated by adding coupling terms in the compliance matrix of the material model in FEA. Sections 5.3 to 5.5 show that the coupling is dependent on the sign of the shear strains, which invalidates the argument. Also, the inverse relationship (the effect of shear stresses on transverse strains), is unconfirmed by examining the SBS strain field, because of a "twisting effect" on the transverse strain field.

To summarize, this thesis shows an iterative method to converge on and characterize all surface constitutive properties in a Short Beam Shear test method. Combining the stresses from Finite Element Analysis (using these converged properties) with strain measurements from Digital Image Correlation, stress-strain response curves are generated based on nodal calculations. These stress-strain curves are translated into material parameters and shown to vary across a surface. This analysis shows that the material model can be improved by adding coupling effects between transverse stresses and shear strains.

6.2. RECOMMENDATIONS

Based on the conclusions for research question 3, the material model should be expanded to distinguish between tensile and compressive Poisson's ratios and include coupling of transverse stresses and shear strains. A new law has to be established for the coupling phenomena, possibly based on expanding the Ramberg-Osgood equations. Incorporating this law, a new version of material iterations should be applied to find the actual parameters of this coupling. The SBS method can also be applied to measure the transverse stress-strain relationship. The transverse stresses and strains are high near the contact areas. In order to do this accurately, the contact stresses need to be validated and one has to compensate for stress components in the axial and width direction. This also means that the stiffness components in the other directions have to be accurate, thus requiring that the SBS specimen is tested in different planes first. Next, the FEMU model has been shown to converge on accurate material properties in a few specific cases. It can still be improved by adding the following:

- Making it easier to find the rotation angle for SBS specimens. An algorithm in Matlab could be able to automatically find the right rotation angle, using the neutral axis in the SBS specimen as a reference.
- Reducing the dependency on man-made judgment by applying a least-square solution to fit shear data.
- Applying more data sets to the FEMU iterative model for increased statistical confidence in the solution.
- Applying more test runs with different materials.

The work performed at the AMSL lab shows that the shear stress-strain curve does not need to differ between shear tests. The Iosipescu shear method is known for providing a pure shear area and giving good results. On the other hand, the Short Beam Shear test was conventionally not suited for shear parameter identification. Using the DIC methods for measuring strain and removing the stress assumptions by applying a FEM model, the two test methods are in agreement with each other. Why are other shear tests giving different shear stress-strain response curves? It would be very informative to remove the assumptions made in other test standards, using a Finite Element Analysis. Does the shear test actually have an area of pure shear and if so, are the calculated stresses correct? Currently, the AMSL at UTA is researching torsion plates. The test is not a popular method to test shear properties. The closed-form stress solution overestimates the shear stresses. In this case, material parameter iterations would be a good way to start to improve on the shear stress-strain solution. With this in mind, the ASTM standards might need to be reviewed for accuracy of the stress assumption.

If the industry is able to characterize the shear non-linear response with cheaper test specimens, it should make these characteristics part of the composite material identification program. The effects of non-linear shear is proven to affect failure load predictions in composite materials considerably, as the local stiffness changes through the specimen thickness. Going one step further, a structure that is loaded out-of-plane will benefit from characterizing the coupling between shear and transverse strains, as these cause the dominant failure modes in shells under this loading case. Thereby, failure load predictions can be improved considerably [11]. Extra accuracy and confidence in the material testing will allow for higher confidence in virtual testing of structures at a higher level. If virtual tests can be used to replace real-life mechanical tests, development costs for a new design will go down (S. Grohman, personal communication, February 12, 2011).

BIBLIOGRAPHY

[1] A. Makeev, Y. He, P. Carpentier, and B. Shonkwiler, *A method for measurement of multiple constitutive properties for composite materials,* Composites Part A: Applied Science and Manufacturing **43**, 2199 (2012).

[2] Department of Defense, *Composite Materials Handbook MIL-HDBK-17-1F,* (2002).

[3] J. Tomblin and W. Seneviratne, *Laminate Statistical Allowable Generation for Fiber-Reinforced Composite Materials : Lamina Variability Method*, Tech. Rep. January (DOT/FAA/AR-06/53, 2009).

[4] Y. He, A. Makeev, and B. Shonkwiler, *Characterization of nonlinear shear properties for composite materials using digital image correlation and finite element analysis,* Composites Science and Technology **73**, 64 (2012).

[5] A. P. Carpentier, *Advanced Materials Characterization based on Full Field Deformation Measurements*, Ph.D. thesis, University of Texas at Arlington (2013).

[6] Y. He, *Matrix-Dominated Constitutive Laws for Composite Materials*, Ph.D. thesis, Georgia Institute of Technology (2010).

[7] M. Grédiac, F. Auslender, and F. Pierron, *Applying the virtual fields method to determine the through-thickness moduli of thick composites with a nonlinear shear response,* Composites Part A: Applied Science and Manufacturing **32**, 1713 (2001).

[8] H. T. Hahn and S. W. Tsai, *Nonlinear Elastic Behavior of Unidirectional Composite Laminae,* Journal of Composite Materials **7**, 102 (1973).

[9] W. Sun and A. Lau, *Three-Dimensional Constitutive Model for Anisotropic Inelastic Deformation of Unidirectional Reinforced Composites,* Journal of Thermoplastic Composite Materials **15**, 477 (2002).

[10] A. Puck and H. Schürmann, *Failure Analysis of FRP Laminates by means of Physically based Phenomenological Models,* Composites Science and Technology **58**, 1045 (1998).

[11] P. P. Camanho, C. G. Dávila, S. T. Pinho, L. Iannucci, and P. Robinson, *Prediction of in situ strengths and matrix cracking in composites under transverse tension and in-plane shear,* Composites Part A: Applied Science and Manufacturing **37**, 165 (2006).

[12] T. Vogler and S. Kyriakides, *Inelastic behavior of an AS4/PEEK composite under combined transverse compression and shear. Part I: experiments,* International Journal of Plasticity **15**, 783 (1999).

[13] T. Vogler, S.-Y. Hsu, and S. Kyriakides, *Composite failure under combined compression and shear,* International Journal of Solids and Structures **37**, 1765 (2000).

[14] D. Adams, L. Carlsson, and R. Pipes, *Experimental characterization of advanced composite materials* (CRC Press LLC, 2003).

[15] H. Czichos, T. Saito, and L. Smith, eds., *Springer Handbook of Materials Measurement Methods* (Springer Science+Business Media, Inc., 2006).

[16] W. Sharpe, ed., *Springer Handbook of Experimental Solid Mechanics* (Springer Science+Business Media, Inc., New York, NY, 2008).

[17] M. Sutton, J. Orteu, and H. Schreier, eds., *Image Correlation for Shape, Motion and Deformation Measurements* (Springer Science+Business Media, LLC, New York, NY, 2009).

[18] K. D. Potter, *Understanding the Origins of Defects and Variability in Composites Manufacture,* in *17th International Conference on Composite Materials* (Edinburgh, UK, 2009).

[19] Hexcel Composites, *HexPly ® 8552 Product Data*, Tech. Rep. (Hexcel, 2013).

[20] K. Marlett, *Hexcel 8552 IM7 Unidirectional Qualification Material Property Data Report*, Tech. Rep. (National Institute for Aviation Research, Wichita, 2011).

[21] ASTM Standard D2344-00, *"Standard Test Method for Short-Beam Strength of Polymer Matrix Composite Materials"*, Reapproved 2006 (ASTM International, West Conshohocken, PA, 2006, 2006).

[22] Y. He and A. Makeev, *Implementation of Nonlinear Shear Models for Composite Materials in ABAQUS*, Tech. Rep. (Georgia Institute of Technology, Atlanta, GA, 2008).

[23] M. Grédiac, *The use of full-field measurement methods in composite material characterization: interest and limitations,* Composites Part A: Applied Science and Manufacturing **35**, 751 (2004).

[24] J. Molimard, *Identification of the Four Orthotropic Plate Stiffnesses Using a Single Open-hole Tensile Test,* Experimental Mechanics **45**, 404 (2005).

[25] D. Lecompte, A. Smits, H. Sol, J. Vantomme, and D. Van Hemelrijck, *Mixed numerical–experimental technique for orthotropic parameter identification using biaxial tensile tests on cruciform specimens,* International Journal of Solids and Structures **44**, 1643 (2007).

[26] S. Avril, M. Bonnet, A.-S. Bretelle, M. Grédiac, F. Hild, P. Ienny, F. Latourte, D. Lemosse, S. Pagano, E. Pagnacco, and F. Pierron, *Overview of Identification Methods of Mechanical Parameters Based on Full-field Measurements,* Experimental Mechanics **48**, 381 (2008).

[27] M. Grédiac and F. Pierron, *Applying the Virtual Fields Method to the identification of elasto-plastic constitutive parameters,* International Journal of Plasticity **22**, 602 (2006).

[28] M. Grédiac, E. Toussaint, and F. Pierron, *Special virtual fields for the direct determination of material parameters with the virtual fields method . 1 — Principle and definition,* Composites Part A: Applied Science and Manufacturing **32**, 2691 (2002).

[29] a. Chan, W. Chiu, and X. Liu, *Determining the elastic interlaminar shear modulus of composite laminates,* Composite Structures **80**, 396 (2007).

[30] J. Cugnoni, T. Gmür, and A. Schorderet, *Inverse method based on modal analysis for characterizing the constitutive properties of thick composite plates,* Computers & Structures **85**, 1310 (2007).

[31] E. Florentin and G. Lubineau, *Identification of the parameters of an elastic material model using the constitutive equation gap method,* Computational Mechanics **46**, 521 (2010).

[32] R. Haj-Ali and H.-K. Kim, *Nonlinear constitutive models for FRP composites using artificial neural networks,* Mechanics of Materials **39**, 1035 (2007).

[33] A. Makeev, Y. Nikishkov, R. Cross, and E. Armanios, *Empirical Modeling Based on Neural Networks and Bayesian Learning,* in *45th AIAA/ASME/ASCE/AHS/ASC Structures, Structural Dynamics & Materials Conference*, April (American Institute of Aeronautics and Astronautics, Palm Springs, 2004) pp. 1–13.

[34] M. R. Gurvich and P. L. Clavette, *Probabilistic Characterization of Elastic Properties of Composites Using Digital Image Correlation Technique,* in *Composite Materials and Joining Technologies for Composites, Volume 7*, Conference Proceedings of the Society for Experimental Mechanics Series, Vol. 7, edited by E. Patterson, D. Backman, and G. Cloud (Springer New York, New York, NY, 2012) Chap. 10, pp. 93–98.

[35] B. P. Smarslok, R. T. Haftka, and P. G. Ifju, *Correlation model for composite elastic properties using only measurements from a single specimen,* Probabilistic Engineering Mechanics **29**, 64 (2012).

[36] M. Kashfuddoja and M. Ramji, *Whole-field strain analysis and damage assessment of adhesively bonded patch repair of CFRP laminates using 3D-DIC and FEA,* Composites Part B: Engineering **53**, 46 (2013).

[37] J.-H. Kim, F. Pierron, M. Wisnom, and S. Avril, *Local stiffness reduction in impacted composite plates from full-field measurements,* Composites Part A: Applied Science and Manufacturing **40**, 1961 (2009).

[38] P. Sztefek and R. Olsson, *Tensile stiffness distribution in impacted composite laminates determined by an inverse method,* Composites Part A: Applied Science and Manufacturing **39**, 1282 (2008).

[39] J.-H. Kim, F. Pierron, M. Wisnom, and K. Syed-Muhamad, *Identification of the local stiffness reduction of a damaged composite plate using the virtual fields method,* Composites Part A: Applied Science and Manufacturing **38**, 2065 (2007).

[40] E. Florentin and G. Lubineau, *Identifiying Product Behaviour using Constitutive Equation Gap Method,* in *IDMME - Virtual Concept 2010* (Bordeaux, France, 2010).

[41] A. Moussawi, G. Lubineau, E. Florentin, and B. Blaysat, *The constitutive compatibility method for identification of material parameters based on full-field measurements,* Computer Methods in Applied Mechanics and Engineering **265**, 1 (2013).

[42] P. Pineau and F. Dau, *Subsampling and homogenization to investigate variability of composite material mechanical properties,* Computer Methods in Applied Mechanics and Engineering **241-244**, 238 (2012).

[43] T. Skourlis, K. Pochiraju, C. Chassapis, and S. Manoochehri, *Structure-modulus relationships for injection-molded long fiber-reinforced polyphthalamides,* Composites Part B: Engineering **29B**, 309 (1998).

[44] S. Sriramula and M. K. Chryssanthopoulos, *An experimental characterisation of spatial variability in GFRP composite panels,* Structural Safety **42**, 1 (2013).

[45] W. C. Young and R. G. Budynas, *Roark ' s Formulas for Stress and Strain*, 7th ed., edited by Larry Hager (R. R. Donnelley & Sons Company, 2002).

[46] Dassault Systems, *Abaqus 6.12 Documentation Collection,* (2012).

[47] Y. Wen-juan and Y. Zhi-ming, *Analytical solution of bending-compression column using different tension-compression modulus,* Applied Mathematics and Mechanics **25**, 983 (2004).

A

INTERFACE FOR THE FEMU MODEL

This appendix gives an overview of the interface of the FEMU program, of which the workings have been explained in chapter 3. This appendix shows the organization of the (sub)directories, the layout of the input and output files, the Readme.txt and an example script to run a batch of specimens.

The actual scripts used for the program are too extensive to include in this appendix. These would span many pages. Instead, the program is added to the attached CD (see appendix F).

A.1. FEMU PROGRAM WORK DIRECTORY OVERVIEW

Figure A.1 shows the organization of the work directory and its subdirectories. The functions of each file specified in this figure is explained in the ReadMe.txt (sec. A.4). Apart from having all these files and folders in place, the program places certain requirements on Abaqus:

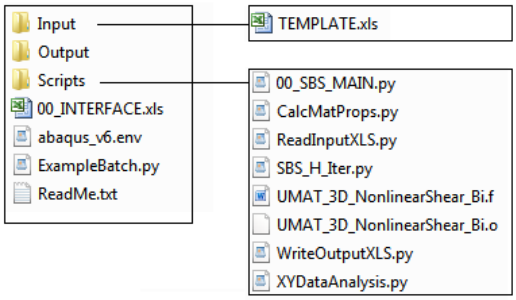


Figure A.1: Overview of File Organization of FEMU Program

- The FEMU program has been developed in ABAQUS/CAE V6.11, but the model has been parametrized to prevent being version dependent.
- The UMAT is written in Fortran. If the user cannot compile Fortran, he can use the .o compiled object instead. This way, the adapted file "abaqus_v6.env" is not necessary.
- Abaqus should have Python packages xlread, xlwrite and xlutils installed.

A.2. INPUT FILE TEMPLATE

The input file is one excel spreadsheet with 4 sheets. This layout of the first sheet is given in table A.1. Here, the user specifies the model parameters. Sheets 2, 3 and 4 are used to input strain and loading data from the test. The layout of these sheets is shown in tables A.2a and A.2b.

A.3. OUTPUT FILE EXAMPLE

The output of the FEMU program is given in one excel spreadsheet. Every sheet represents one iteration. An example sheet is shown in table A.3.

A.4. FEMU PROGRAM README

```
################################################################################
                              #REQUIREMENTS
################################################################################
* US Units (inch)
* Requires the following files to run:
  1. UMAT user subroutine for material behavior. Assumptions:
     Non-linear shear (Ramberg-Osgood equation), bimodular in 11 and 22,
     transverse isotropic
  2. py scripts:
     1) 00_SBS_MAIN.py
Main script
     2) SBS_H_Iter.py
Short Beam Shear Half Model for Iterations
     3) ReadInputXLS.py
This file reads the input excel file.
     4) CalcMatProps.py
This file calculates: G, GK, Gn, ExxT, ExxC and the Stress-Strain Curve;
     5) XYDataAnalysis.py
This file calculates:  Sxy, dSxx/dy, Neutral Axis FEM, dLEyy/dy;
This file updates:  Neutral Axis, NUxy;
     6) WriteOutputXLS.py
This file writes the output excel file
  3. DIC strain data: Columns for different variables, no empty/string cells
     1) Across frames: Force[lb], Engineering Shear Strain
     2) At x=L/4, specified frame: exx, eyy, Yc (corrected y-coordinates)
  4. Abaqus .env file to be set to handle the UMAT in Fortran
* Abaqus will read one input file as XLS in subdirectory /Input
* Abaqus will place one output file as XLS in subdirectory /Output/Specimen_name

################################################################################
                              #USER INSTRUCTIONS
################################################################################

The following 4 steps are needed to run an analysis:

STEP 1a:  Create the input excel file according to the template. Place it in
            subdirectory /input. Type in Abaqus/CAE:  File= 'Input/FILENAME'
  OR 1b:  Fill in 00_INTERFACE.xls in the work directory.
  OR 1c:  Write custom batch file. See ExampleBatch.py
STEP 2:   Start ABAQUS/CAE and set Work Directory
```

Table A.1: FEMU Input Template, Sheet 1

SHORT BEAM SHEAR SPECIMEN MATERIAL ITERATIONS. ALL UNITS ARE EMPIRICAL		
NAMES	VALUES, READ BY ABAQUS	COMMENTS, FREE TO ALTERATION
MATERIAL NAME	⋯	Only letters and numbers
SPECIMEN NAME	⋯	Only letters and numbers
LOADING		
LOADPLANE	⋯	12, 13 or 23. 13 by default
FRAME	⋯	Which Frame with cross-sectional data?
SHEAR LIN. RANGE L	⋯	FIRST FRAME
SHEAR LIN. RANGE L	⋯	LAST FRAME
SHEAR NONLIN. RANGE L	⋯	FIRST FRAME; Linear shear: set to 0
SHEAR NONLIN. RANGE L	⋯	LAST FRAME; Linear shear: set to 0
TRANSVERSE LIN. RANGE L	⋯	FIRST POINT
TRANSVERSE LIN. RANGE L	⋯	LAST POINT
SHEAR LIN. RANGE R	⋯	FIRST FRAME
SHEAR LIN. RANGE R	⋯	LAST FRAME
SHEAR NONLIN. RANGE R	⋯	FIRST FRAME; Linear shear: set to 0
SHEAR NONLIN. RANGE R	⋯	LAST FRAME; Linear shear: set to 0
TRANSVERSE LIN. RANGE R	⋯	FIRST POINT
TRANSVERSE LIN. RANGE R	⋯	LAST POINT
GEOMETRY [in]		
WIDTH	⋯	Width dimension
THICKNESS	⋯	Thickness dimension
NOSE DIAMETER	⋯	
SUPPORT DIAMETER	⋯	
X-LOCATION RIGHT SUPPORT	⋯	Reference is loading nose
X-LOCATION LEFT SUPPORT	⋯	Reference is loading nose
MODEL PARAMETERS		
ACCURACY	⋯	Convergence Criterion
MAX NR. OF ITERATIONS	⋯	Maximum number of iterations
NR. OF CPU'S	⋯	Number of CPU's to run the job
STARTING POINT MATERIAL ITERATIONS[psi]		
E11T	⋯	Tensile Stiffness in 11
E11C	⋯	Compressive Stiffness in 11
E22T	⋯	Tensile Stiffness in 22
E22C	⋯	Compressive Stiffness in 22
E33	⋯	Stiffness in 33
NU12	⋯	Poisson's Ratio 12
NU13	⋯	Poisson's Ratio 13
NU23	⋯	Poisson's Ratio 23
G12	⋯	Shear Stiffness in 12
G13	⋯	Shear Stiffness in 13
G23	⋯	Shear Stiffness in 23
GK	⋯	Ramberg-Osgood S-I modulus
Gn	⋯	Ramberg-Osgood exponent

Table A.2: FEMU Input Template, Sheets 2-4

(a) FEMU Input Template, Sheet 2

Force (lbs)	**γxy (left)**	**γxy (right)**
⋮	⋮	⋮

(b) FEMU Input Template, Sheet 2 (Left XSection) and 3 (Right XSection)

exx	**eyy**	**Yc (in)**
⋮	⋮	⋮

Table A.3: FEMU Output Sheet for IM7/8552 Specimen, Iteration 1

PREV: E11T	E11C	E22T	E22C	E33	NU12	NU13	NU23
	G12	G13	G23	GK	Gn		
23700000	21700000	1700000	1700000	1300000	0.32	0.32	0.5
	737000	743000	435000	36100	0.201		
NEW: E11T	E11C	E22T	E22C	E33	NU12	NU13	NU23
	G12	G13	G23	GK	Gn		
26411423	20903715	1700000	1700000	1300000	0.32	0.308804	0.5
	737000	784945	435000	32209.7	0.219707		
Surface:	ExxT	ExxC	NUxy	Gxy	GK	Gn	Neutral Axis
L	28375097	22457895	0.59631	830935.2	34536.8	0.226761	0.038981
R	24447749	19349536	0.182601	738954.8	29882.59	0.212653	0.038981
Frame	Load	Sxy left	DIC gxy left	R-O left	Sxy right	DIC gxy right	R-O right
1	0.001	0.026329	0	4.68E-08	0.024021	0	5.26E-08
2	0.1072	2.990844	2.86E-05	5.02E-06	2.766134	1.33E-05	5.64E-06
3	0.2515	7.170229	6.53E-05	1.18E-05	6.672869	7.92E-05	1.32E-05
4	5.3554	174.9193	0.00038	0.000251	174.9193	0.000308	0.000282
5	16.6273	572.8478	0.0009	0.000778	572.8478	0.000963	0.000875
6	31.0194	1094.967	0.001662	0.001452	1094.967	0.001641	0.001632
7	47.3592	1693.096	0.002381	0.002218	1693.096	0.002485	0.002493
⋮	⋮	⋮	⋮	⋮	⋮	⋮	
30	379.9809	12550.45	0.028819	0.027581	12550.45	0.037175	0.035313
31	382.6682	12626.71	0.030352	0.028009	12626.71	0.039572	0.035943
Fr.21 L: Y	Sxx	Syy	Sxy	LExx	LEyy	LExy	
-0.07875	63910.33	0.506325	838.8712	0.00242	-0.00075	0.00107	
-0.07481	59477.11	5.114651	1612.218	0.002252	-0.00069	0.002059	
-0.07087	54627.55	28.31098	3311.488	0.002067	-0.00062	0.004272	
⋮	⋮	⋮	⋮	⋮	⋮	⋮	
0.070875	-46606.8	-326.146	2708.379	-0.00223	0.000442	0.003471	
0.074813	-48955.4	-351.497	1334.026	-0.00234	0.000457	0.0017	
0.07875	-51908.9	-356.653	728.7225	-0.00248	0.000498	0.000927	
Fr.21 R: Y	Sxx	Syy	Sxy	LExx	LEyy	LExy	
-0.07875	63910.34	0.506334	-838.871	0.00242	-0.00075	-0.00107	
-0.07481	59477.11	5.11465	-1612.22	0.002252	-0.00069	-0.00206	
-0.07087	54627.55	28.31098	-3311.49	0.002067	-0.00062	-0.00427	
⋮	⋮	⋮	⋮	⋮	⋮	⋮	
0.070875	-46606.8	-326.146	-2708.38	-0.00223	0.000442	-0.00347	
0.074813	-48955.4	-351.497	-1334.03	-0.00234	0.000457	-0.0017	
0.07875	-51908.9	-356.653	-728.723	-0.00248	0.000498	-0.00093	

```
STEP 3:   Run script: 00_SBS_MAIN.py
  TO RUN:  execfile('Scripts/00_SBS_MAIN.py', __main__.__dict__)
STEP 4:   Find output files in Output/Specimen_name

In order to automize a batch run, one is encouraged to modify ExampleBatch.py. It is
intended to run an iterative loop for each input file. A consistent naming convention
would enable this method.

################################################################################
                              #NOTES ON THE INPUT FILE
################################################################################

The input file will contain the strain data for both the left and right data set.
Certain parameters are specimen-specific (width and thickness, etc), but other
parameters have to be specified separately, as is specified in the template

Sheet 'Model'

* The material name influences the Job-name.
* The specimen name determines the output directory.
* The user is expected to examine the DIC data to define in which regions
     the data is linear. For linear shear response, set Rnl to [0,0]
* The material starting point has a lot of freedom. Reasonable values affect
     material properties <1%

Sheet 'Shear Input'

* Across frames, specify the load [lbs] and engineering shear strain,
    both left and right

Sheets 'XSection Left' and 'XSection Right'

* Choose a frame which has high load, but is well below failure
* Specify at L/4: epsilon_xx, epsilon_yy and the corresponding corrected
    Y-coordinates in [inch]

################################################################################
                              #OUTPUT FILE
################################################################################

The output file is an excel spreadsheet and contains one sheet per iteration.
It shows the following things:

* Material properties previous iteration
* Material properties end of this iteration
* Material properties calculated from the 2 data sets (left and right)
* Across frames: Load, left and right shear stress-strain data
  *  Shear Stress
  *  DIC Engineering Strain
  *  R-O Simulation in FEM
* For the specified frame in the input file, at L/4 (first left then right):
  *  Y-coordinates
  *  Stress components: Sxx, Syy, Sxy
  *  Strain components: LExx, LEyy, LExy

################################################################################
```

```
                                #FINAL NOTES
###############################################################################
* Mesh for SBSQuarter is converged for material properties, not for the
    stress concentrations
* Monitor job progress: CAUTION: Apply only once per Abaqus session!
    Type in the following commands in Abaqus:
    monitorManager.addMessageCallback(ANY_JOB,ANY_MESSAGE_TYPE, printMessages, None)
* As the material data set left is deemed equally important as the data set right,
    the actual model parameters are the resultant of average material properties.
    Most importantly, it was impossible to converge the neutral axis separately
    left and right.
```

A.5. FEMU PROGRAM EXAMPLE BATCH SCRIPT

The script below is used to run the batch of IM7/8552 specimens as shown in 3.6. It runs multiple specimens with one command. It constructs the name of the input file and then runs the iterative method.

```
Mat  = 'Input/I8-A'# For naming convention

for i in [1,4,5,6]:
      # Generate filename
      File = Mat + str(i) + '.xls'
      print File
#
      # Run iterative loop
      execfile('Scripts/00_SBS_MAIN.py', __main__.__dict__)
```

B

Influence of Noise in DIC Measurements

The measurements in DIC are inherently noisy. This noise has various causes and influences which material properties are calculated. For accurate material characterization, it is necessary to understand the noise mechanisms. The finite resolution of the camera and optical quality of the lens combined with the speckle size, quality, and distribution form a physical limit on what the accuracy of the DIC method can be. The speckle size is limited on the resolution of the camera, which has to be able to distinguish between the speckles. Next, the algorithms that the VIC3D software uses to track the speckles and create the strain fields have limited accuracy and are less reliable near the edges of the speckle field. Lastly, the user of the software has a lot of influence on the noise levels by changing the filter or subset size. The filter and subset sizes affect the smoothing of the data.

The noise in an image is thus inherent to a lot of factors and any absolute values in this section are used to find trends. Most importantly, the method may be used for defining the noise in the spatial variability of stiffness plots. It is assumed that noise in the DIC method is the sole contributor to this noise. To find these trends, two simpler mechanical tests are analyzed: tensile and compressive tests. Figure B.1 shows a compression specimen with a speckle pattern used for the DIC analysis.

As the specimen is loaded, the speckle pattern is deformed. Images of these deformed patterns are processed with the VIC3D software, using sizes for the filter and subset as recommended by the software. Figures B.2 - B.4 show the strain fields in yy (transverse), xx (axial) and xy (shear) strains. The transverse strains are highest and compressive. The axial strains are lower and positive and the shear strains are nearly zero. To create the probability (PDF) and cumulative (CDF) density function plots, all the data points (coordinates and strain values) are read into Matlab. The edges of the fields are cut off, because it often consists of bad data. Then the probability and cumulative density plots are generated.

There are two relevant probability methods available that work well to create the statistical plots in figure B.2 - B.4. The normal distribution is a common method and calculates the mean and standard deviation of the distribution. The Student's t-distribution offers a better fit at select cases, but is generally more applicable for data sets with few measurement points. A strain fields consists of hundreds of data points, so the normal distribution is more applicable. Due to edge effects, the influence of outliers can be significant, which have to be cut off from the analysis. The outliers are cut off until the CDF of the normal fit matches that of the measurement data.

The method as described above is applied to two tensile specimens (T1 and T2) and two compression specimens (C1 and C2) for two different load levels. The results are shown in tables B.1 and B.2. For each strain field, the mean (μ) and standard deviation (σ [%]) are given. One can already quickly see that the higher the strain level, the lower the percentage of the standard deviation is. This is because the signal to noise ratio

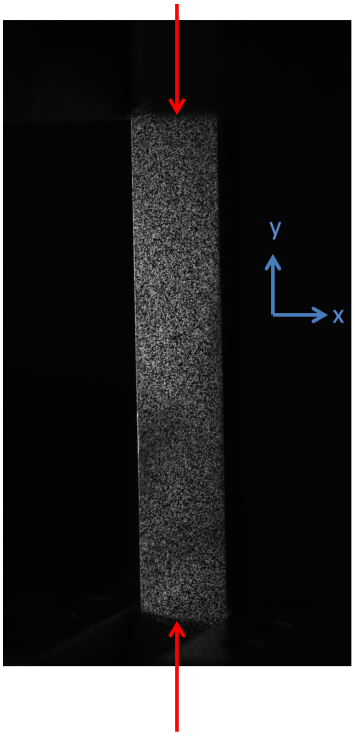


Figure B.1: Compression Test Specimen, showing the Speckle Pattern

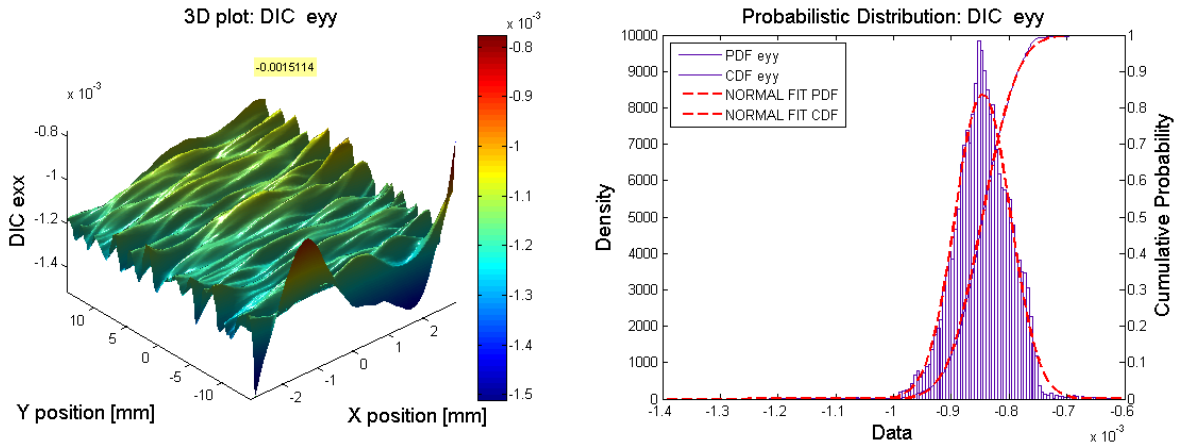
improves at higher strain levels. Even though the noise contribution may be very small in one direction, it might be very significant in other directions. In this example, the measurements for the shear strains are very unreliable, as the standard deviation is over 100% for most specimens. As mentioned before, these noise values may be decreased by increasing the filter size, smoothening the data.

For an SBS specimen, it is not advisable to keep increasing the filter size. The strain gradients would not be represented properly if the data is filtered too much. For similar subset and filter sizes, the noise is very significant at strain levels below 1000 microstrain. That is the reason why transverse strain measurements in the SBS specimens are noisy compared to axial strains. The absolute values of these strains are very small, but they are also subject to strain gradients. The standard deviation of the noise is generally a lot higher than the covariance of the calculated material properties [1]. A good analysis does not use point calculations, but rather the average value of an area.

Table B.1: Mean Values and St. Deviation for Tensile Specimens T1 and T2 for IM7/8552. Format: μ (σ [%])

	T1		T2	
Load	579	912	1312	2293
ϵ_{yy}	4.6E-4 (4.2)	7.0E-4 (3.5)	1.1E-3 (5.9)	1.8E-3 (4.3)
ϵ_{xx}	-1.3E-4 (24)	-2.3E-4 (10)	-3.3E-4 (11)	-5.8E-4 (7.6)
ϵ_{xy}	-1.7E-5 (129)	-2.3E-5 (108)	-4.0E-5 (103)	-1.0E-4 (77)
ν_{12}	0.27	0.33	0.31	0.33

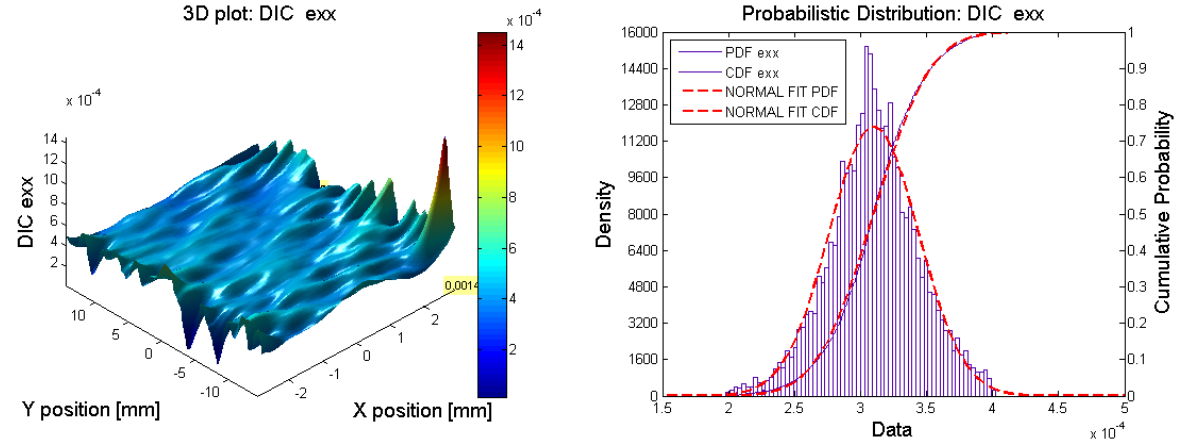
This method of visualization can be used to identify and cut off pinching phenomena, and find the mean of a data set to determine material parameters more accurately. As an example, the Poisson's ratio is identified for the tensile and compressive specimens, using the mean value of the strain data sets. They are noted in tables B.1 and B.2. The spread of this ratio is not very high in the selected data sets. However, there seems to be a clear distinction between the Poisson's ratio for specimens loaded in tension and those loaded in compression. Those loaded in tension have an average Poisson's ratio of 0.31 against a ratio of 0.37 in compression. This is close to the values as specified by Hexcel [20]. It confirms that the Poisson's ratio is stress-state dependent, as is explained in more detail in section 5.2.



(a) Transverse Strains on the Surface

(b) Statistical Probability and Cumulative Distribution

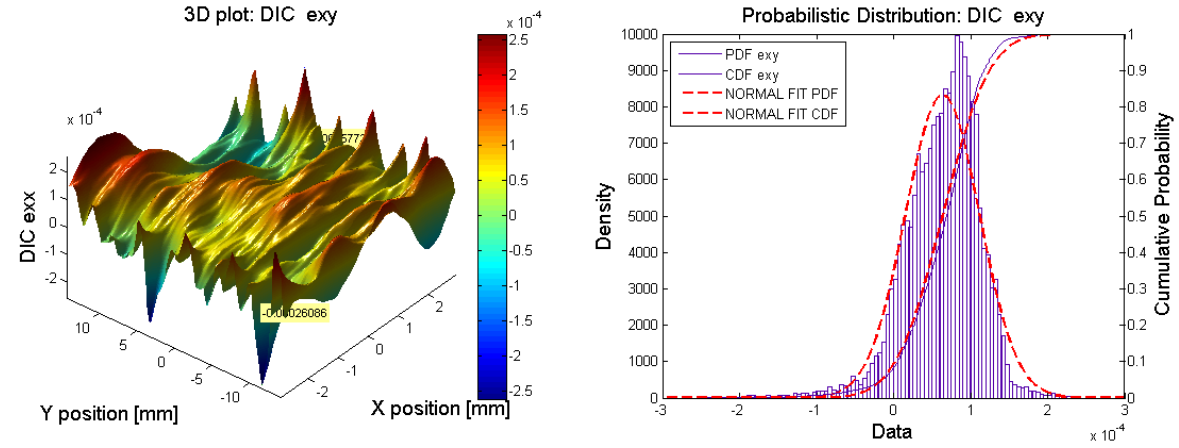
Figure B.2: Transverse Strains in IM7/8552 Compression Specimen and its Statistical Distribution



(a) Axial Strains on the Surface

(b) Statistical Probability and Cumulative Distribution

Figure B.3: Axial Strains in IM7/8552 Compression Specimen and its Statistical Distribution



(a) Shear Strains on the Surface

(b) Statistical Probability and Cumulative Distribution

Figure B.4: Shear Strains in IM7/8552 Compression Specimen and its Statistical Distribution

Table B.2: Mean Values and St. Deviation for Compression Specimens C1 and C2 for IM7/8552. Format: μ (σ [%])

	C1		C2	
Load	709	1160	1315	1584
ϵ_{yy}	-5.0E-4 (8.4)	-8.5E-4 (5.6)	-9.7E-4 (4.1)	-1.2E-4 (3.9)
ϵ_{xx}	1.9E-4 (16)	3.1E-4 (11)	3.6E-4 (12)	4.3E-4 (8.8)
ϵ_{xy}	5.0E-5 (87)	6.0E-5 (75)	4.3E-5 (107)	6.1E-5 (87)
ν_{12}	0.39	0.37	0.37	0.37

C

APPARENT STIFFNESS PLOTS WITH HOMOGENEOUS MODEL

This appendix shows how to generate apparent stiffness plots in SBS specimens, using a pre-defined homogeneous model. These plots will show how apparent axial and shear stiffness change over a surface. Apparent stiffness is the local tangent of the stress-strain curve or the derivative of the stress-strain equation, depending on the level of stress and the material model. It represents the local stiffness, as defined by the material model. This stiffness is stress-dependent; The axial stiffness in tension is different than in compression. Also, the apparent local shear stiffness is reduced under high shear stresses, due to the non-linear stress-strain equation.

C.1. LOCAL STIFFNESS CHANGES IN FEM

The FEM model can be used to generate apparent stiffness plots across the front surface. Its application might be structural: The engineer would want to know the stiffness of it's structure through the thickness of its plates, in order to accurately determine the failure loads. The UMAT is responsible for modeling the material behavior and is described in section 3.3. This UMAT determines the derivative of the stress-strain curve (the Jacobian) for every integration point. Equation (E.5) give the local apparent stiffness in shear. One may specify a certain frame and a certain group of integration points for which to write stiffness parameters to a separate file. The extract below shows how to export the necessary data. The if statement selects a group of nodes (based on coordinates) and increment number. It then opens a new file called 'Exp99.rpl', in which it adds the following data for each integration point: element number, integration point number, x-coordinate, y-coordinate, apparent shear and axial stiffness, axial and shear strains and stresses in the 13-plane.

```
 IF ((COORDS(3).GT.0.1 .AND. COORDS(1).LT.0.56.AND.
1          COORDS(1).GT.-0.56) .AND. (KINC.EQ.99 )) THEN
   open (unit = 10001, file ='Exp99.rpl',position='append')
   write(10001,*) NOEL, NPT, COORDS(1), COORDS(2), DDSDDE(5,5),
1          E11, STRAN(1), STRAN(5), STRESS(1), STRESS(5)
   close(10001)
 END IF
```

For the method above, this example writes the requested data for all integration points at a specified surface. This method is duplicated for frame 0, where the integration point coordinates are undeformed. Unfortunately, these data file shows many more data points than necessary: a lot of these points are duplicates. Also, the number of nodes selected at zero load level is different from that selected at high load level. For easy reading in Matlab, it was chosen to convert this text file to a .CSV file. A Python script was set up that performs this

conversion. First, it reads the raw data files. Next, it creates a library for each data point (the x- and y-values are the keys). These libraries prevent duplicate data points. Then, it takes the undeformed point coordinates from frame 0 and the loaded apparent stiffness and strain values from the specified frame. It sorts the libraries on x-value and deletes the entries that do not have the desired data. this final selection is written to a new .CSV file. Please refer to "FilterExport.py" in the attached CD.

In Matlab, the .CSV file with the values from UMAT is finally read. The "linspace" function is used in combination with the "meshgrid" function to create a grid to generate surface plots on. The "scatteredInterpolant" function is used to interpolate the UMAT values onto this grid, and the "surf" function is used to generate the plots. These two plots are generated for a S2/381 glass specimen under high load. The results are shown in figures C.1 and C.2. One can indeed see the expected changes in stiffness: The bottom part of the SBS specimen is loaded in tension ($E_{11} = 7.5E6$) and the top in compression ($E_{11} = 6.8E6$). Furthermore, one can see that the regions where the shear strains are highest, the local shear stiffness is lowest. The right shear stiffness is slightly lower than left, as the supports are not placed symmetrically.

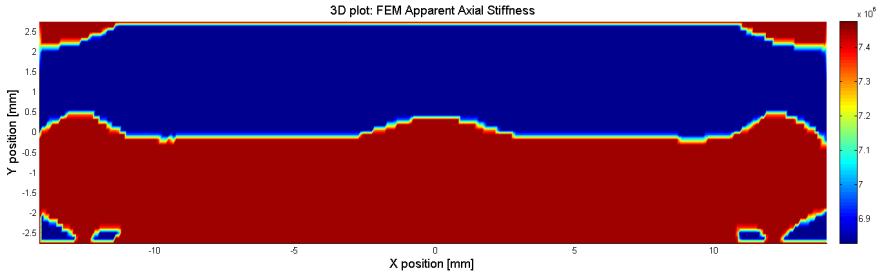


Figure C.1: Apparent Axial Stiffness over the Front Surface of a SBS Specimen in FEM

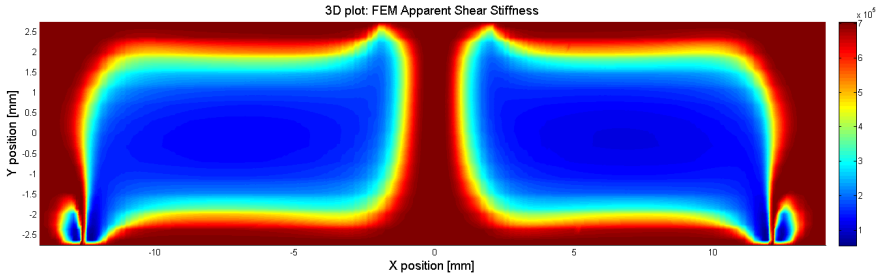


Figure C.2: Apparent Shear Stiffness over the Front Surface of a SBS Specimen in FEM

C.2. LOCAL STIFFNESS CHANGES IN DIC

The method of generating spatial plots of apparent stiffness works for the FEM model, but it can also be applied to the measured strain data from DIC. This may not have a direct structural significance, but does have an application for the processing of the DIC strain data. This is illustrated in figures C.3 to C.6. This strain data is taken from S2/8552 glass epoxy UD specimens under 1200 lbf. As mentioned in section 3.1, the DIC data has to be properly corrected for the coordinate system. Because of the positioning of the camera's and the test piece, the coordinate systems do not necessarily line up and the strain fields look twisted. This twisting is corrected for by a rotation angle. The twisting is easily visualized by the line separating the tensile ($E_{11} = 6.0E6$) and compressive ($E_{11} = 7.4E6$) axial stiffness zones. They are separated by a neutral axis, which should be horizontal. These two specimens are rotated by the same angle, yet for specimen 1, the rotation is not quite right. The neutral axis in specimen 2 is nearly horizontal, so the rotation is good. Also, the location of the lowest shear stiffness (highest shear strains) in specimen 1 left and right is not equally high.

The VIC3D program can export its strain fields as a .CSV document or as a Matlab data file. Both work to get the strain field in Matlab. The strain data is then converted using a pre-determined material model, as explained before. To go from shear strains to stiffness, Equation (2.1) has to be inverted, which is not straightforward. Therefore, a look-up table is used to match strain values to apparent stiffness values, using (E.5).

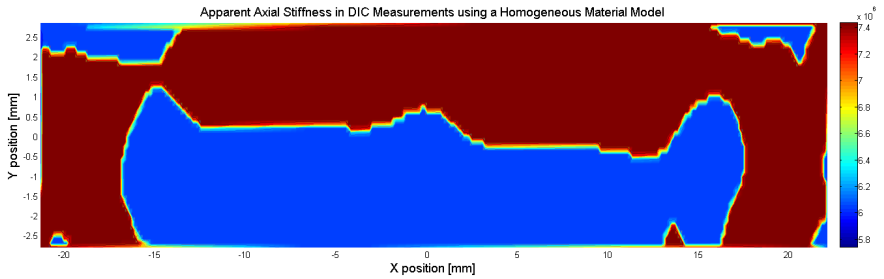


Figure C.3: Apparent Axial Stiffness over the Front Surface of a SBS Specimen in DIC for S2/8552, Specimen 1

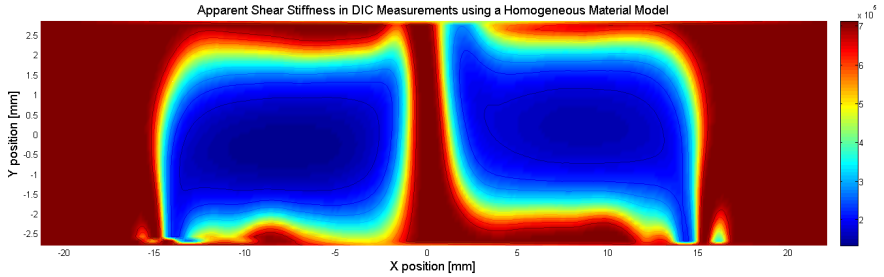


Figure C.4: Apparent Shear Stiffness over the Front Surface of a SBS Specimen in DIC for S2/8552, Specimen 1

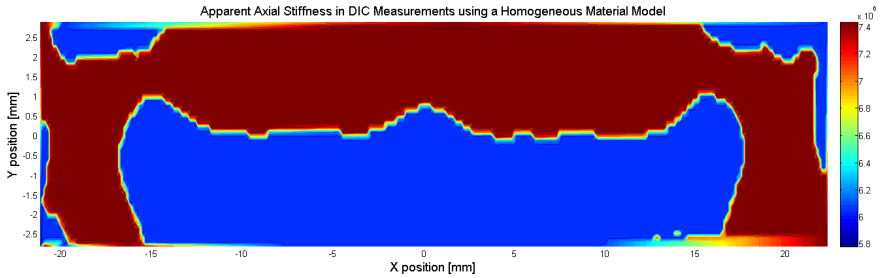


Figure C.5: Apparent Axial Stiffness over the Front Surface of a SBS Specimen in DIC for S2/8552, Specimen 2

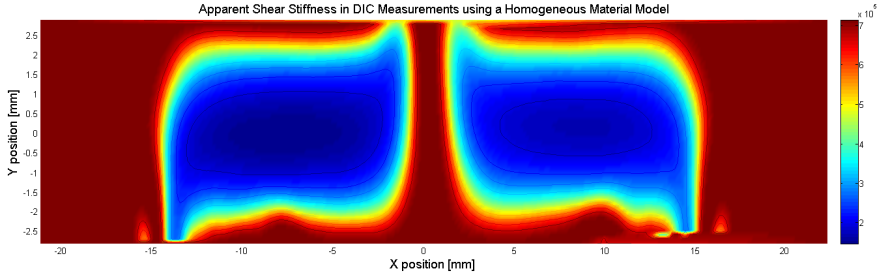


Figure C.6: Apparent Shear Stiffness over the Front Surface of a SBS Specimen in DIC for S2/8552, Specimen 2

The twisting of the strain fields as shown above has a clear influence on the calculated material properties. Most importantly, the neutral axis is different left and right. The neutral axis is used to determine the ratio of the tensile/ compressive axial moduli, which means that the calculated materials properties differ very much from right to left. Furthermore, the shear stiffness calculated on the left is lower, because the peak shear strains at the left side are not at the same location as at the right side.

This method has limited use. So far, it is able to visualize whether the strain fields are properly rotated or not. It also shows that the rotation angle is likely specimen-specific. The analyst can adjust the rotation angle to make the neutral axis horizontal. The material parameters at the start do not influence the conclusions. It should be possible for Matlab to calculate this rotation angle automatically. This, however, is out of the scope of this thesis and is left for continued research.

D

Least-Squares Solution for Ramberg-Osgood Parameters

In this thesis, the Ramberg-Osgood equation is fitted using a linear regression analysis. It is a method that can be applied in Excel. However, the equation is non-linear and the analyst can gain a lot of accuracy by improving on this fitting method. This appendix shows how more advanced curve-fitting in Matlab gives a data fit which improves on the original method by relying far less on user input. Several different concepts are explored to find the most reliable fitting method.

The first method is explained in section 4.2. Linear regression tools in Excel are used to find the parameters G, K and n. These parameters depend on the limits on the selected data ranges. The linear regime is selected to be within 1000 and 6000 microstrain [$\mu\epsilon$]. The non-linear range is chosen depending on the quality of the data at high load levels, as visualized by plotting $ln(\gamma - \frac{\tau}{G})$ vs $ln(\tau)$.

The fit options is used to create the curve-fit in Matlab, using the format in equation (D.1). The nonlinear Least-Squares (LS) method is chosen with reasonable lower and upper limits for the parameters. This method doesn't solve the fit directly. Instead, it starts at a pre-defined starting point and iterates the specified parameters until the best fit is found. It is thus an optimization problem. Unfortunately, the starting point affects the final fit. The Ramberg-Osgood does not provide a single solution that fits the data best. There is a small margin where a higher K value can be compensated by a higher n value. The "Robust" setting is turned on to improve the fit and to stabilize the answer. The dependency on the starting point is further alleviated by restarting the optimization problem with the output parameter coefficients as the starting point.

The third method adapts the nonlinear least-squares fit method by applying a weights vector. This weight vector makes specific data points more important than others. The non-linear fit is too steep at the end; the last data points do not have enough significance and they diverge from the fitline. A weight vector is configured to have a higher weight value for the data points at the end and at the beginning. This produces an even better fit, as the R^2 (a method for accuracy of the curvefit) is increased from 0.9997 to 1.0000. A comparison of the performance of the methods is given in Table D.1 and Figure D.1.

$$\frac{x}{G} + \left(\frac{x}{K}\right)^{\frac{1}{n}} \tag{D.1}$$

The only reason this method is not applied is because of its dependency on the starting point and the format of the weights, which is subject to the user input. The dependency of the starting point is compensated by iterating the fit method, but no consistent method is found to produce reliable results for every data set.

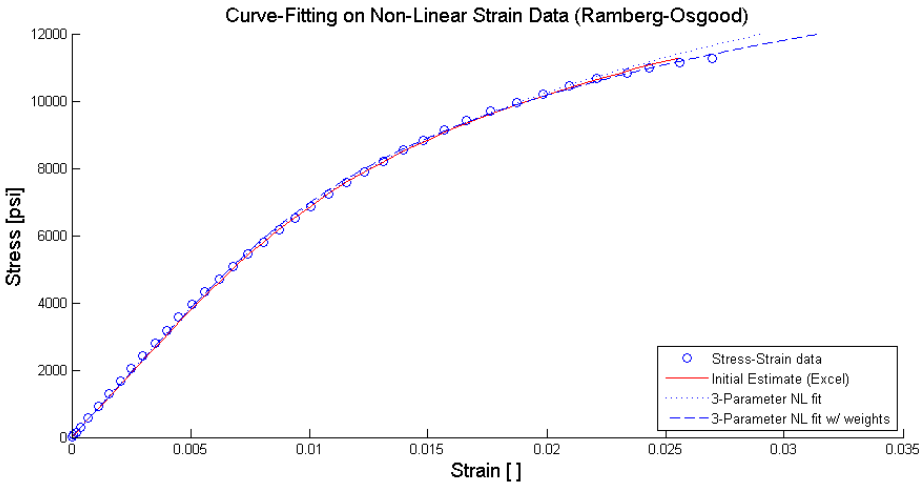


Figure D.1: Curve-Fitting of Shear Stress-Strain Data using a Regression Analysis in Excel and 3-Parameter Nonlinear Curve-Fits with and without weights

Table D.1: Parameters of the Curve Fits for the Ramberg-Osgood Equation

Method	G	K	n	R^2
Excel Method	762,488	29,478	0.212	
Non-lin. LS w/o weights	784,200	31,940	0.229	0.9997
Non-lin. LS w/ weights	772,200	26,870	0.195	1.0000

E

Added Coupling Terms in Shear Non-Linear Regime: Calculations

This appendix covers the steps used to determine which equations are necessary for the User Material subroutine in Abaqus/CAE to define coupling between shear and axial strains. The concept is explained for the 2-dimensional case, which is then expanded to conform the 3-dimensional case.

E.1. 2-Dimensional Coupling

The constitutive model of a material in this case defines the relationship between stresses and strains in a composite material. The conventional 2D constitutive model for uni-directional plies is given in Equation (E.1).

$$\epsilon = [S]\sigma$$
$$\begin{Bmatrix} \epsilon_1 \\ \epsilon_2 \\ \gamma_{12} \end{Bmatrix} = \begin{bmatrix} \frac{1}{E_{11}} & \frac{-\nu_{12}}{E_{11}} & 0 \\ \frac{-\nu_{12}}{E_{11}} & \frac{1}{E_{22}} & 0 \\ 0 & 0 & \frac{1}{G_{12}} \end{bmatrix} \begin{Bmatrix} \sigma_1 \\ \sigma_2 \\ \tau_{12} \end{Bmatrix} \tag{E.1}$$

In Equation (E.1), the 1 stands for the fiber direction of the uni-directional plies and the 2 stands for the transverse direction. The axial stiffness E and shear stiffness G denote the stiffness moduli of the material. ν stands for the Poisson's ratio. ϵ and γ denote the axial and shear strain respectively. σ and τ are used for axial and shear stress respectively. In order to calculate the stiffness matrix, the inverse must be taken from the compliance matrix S, which is shown in Equation (E.2)

$$d = 1 - \nu_{12}^2 \frac{E_{22}}{E_{11}}$$
$$S^{-1} = \begin{bmatrix} \frac{E_{11}}{d} & \frac{\nu_{12}E_{22}}{d} & 0 \\ \frac{\nu_{12}E_{22}}{d} & \frac{E_{22}}{d} & 0 \\ 0 & 0 & G_{12} \end{bmatrix} \tag{E.2}$$

In this case, notice how there is no coupling between the shear and axial strains. If one assumes a coupling term, the compliance matrix will be of the form in Equation (E.3). The inverse of that compliance matrix will thus be given in Equation (E.4)

$$S = \begin{bmatrix} \frac{1}{E_{11}} & \frac{-\nu_{12}}{E_{11}} & \frac{-\nu_{16}}{E_{11}} \\ \frac{-\nu_{12}}{E_{11}} & \frac{1}{E_{22}} & 0 \\ \frac{-\nu_{16}}{E_{11}} & 0 & \frac{1}{G_{12}} \end{bmatrix} \tag{E.3}$$

$$d = 1 - \nu_{12}^2 \frac{E_{22}}{E_{11}} - \nu_{16}^2 \frac{G_{12}}{E_{11}}$$

$$S^{-1} = \begin{bmatrix} \frac{E_{11}}{d} & \frac{\nu_{12}E_{22}}{d} & \frac{\nu_{16}G_{12}}{d} \\ \frac{\nu_{12}E_{22}}{d} & \frac{E_{22}(1-\nu_{16}^2\frac{G_{12}}{E_{11}})}{d} & \frac{\nu_{12}\nu_{16}\frac{E_{22}G_{12}}{E_{11}}}{d} \\ \frac{\nu_{16}G_{12}}{d} & \frac{\nu_{12}\nu_{16}\frac{E_{22}G_{12}}{E_{11}}}{d} & \frac{G_{12}(1-\nu_{12}^2\frac{E_{22}}{E_{11}})}{d} \end{bmatrix} \tag{E.4}$$

E.2. 3-DIMENSIONAL COUPLING

The previous discussion shows clearly how the compliance and stiffness matrix change when a coupling term is added in 2D. The model as used in the research is in 3D, so the above methodology must be expanded for the 3-dimensional case. One starts at the compliance matrix, which is now 6x6 in size. Then one may add coupling terms, as in Equation (E.3). The calculations are performed and checked using Maple. Practically, one should not add more than 1 or 2 coupling terms. Firstly, one cannot measure and validate more than 2 coupling terms at the same time, due to the 2-dimensional nature of the strain measurements. Secondly, whereas the uncoupled constitutive equations are easy to manage, the stiffness matrix grows rapidly in size by adding coupling terms. Anything more than two coupling terms will yield extravagantly long equations for the User Material subroutine, leading to a high chance of human error in incorporating these equations.

By analyzing Short Beam Shear results in the 1-3 plane, it is possible to investigate whether applying a Poisson's ratio ν_{15} (coupling between axial and shear strain) or ν_{35} (transverse and shear strain) may be relevant. Only the effects of a coupling term in the 35 position is considered. Equations (E.8) and (E.9) shows the compliance matrix and Jacobian DDSDDE when adding the term ν_{35}. The convention is the same as in Abaqus, which switches the G12 and G23. As the Jacobian matrix in UMAT represents the derivative of the stress-strain curve ($\frac{\delta\sigma}{\delta\epsilon}$), the shear stiffness G is replaced by the its local non-linear variant, as in equation (E.5). Also, the Poisson's ratio is assumed to be non-linear, with a quadratic form as in equation (E.7). K is the coefficient of this coupling term and is an extra input value to the UMAT. Note that the Jacobian matrix is symmetric. The results have been checked numerically by writing the Jacobian, stresses and strains to a separate file and comparing these to values found in Matlab.

$$G_{12} = \frac{G_{12}}{1 + \frac{G_{12}\cdot|\sigma_{12}|^{\left(\frac{1.0}{Gn}-1.0\right)}}{Gn\cdot Gk^{\frac{1.0}{Gn}}}} \tag{E.5}$$

$$G_{13} = \frac{G_{13}}{1 + \frac{G_{13}\cdot|\sigma_{13}|^{\left(\frac{1.0}{Gn}-1.0\right)}}{Gn\cdot Gk^{\frac{1.0}{Gn}}}} \tag{E.6}$$

$$\nu_{35} = K\cdot\gamma_{13}^2 \tag{E.7}$$

$$S = \begin{bmatrix} \frac{1}{E_{11}} & \frac{-\nu_{12}}{E_{11}} & \frac{-\nu_{13}}{E_{11}} & 0 & 0 & 0 \\ \frac{-\nu_{12}}{E_{11}} & \frac{1}{E_{22}} & \frac{-\nu_{23}}{E_{22}} & 0 & 0 & 0 \\ \frac{-\nu_{13}}{E_{11}} & \frac{-\nu_{23}}{E_{22}} & \frac{1}{E_{33}} & 0 & \frac{-\nu_{35}}{E_{33}} & 0 \\ 0 & 0 & 0 & \frac{1}{G_{12}} & 0 & 0 \\ 0 & 0 & \frac{-\nu_{35}}{E_{33}} & 0 & \frac{1}{G_{13}} & 0 \\ 0 & 0 & 0 & 0 & 0 & \frac{1}{G_{23}} \end{bmatrix} \tag{E.8}$$

$$d = E_{11}E_{22}E_{33} - \nu_{12}^2E_{22}^2E_{33} - \nu_{13}^2E_{22}E_{33}^2 - \nu_{23}^2E_{11}E_{33}^2 - 2.0\nu_{12}\nu_{13}\nu_{23}E_{22}E_{33}^2 - \nu_{35}^2E_{11}E_{22}G_{13} + \nu_{12}^2\nu_{35}^2E_{22}^2G_{13} \quad \text{(E.9)}$$

$$DDSDDE(1,1) = (E_{22}E_{33} - \nu_{23}^2E_{33}^2 - \nu_{35}^2G_{13}E_{22})\frac{E_{11}^2}{d}$$

$$DDSDDE(1,2) = (\nu_{12}E_{22}E_{33} + \nu_{13}\nu_{23}E_{33}^2 - \nu_{12}\nu_{35}^2E_{22}G_{13})\frac{E_{11}E_{22}}{d}$$

$$DDSDDE(1,3) = (\nu_{13} + \nu_{12}\nu_{23})\frac{E_{11}E_{22}E_{33}^2}{d}$$

$$DDSDDE(2,2) = (E_{11}E_{33} - \nu_{13}^2E_{33}^2 - \nu_{35}^2E_{11}G_{13})\frac{E_{22}^2}{d}$$

$$DDSDDE(2,3) = (\nu_{23}E_{11} + \nu_{12}\nu_{13}E_{22})\frac{E_{22}E_{33}^2}{d}$$

$$DDSDDE(3,3) = (E_{11} - \nu_{12}^2E_{22})\frac{E_{22}E_{33}^2}{d}$$

$$DDSDDE(5,1) = (\nu_{13} + \nu_{12}\nu_{23})\frac{\nu_{35}E_{11}E_{22}E_{33}G_{13}}{d}$$

$$DDSDDE(5,2) = (\nu_{12}\nu_{13}E_{22} + \nu_{23}E_{11})\frac{\nu_{35}E_{22}E_{33}G_{13}}{d}$$

$$DDSDDE(5,3) = (E_{11} - \nu_{12}^2E_{22})\frac{\nu_{35}E_{22}E_{33}G_{13}}{d}$$

$$DDSDDE(4,4) = G_{12}$$

$$DDSDDE(5,5) = G_{13} \cdot \frac{(d + \nu_{35}^2E_{11}E_{22}G_{13} - \nu_{12}^2\nu_{35}^2E_{22}^2G_{13})}{d}$$

$$DDSDDE(6,6) = G_{23}$$

F

Introduction to the Included CD

Table F.1: Important Files in the Attached CD

Folder	File	Function
1		See Appendix A
2	Load-Disp.xlsx	Comparing DIC and FEM load-displ. curves
	FEMU Performance.xlsx	Illustrating FEMU performance
	Validation IM7/8552.xlsx	Material characterization IM7/8552
3		
- FEM	ExtractEandG.py	Extract stiffness field values
	griddata_fit.py	Interpolates DIC data on FEM nodes
	plot_DIC.py	Plots DIC nodes in Abaqus
	SBS_Spatial.py	Main file
	SBSHalf.py	Front half model with finer mesh
- Matlab	SpatialVariabilityPlots.m	Main file. Plots stiffness fields with statistics
	Shear Stress-Strain Distr.xlsx	Analysis as in chapter 4.3
4	Coupled nonlin 3D.mw	Coupling equations as in appendix E
5	ExpCoupled.rpl	Numerical check UMAT
	OneElement.py	Single element model for UMAT verification
	UMAT_3D_NLCoupling35.f	UMAT with coupling
6	PostProcessing.m	Main file
	DICPlot.m	Plots DIC strain fields
	FEMPlot.m	Plots FEM stress or strain fields
	UMATPlot.m	Plots UMAT stiffness fields
7	UMAT_3D-NLShear_Bi.f	UMAT that writes output
	FilterExport_V2.py	Reads UMAT output and writes .CSV
8	RambergOsgood_LS.m	Least-squares solution for Ramberg-Osgood
9	DICPlotStiffness.m	Main file.
	DICStiffnessPlots.m	Plots DIC strain fields and stiffness fields
10	DICStatistics.m	Plots DIC strain Fields with Statistics